Self-assembly of nanoparticles on fluid and elastic membranes

Anđela Šarić

Submitted in partial fulfillment of the
requirements for the degree
of Doctor of Philosophy
under the Executive Committee
of the Graduate School of Arts and Sciences

COLUMBIA UNIVERSITY

2013

ABSTRACT

Self-assembly of nanoparticles on fluid and elastic membranes

Anđela Šarić

This dissertation presents studies on self-assembly of nanoparticles adsorbed onto fluid and elastic membranes. It focuses on particles that are at least one order of magnitude larger than the surface thickness, in which case all chemical details of the surface can be ignored in favor of a coarse-grained representation, and the collective behavior of many particles can be analyzed. We use Monte Carlo and molecular dynamics simulations to study the phase behavior of these systems, and its dependence on the mechanical and geometrical properties of the surface, the strength of the particle-surface interaction and the size and the concentration of the nanoparticles. We present scaling laws and accurate free-enegy calculations to understand the occurence of the phases of interest, and discuss the implications of our results.

Chapters 3 and 4 deal with fluid membranes. We show how fluid membranes can mediate linear aggregation of spherical nanoparticles binding to them for a wide range of biologically relevant bending rigidities. This result is in net contrast with the isotropic aggregation of nanoparticles on fluid interfaces or the expected clustering of isotropic insertions in biological membranes. We find that the key to understanding the stability of linear aggregates resides in the interplay between bending and binding energies of the nanoparticles. Furthermore, we demonstrate how linear aggregation can lead to membrane tubulation and determine how tube formation compares with the competing budding process. The development of tubular structures requires less adhesion energy than budding, pointing to a potentially unexplored route of viral infection and nanoparticle internalization in cells.

In Chapters 5 – 8, we shift focus to elastic membranes and study self-assembly of nanoparticles mediated by elastic surfaces of different geometries, namely planar,

cylindrical and spherical. Again, a variety of linear aggregates are obtained, but their spatial organization can be controlled by changing the stretching rigidity of the elastic membrane, the strength of the particle adhesion, the curvature of the surface, as well as by introducing surface defects. Furthermore, we show how a fully flexible filament binding to a cylindrical elastic membrane may acquire a macroscopic persistence length and a helical conformation. We find that the filaments helical pitch is completely determined by the mechanical properties of the surface, and can be easiliy tuned. Moreover, we study the collapse of unstretchable (thin) hollow nanotube due to the collective behavior of nanoparticles assembling on its surface, resulting in an ordered nanoparticle engulfment inside the collapsed structure. Our hope is that the results presented in this Dissertation will stimulate further experimental studies of the mechanical properties of fluid and cross-linked membranes, in particular the long range correlations arising due to the particle binding.

Table of Contents

List of Figures

Acknowledgments

My deepest appreciation goes to my advisor, Prof. Angelo Cacciuto, for creating a stimulating and supportive research environment, where I have not only constantly learned, but have also truly enjoyed my day-to-day worklife. His way of thinking, limitless creativity and enthusiasm make him the kind of scientist I aspire to be.

I am also grateful to Prof. Bruce Berne and Prof. David Reichman, for their insightful feedbacks on my second-year defense and original research proposal, and especially for their help with my postdoctoral and fellowship applications. Prof. Sanat Kumar and Prof. Luis Campos have taken the time out of their busy schedules to read my dissertation and attend my defense, which I greatly appreciate.

There are a number of people that have made a contribution to my work and PhD life in the past five years. For a large part of that period, William L. Miller was the only other member of the Cacciuto group, and I could have not asked for a better coworker and a friend. I had the privilege of learning extensively from Dr. Josep Pàmies on my very first projects, as well as from Dr. Behnaz Bozorgui. I was happy to have collaborated with Dr. Chantal Valeriani, Joe Napoli and Stewart Mallory- all of which turned out to be fruitful and a lot of fun. Furthermore, Clarion Tung, Joseph Harder and Katie Klymko were there for me to share food and visions. I would also like to thank many other friends here at Columbia, especially Dani, Alex, Ahmed, Glen and Tim. Many happy hours with them made the chemistry department a much nicer place.

I want to express my sincere gratitude to my family- to my parents for their

unconditional love and support, and to my lovely sisters Tereza, Iva and Magdalena.

Finally, of course, I am thankful to my partner Pavle Trošelj. Living on two continents is not easy, but we made it work, and I'm looking forward to spending the rest of my life with him.

Anđela Šarić

For my sisters

Chapter 1

Introduction

1.1 Self-assembly on interfaces and deformable surfaces

Self-assembly is the process by which initially isolated components spontaneously organize into large, ordered and stable structures. The phenomenon is ubiquitous in nature and is observed across all length scales: "from molecules to galaxies" [1]. At the nanoscale, self-assembly is usually achieved by a complex balancing act between two factors: the direct or effective interactions among the components, and the random thermal fluctuations of the surrounding medium. While the former factor usually determines the morphology and symmetry of the final aggregate, the latter allows the components to diffuse through the medium and explore the available space. Examples of self-assembly, and more in general self-organization of molecules, proteins and protein complexes in biological systems are numerous and are fundamental for the proper functioning of the cell [2–5]. Furthermore, self-assembly is expected to play an important role in the production of materials with novel optical, mechanical, and electronic properties. In fact, whether we are considering organic photovoltaics, photonic crystals with optoelectronic capabilities or energy-saving transistors and LEDs, key to

the efficiency of these electronic materials is a regular and precise spatial organization of their building blocks. Because of the large cost associated with nanolithographic patterning, their large-scale production remains prohibitive, and the process of self-assembly has been put forward as an attractive candidate for a cost-effective solution to the next generation of functional materials.

Although the field of self-assembly has historically focused on molecular systems interacting via covalent interactions, recent advances in particle synthesis [6–12] have significantly extended the structural landscape accessible to colloids that are typically two or three order of magnitude larger than molecules and interact via dispersion forces. Colloidal particles that are anisotropic both in shape and surface chemistry are today easily synthesized, and provide an unlimited number of building blocks that can potentially organize into an unprecedented variety of structures via the process of self-assembly. Unfortunately, self-assembly is a rather delicate and poorly understood process, and the formation of defect-free structures is hardly achievable unless a careful design of the building blocks is performed beforehand.

This dissertation deals with self-assembly on two dimensional fluctuating surfaces, as they can act as powerful universal templates through which arbitrary building blocks of even larger sizes than colloids can be readily driven close to each other thus favoring their aggregation. Spontaneous organization of components adhering to fluid interfaces is a matter of common experience, and is observed across a wide range of length scales: from the assembly of marine litter into large garbage patches and clustering of cheerios on milk at the macroscopic scale, to the aggregation of proteins embedded in lipid membranes at the nanoscale. The first example of small particles assembling onto the interfaces of liquid droplets was reported over a century ago [13], and has been used ever since in industrial processing [14], as well as to produce supracolloidal structures, such as colloidosomes, capsules and nano-particle-based membranes [15, 16]. The effectiveness of bottom-up schemes to organize millimeter-size objects at fluid interfaces in a controlled manner was further demon-

strated by Whitesides and co-workers [17, 18]. The origin of particle aggregation driven by fluid interfaces is very well established [19, 20]. Local deformations in the profile of the interface induced by floating objects adhering to it result in long-range capillary forces that develop to minimize the interfacial free energy that is regulated by its surface tension. By a judicious choice of the interface, and a careful design of the building blocks, a plethora of patterns and even three-dimensional objects can be assembled [21]. For recent reviews the reader is referred to [15, 16, 22, 23].

The work in this dissertation focuses on self-assembly of nanoobjects on surfaces that are not exclusively dominated by their tension and have richer mechanical properties that give rise to a complex response to deformations and peculiar assembly patters. Namely, we are interested in fluid and elastic/tethered membranes. While in the former case the elastic properties are controlled by the tension of the surface and by its bending rigidity, in the latter case surfaces are tensionless but have both bending and stretching rigidities.

The simplest and most important example of fluid surfaces are biological membranes. The main constituents of biological membranes are phospholipids − amphiphilic molecules that spontaneously organize in sheets that stack into bilayers and are capable of forming complex and soft two dimensional geometries. They envelop Eukaryotic cells and compartmentalize their different subcellular regions [2, 24]. Under physiological conditions lipid molecules inside each layer are found in the fluid state and can freely diffuse over the membrane surface. Fig. 1.1a) illustrates the typical structure of a lipid bilayer. The thickness of biological membranes is $t \sim 5nm$, while their surface area is usually many orders of magnitude larger [24, 25]. For instance, the total area of a complex network of membranes in a typical liver cell is 110,000 μm^2, which gives about $8.2m^2$ of membrane area per gram of tissue [2].

Biological membranes are constantly in contact with various macromolecules that either reside on their surface, or are being transported between the cell and its environment as well as shuffled between different compartments within eukaryotic cells.

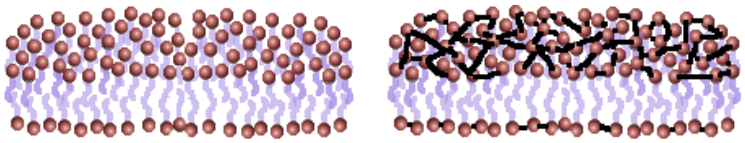

(a) (b)

Figure 1.1: Schematic representation of a fluid (a) and a crosspolymerized (elastic) (b) membrane.

Since a lipid membrane is permeable only to water and small uncharged molecules [25], all macromolecules that are required to interact with it or cross it need to do so by locally deforming the surface upon binding and subsequently either organize upon adsorption or possibly vesiculate away from it. Self-assembly on biological membranes is thus a crucial step in cellular transport, signaling and recognition. Being able to control this process is of central interest for designing particles for targeted-drug delivery and for understanding nanotoxicity [26, 27]. It has also promising applications in nanopatterning and nanotechnology [28], in medical imaging [29] and in development of biosensors and functional biomimetric materials [30, 31]. In addition to phospholipids, many other amphiphilic molecules are capable of building bilayer membranes, for example blockcopolymers and surfactants [32–34], and recently membranes made of colloidal particles have been successfully assembled [35].

Unlike in their fluid counterparts, the building blocks of elastic membranes do not diffuse, but are tethered to each other as sketched in Fig. 1.1b. As a result, the elements of elastic membranes cannot flow and can withstand shear [36]. Examples of such surfaces are cross-polymerized membranes [37], gels [38], actin-spectrin networks of red blood cells' cytoskeleton[39, 40], membranes made of close-packed nanoparticles[41], graphene and graphite-oxide sheets [42–45] and polymer films [46]. Their study has seen a drastic increase over the past decade due to their potential use in flexible electronics [47], artificial skin [48] and as blood cells substitutes [49], tunable diffraction gratings [50], and in stimulus responsive materials and soft-robotics [51].

Although much of the elastic properties of elastic sheets or shells is by now well understood [36], very little is known about their properties as self-assembly templating agents.

This dissertation discusses how self-assembly of nanoparticles and colloids can be driven by soft, deformable surfaces, with emphasis on biological and elastic membranes. Specifically it is focused on adsorbed particles that are at least one order of magnitude larger than the membrane thickness and do not disrupt the molecular structure of the underlying surface nor do they pierce through it in any way.

1.2 Organization of this dissertation

This dissertation is organized as follows.

We begin by providing a physical description of fluid and elastic membranes, followed by a brief overview of accepted theories of self-organization on membranes, and computer models for their simulation, as detailed in Chapter 2.

In Chapters 3 and 4 we focus on nanoparticles adsorbed on fluid membranes. Chapter 3 discusses how lipid membranes can mediate linear aggregation of spherical nanoparticles binding to it for a wide range of biologically relevant bending rigidities. It is based on work published in [121].

Chapter 4 deals with membrane tubulation driven by large colloidal particles. We detail the mechanism behind it and investigate how the tube formation compares with the competing budding process. It is based on work published in [122].

Starting with Chapter 5 we shift our focus to elastic surfaces and show how the linear aggregates of adsorbing nanoparticles are again favorable, but that the stretch-

ing rigidity of the underlying surface controls the morphology of linear aggregation. It is based on work published in [123].

In Chapter 6, we begin to consider elastic surfaces of various geometries. In this Chapter we show how a flexible filament binding to an elastic cylindrical surface may acquire a macroscopic persistence length and a helical conformation. It is based on work published in [124].

Chapter 7 focuses on radial collapse of unstretchable (thin) hollow nanotubes under adhering nanoparticles. This work is currently under review [125].

Finally, in Chapter 8, we study nanoparticle self-assembly on spherical elastic shells. This case yields the largest variety of patterns, due to its peculiar topology and inevitable presence of surface defects. It is based on work published in [126].

Chapter 9 gives a brief summary of the results presented in this Dissertation, and outlines future directions in relation to this work.

Chapter 2

Physical properties and modeling of membranes

2.1 Deformable surfaces

When a particle adhering to a surface is at least one order of magnitude larger than the surface thickness, it is reasonable to neglect the surface molecular details. In this limit a particle will experience the surface as a continuous medium (see Fig. 2.1a) for an illustration) having specific mechanical properties. For a lipid membrane the standard elastic representation is given by the Helfrich free energy [25, 52, 53] and contains a curvature F_c and a surface tension F_γ term:

$$F = F_c + F_\gamma = \int dA \left[\frac{\kappa}{2}\left(H - H_0\right)^2 + \kappa_G K\right] + \int \gamma \, dA \tag{2.1}$$

where $H = 1/R_1 + 1/R_2$ is the mean curvature, $K = 1/(R_1 R_2)$ is the Gaussian curvature, R_1 and R_2 are the principal radii of curvature at a certain point on the surface A, and the constant H_0 is the surface spontaneous curvature. κ, κ_G and γ are respectively the bending rigidity, the Gaussian rigidity and the tension of the surface.

The bending rigidity κ for biological membranes can be estimated as the cost to compress the inner leaflet of the bilayer and stretch the outer one exposing some of its

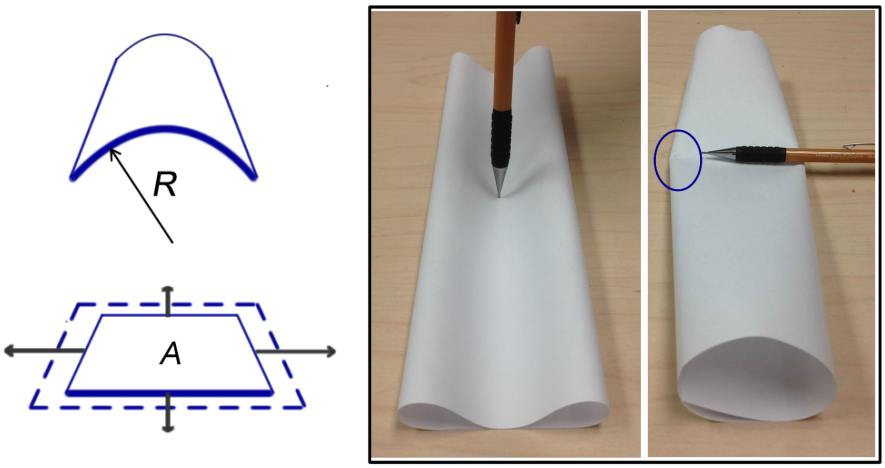

(a) (b)

Figure 2.1: (a) A bending (top panel) and a stretching (bottom panel) deformation of a thin sheet. (b) Stretch-free deformation along a zero-curvature direction on a thin cylinder (left panel). d-cone formed as a result of a stretch-inducing deformation (right panel).

hydrophobic area to water [24, 25]. Experimentally measured values of κ are found to be in the range of $10 - 30 k_{\mathrm{B}}T$, where T is the temperature and k_{B} is the Boltzmann constant; the exact value depends on molecular composition. Unfortunately, no methods are available for a direct measurement of the Gaussian rigidity κ_G, as a result its value is much more uncertain. To date, the only assessment for a pure phospholipid system yielded $\kappa_G \approx -0.9\kappa$ [54]. In most treatments of membranes, the Gaussian curvature term of the Helfrich free energy is neglected as κ_G is a measure of the energy cost associated to topological changes of the surface, and it is constant as long as the surface topology remains unaltered.

The bending rigidity of artificial fluid membranes can be tuned by changing the properties of their building blocks. κ for surfactant membranes grows quadratically with the length of the surfactant molecule, and depends on the surface area per surfactant polar head [32, 33, 55]. Surfactant membranes are relatively soft with

$1k_BT \leq \kappa \leq 10k_BT$ [55]. Analogously, the rigidity of block-copolymer membranes greatly depends on the molecular weight of the copolymer [56] and can be as low as $10k_BT$ and as high as $100k_BT$ [56, 57]. Fluid membranes made of colloidal rods are reported to be quite stiff and have $\kappa \approx 150k_BT$ [35].

Although measured values of surface tension γ of lipid membranes vary significantly, most studies assume a negligible or a very small value $\gamma \approx 10^{-3} - 10^{-2} pN/nm$, depending on the conditions of the experiment and the presence of a lipid-reservoir [25, 58]. The surface tension of polymeric membranes has been shown to be relatively independent of molecular weight, with similar values as those reported for lipid membranes [32]. Therefore, the behavior of fluid membranes in the limit of small deformations is mostly governed by the bending energy.

Let us now consider the physical properties of elastic/tethered membranes. They do not have surface tension, but are resistant to stretching and respond to perturbations away from their equilibrium shape in a spring-like fashion. Their free energy can be decomposed in two contributions: a curvature term F_c that has the same form of that introduced for fluid surfaces, and an elastic term, F_e, that accounts for the stretching energy (see Fig. 2.1a) for an illustration) and can be expressed in terms of the surface Lamé coefficients μ and λ [36] as

$$F_e = \frac{1}{2} \int dA \left(2\mu u_{ij}^2 + \lambda u_{jj}^2 \right). \tag{2.2}$$

Here u_{ij} is the two-dimensional strain tensor that can be written in terms of the in-plane displacement vector field u_i and the out-of-plane displacement field h[36] with respect to the unstressed planar reference surface

$$u_{ij} = \frac{1}{2} \left(\nabla_i u_j + \nabla_j u_i + \nabla_i h \nabla_j h \right). \tag{2.3}$$

The last term in the above equation preludes to a non-trivial coupling between in- and out-of plane deformations. In this representation, also known as the Monge

gauge [25], the bending free energy can be approximated (for $H_0 = 0$) to

$$F_c = \frac{\kappa}{2} \int dA \left(\nabla^2 h\right)^2, \tag{2.4}$$

It can be shown that the Lamé coefficients are related to the Young's modulus of the sheet by a simple relation $Y = \mu(3\lambda + 2\mu)/(\lambda + \mu)$, while the bending rigidity scales as $\kappa \sim Yt^3$; here t is the thickness of the sheet [36].

A very important property of thin elastic sheets can be readily obtained by considering the ratio between the cost associated to stretching and that associated to bending deformations. A simple scaling analysis reveals that $F_c \sim Yt^3h^2/L^4$, and $F_e \sim Yth^4/L^4$, where L is the lateral length of the surface, and the ratio between the two terms scales as

$$q = F_e/F_c \sim (h/t)^2 . \tag{2.5}$$

This equation states that whenever the extent of the deformations applied to an elastic sheet is larger than the surface thickness, bending is the preferred mode of deformation. Furthermore, it is also possible to show that the strain tensor is simply related to the principal radii of curvature, c_1 and c_2, of a small deformation imposed on a planar surface, namely $u_{xy} \simeq c_1 c_2 xy$ [59]. This relation, intimately related to the above-mentioned coupling between u_i and h, implies that the only stretch-free deformations possible on an elastic sheet are those involving a single axis of curvature, i.e. either c_1 or c_2 must be equal to zero. These two results have a profound effect on the way thin elastic surfaces respond to deformations, and are at the core of most of the phenomenological behavior experienced with thin elastic materials. For instance, spherical shells have no stretch-free deformations as any perturbation of the spherical shape necessarily involves two axes of curvature. The resulting conformations involve stress-focusing by buckling[59], as readily observed when poking a table tennis ball. Fig. 2.1b shows examples of a stretch-free and a stretch-costly deformation on a cylindrical shell. Skin wrinkling under applied stress [60] and stress focusing via d-cone formation of crumpled paper [59] are two beautiful examples of this phenomenon that has a strong geometrical dependence.

2.2 Membrane-mediated interactions

Nanoobjects that interact with fluid membranes can be either adsorbed on the membrane surface or embedded in the bilayer, in which case we will call them inclusions. In either case, adsorption or inclusion of a nanoparticle locally perturbs the membrane surface in a way that depends on the shape and size of the nanoparticle and the nature of its interaction with the membrane. The tendency of the membrane to minimize the size of these perturbations can result in effective interactions between the adsorbed/included nanoparticles. These forces can be either attractive or repulsive as schematically shown in Fig. 2.2. Theoretical studies of the these phenomena for fluid membranes go back over two decades and there are a number of excellent reviews on the subject [61–63]. Nonetheless, the field is still developing, and new findings and improvements of the theories are constantly being reported.

There are several ways for a membrane to induce interactions between embedded particles. In the simplest case of an isotropic particle perfectly included in the bilayer (Fig. 2.2a)), a Casimir-like interaction is known to develop for a range of particle separations. In general, nanoparticles are much stiffer than the membrane, and their presence perturbs the spectrum of natural membrane fluctuations. The extent of the perturbation depends on the separation r between the nanoparticles, and is minimized when they are brought together, leading to an effective nanoparticle-nanoparticle attraction [64–66] of the form $V(r) \sim -1/r^4$. Although long-ranged, its magnitude and importance are still under debate.

Often the presence of membrane inclusions locally alters the thickness of the hydrophobic core of the bilayer resulting in its distortion near the inclusion perimeter. As illustrated in Fig. 2.2b), this typically leads to either a local compression or expansion of the surface [67–70]. Whenever two adjacent inclusions deform the bilayer in the same way (both are thinner or thicker than the unperturbed membrane's hydrophobic region), the boundary deformations are minimized upon their aggregation, giving rise to a short-range attraction. When the inclusions alter the membrane

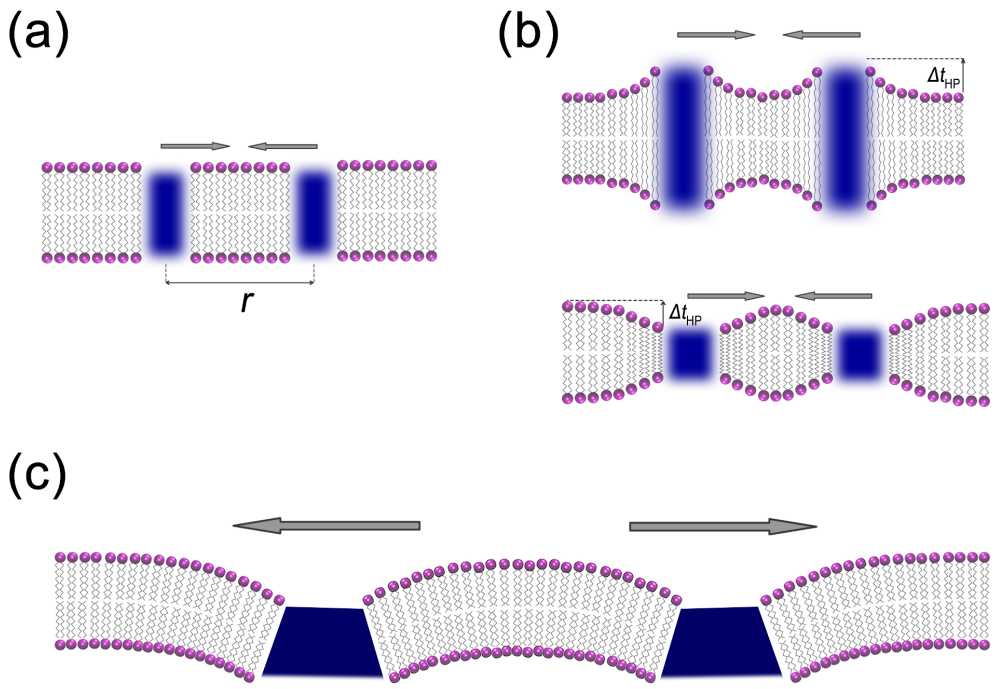

Figure 2.2: Illustrations of membrane-induced interactions between inclusions. (a) Casimir-like attractions between particles perfectly included in the bilayer. (b) Hydrophobic missmatch: like deformations attract. (c) Bending-mediated repulsion between like deformations.

thickness in an opposite manner (one thins it out and the other one thickens it), the resulting interaction is repulsive. In both cases the energy cost of the deformation increases as the square of the hydrophobic mismatch length Δt_{HP}, but it is mainly constant and with a limited range of interaction (several nm) [62, 68]. This interaction is of great importance for the organization of transmembrane proteins and other membrane inclusions.

Another very important membrane-mediate interaction is more readily linked to local bending deformations. Consider for instance the deformation caused by an adsorbing nanoparticle attracted to a membrane as it tries to locally bend it to maximize their surface contact, or the deformations enforced by membrane inclusions that are not symmetric with respect to the bilayer mid-plane (Fig. 2.2c)). When the deformation profiles induced by different nanoparticles are close enough to overlap, an effective interactions take place [64, 65, 71]. In the limit of shallow deformations, like-indentations repel, while oppositely-curved indentations attract. The bending mediated interactions are of a longer range than the hydrophobic mismatch and decay with particle separation as $V(r) \sim 1/r^4$. They are considered to be very important for many membrane-associated aggregation processes. Recently, Deserno et al. have considered interactions between strongly curved deformations, and have showed that a crossover from repulsion to attraction takes place as the deformation deepens [72]. Moreover, Fournier et al. studied anisotropic deformations, and have showed that orientationally-dependent attractions are also possible [73].

The global shape of the membrane can also be used to sort particles in different regions and favor phase segregation in multi-component systems. For instance, membrane-bending particles tend to aggregate in the regions of the membrane whose curvature is the most similar to their own − thus maximizing their surface contact at a minimum cost in bending [74, 75]. Analogously, when clustering of like-membrane-bending particles occurs, due for example to phase separation between different components [76, 77], large shape deformations on an initially flat region of the membrane

can develop for easily bendable surfaces. When the bending energy is non-negligible, micro-phase separation into repulsive bulged phases will occur, resulting in a finite-spaced membrane domains, providing yet another mechanism of membrane-induced ordering [78]. This complex coupling between particle self-assembly and surface deformability is central to understanding intra- and extra cellular communication in Eukaryotic cells [79–83].

Unlike fluid membranes, only particle adsorption is possible on elastic surfaces, and they respond to it by bending and stretching. The treatment of the bending part of the deformation is identical to that described for fluid membranes, however, very little is known on the role of the stretching energy in the pair-wise interaction between the deformations. The main difference from fluid membranes is that the topology and the geometry of the surface play a much more important role in the response of elastic surfaces to deformations. Simply put, depending on the elastic parameters and geometry of the surface, different directions on the surface might not be equivalent. Of particular interest are thin elastic surfaces for which the stretching dominates over the bending energy resulting in global constraints involving exclusively (whenever possible) uni-axial deformations. Additionally, the presence of defects in elastic networks may also play an important role, since defects might be more or less prone to deformation compared to the rest of the surface, and might attract or repel particles [84]. These phenomena give rise to orientational interactions between deformations and lead to more complex and beautiful aggregation patterns.

2.3 Computer simulations of deformable surfaces

A large number of membrane models has been put forward to describe soft surfaces across all length scales. Not surprisingly, most of them have been developed for biological membranes, although models for surfactant and polymer membranes are also available [85–88]. Our goal here is not to review all existing membrane-simulation

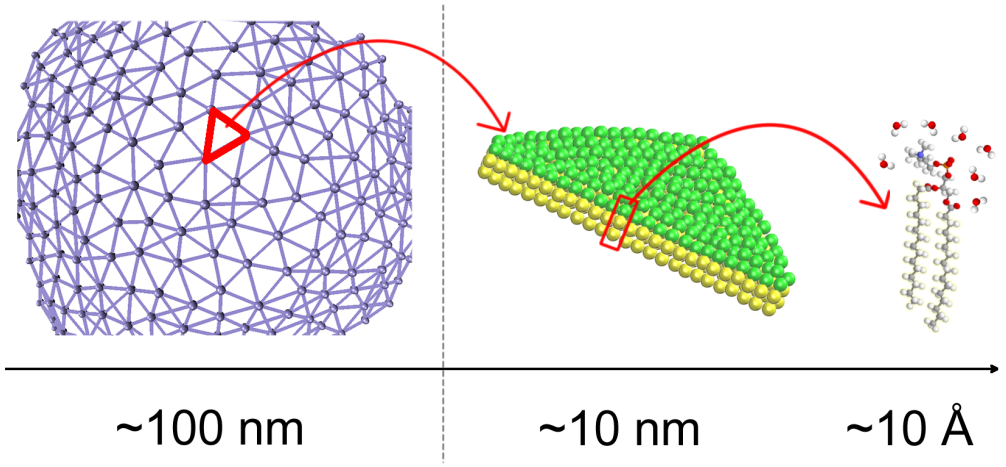

Figure 2.3: From implicit to full atomistic: schematic illustration of representative membrane models at different length scales. From left to right: triangulated network, three-bead per lipid coarse-grained (CG) model, atomistic representation.

techniques, but to give a brief overview of representative models at different scales, with focus on their applications in simulating membrane interactions with macromolecules. An overview of representative models is sketched in Fig. 2.3. Detailed reviews on various techniques and their evaluation can be found in References [53, 89–92].

Membrane systems can be modeled either as continuous surfaces, using the mathematical functions described in Eq. 2.1 and 2.2, or with a particle-based representation where each lipid/building-block is depicted explicitly with more or less degree of coarse-graining. A common approach in continuous models includes writing all energy contributions in the framework of the Helfrich elastic model and performing numerical energy minimization with system-dependent constraints. This process is relatively fast and computationally inexpensive, but an analytical expression of all energy contributions in the system is not always trivial. This is especially true in the case of complex membrane-particles systems where multi-body interactions and unexpected geometrical realizations of the membrane and nanoparticles can occur.

In addition, this technique does not capture thermal effects or the dynamics of the system, although a few dynamical continuous models have been developed. Let us just mention Fourier space Brownian dynamics [89], which evolves the free energy of a lipid bilayer in the Fourier space in the presence of arbitrary forces, and includes hydrodynamics as well as thermal fluctuations.

Particle-based models are more versatile and can be applied to arbitrary geometries and number of components. However, they need to satisfy the non-trivial task of keeping membrane integrity while maintaining its fluidity. They can be roughly classified in two groups, depending on whether the bilayer structure is described explicitly or implicitly [92]. Models in the first group describe each amphiphilic molecule separately and can be fully atomistic or coarse-grained. Implicit models depict a membrane as a coarse-grained surface where a unit segment does not represent a single molecule, but a membrane patch consisting of hundreds to thousands of amphiphilic molecules. The most detailed, full atomistic, models explicitly account for each atom of an amphiphilic molecule via molecular mechanics, sometimes employing the united atoms approach to represent nonpolar alkyl groups of the hydrocarbon tails, and a set of interaction parameters are then given by the chosen force field. Such a level of detail is necessary when studying membrane interactions with small molecules or the inner-working of transmembrane channels. Nowadays these simulation are benchmarked at about hundred fully hydrated lipids for $50-100ns$. A nice review on recent developments of membrane force-fields can be found in Ref. [93].

For simulation of membrane interactions with larger nano-components, this detailed description is unnecessary and unfeasible, and several coarse-graining techniques have been developed. An amphiphilic molecule can be coarse-grained by forming groups consisting of 2-5 heavy atoms into a single coarse-grained (CG) site, with water included either explicitly or implicitly via effective potentials. Further coarse-graining is achieved by a systematic decrease in the number of CG sites- up to two or three segments [94–96] or even just one spherocylinder for the whole lipid

molecule [97] with the solvent represented via an effective attractive potential between hydrophobic parts. Particle-based explicit models that include some degree of depiction of the lipids require a large number of explicit or effective water molecules to provide osmotic pressure and stabilize the surfaces against lipid evaporation. A rough estimate is at least 30 molecules of water per lipid [90], and this increases the computational cost by at least an order of magnitude. For this reason water-free membrane models have become very popular, however, the parametrization of such models is less straightforward and a large variety of ad-hoc potentials have been suggested. Most of them are based on modifications of a Lennard-Jones potential [95, 96]. Although all of the proposed potentials are able to reproduce membrane self-assembly, the resulting values of membrane rigidities are hard to control and range between several $k_{\mathrm{B}}T$ up to over $100k_{\mathrm{B}}T$ [90]. Effective potentials for CG simulations of biological membrane can also be derived from atomistic simulations of lipids in water using a multiscaling approach, either via force-matching or by employing hybrid algorithms [98]. Each of these approaches has its strengths and weaknesses, see for instance Ref. [91, 99, 100], but all of them have been employed to attack important biophysical questions.

In the second group of particle-based models, the membrane is built from units that represent a coarse-grained surface patch rather than an individual molecule. Since they ignore the details of the bilayer, these models are valid only for a description that involves length-scales sufficiently larger than the membrane thickness ($\gg 5nm$). The mechanical properties of the bilayer are reflected in the values of a set of elastic parameters associated with the Helfrich free energy. The strength of this group of models is that they give access to larger length and time scales unobtainable by explicit-lipid models.

The standard physical representation in this class is the triangulated-network model, which is the model used to simulate fluid membranes in this Dissertation. Here the membrane is described as an infinitely thin elastic surface consisting of hard, spherical beads connected by flexible links to form a triangulated mesh [101–104].

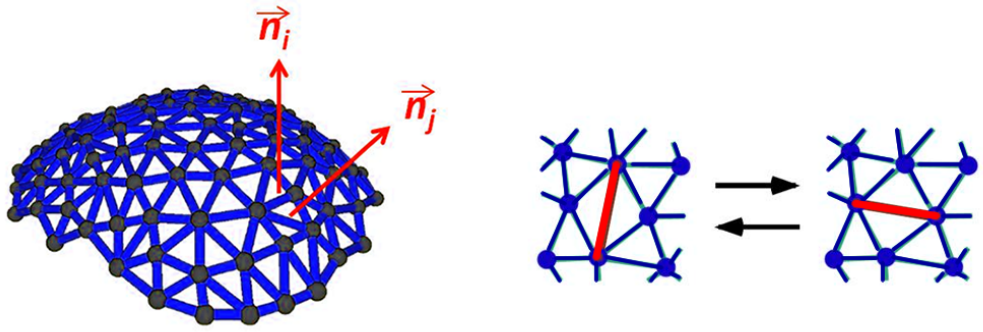

Figure 2.4: Triangulated-network model for fluid membranes. Left panel: the membrane bending energy acts on neighbouring triangles, according to Eq. 2.6. Right panel: the mesh connectivity is dynamically rearranged to incorporate surface fluidity.

Using Monte Carlo (MC) methods, the mesh connectivity is dynamically rearranged to incorporate surface fluidity. The membrane bending energy acts on neighbouring triangles, and has the typical form

$$H_{ij}^{c} = \frac{\kappa}{2}(1 - \mathbf{n}_i \cdot \mathbf{n}_j)\,, \tag{2.6}$$

where $\mathbf{n}_i$ and $\mathbf{n}_j$ are the normals of two triangles i and j sharing a common edge, as illustrated in Fig. 2.4. The cost associated with area changes is usually included via the energy term

$$H_{\gamma} = \gamma A, \tag{2.7}$$

where A is the total surface area. Since membrane beads are connected by dynamic bonds, this model cannot account for topological changes, such as poration or budding-off.

A closely related representation is the meshless model, where membrane beads are polar and are not held together by imposed bonds, but they self-assemble into a membrane by carefully designed potentials. Most of these potentials consist of three distinct interactions: a repulsive part that ensures volume exclusion, an attractive

part that drives membrane self-assembly, and an angular part that depends on particle orientation and mimics the membrane bending rigidity. Meshless models can capture membrane topological changes and dynamics, but in the majority of them the membrane elastic properties are not included into the system in the as external parameters, but are encoded into the details of the pair potentials between the membrane beads and need to be extracted by analyzing the fluctuations spectrum of the surface or by other means. The first meshless model was proposed by Drouffe et al. in 1991 [105] and has relied on multibody interactions. Recently, a few pairwise-additive meshless models have been reported [106–108]. An alternative meshless model, in which particles have no internal degrees of freedom and the potentials depend only on particle positions, can be found in [109]. It is important to emphasize that the size of a surface bead in triangulated-network model as well as in the meshless model is not related to the membrane thickness, but rather to the coarse-graining length-scale of the membrane surface, and should be large enough, $\sigma \simeq 30 - 50$ nm, so that an elastic description of the membrane is acceptable.

Tethered membranes can also be described employing continuum elastic models, however simulations of elastic membranes in contact with nanoobjects have been mostly performed using particle-based elastic models. The simplest particle-based model for an elastic membrane is a fixed-mesh (network) model [101, 104, 110]. It is a predecessor of the triangulated-network model for fluid membranes, without the bond-flip to maintain the interparticle-connectivity fixed. The bending energy can be incorporated using Eq. 2.6, while the shear elasticity/stretching energy can be accounted for through the strength of harmonic bonds between linked surface beads:

$$H^e_{mn} = K_s(r_{mn} - r_b)^2 \tag{2.8}$$

where K_s is the spring constant, r_{mn} is the distance between two neighbouring beads m and n, and r_b is their equilibrium bond length. Special attention has been given to elastic models of a red-blood-cell membrane [111–114], where effects of both fluid and

elastic membrane can be of importance for different purposes. Beyond the standard fixed-mesh model, they have been described by attaching an elastic network on the bilayer membrane as in [115]. A few alternative schemes have also been proposed, including the coupling of the elastic network with the hydrodynamics of the surrounding solvent [92, 113, 116].

Finally, a full description of the systems of interest requires a representation of the nanoobject-membrane interaction. Adsorption of a nanoobject can take place in different ways, for instance it can be induced by binding of ligands on the nanoparticle to receptors on the surface on the membrane, such as streptividin-biotin links, but it can also be driven by van der Waals interactions, or by electrostatic physysorption for charged membranes and nanoparticles. Particle inclusion within the bilayer is usually driven by hydrophobic effects. These interactions in atomistic models arise from first principles calculations, while in coarse-grained models they are usually included via a generic short-range attractive potential between a nanoobject and each membrane-building particle, and can be described with simple functional forms ranging from Morse to truncated Lennard-Jones potentials. These short-ranged attractions adequately account for the ligand-receptor or van der Waals interactions.

Chapter 3

Fluid membranes can drive linear aggregation of adsorbed spherical nanoparticles

3.1 Introduction

Lipid membranes have unique mechanical properties that are crucial for many biological processes, including cellular recognition, signal transduction, inter- and intracellular transport, and cell adhesion. Most of these processes require interactions of a lipid-bilayer with a variety of nano- and micro-size objects, such as proteins, DNA, viruses and other biomacromolecules. Along with its fundamental importance, understanding the interactions of fluid membranes with nano-objects is a crucial component in targeted drug-delivery design and in nanotoxicity studies.

Lipid membranes are typically very flexible and under thermal perturbations they undergo surface deformations that are significantly larger than their thickness. Because of such a flexibility, they can easily be deformed when interacting with nanoparticles that can be either adsorbed on the membrane surface or embedded in the lipid bilayer. As discussed in Chapter 2.2, the resulting membrane deformations may

in turn mediate interactions between the membrane-bound objects. Adsorption or inclusion of objects comparable in size to the membrane thickness ($\sim$ 5nm) greatly perturbs the local packing of the lipids leading to quite complex phenomena dependent on the molecular details of the membrane-object interactions. When considering larger objects, on the contrary, it becomes feasible to describe the membrane as a continuous surface and coarse-grain its interactions with the nanoscopic objects with generic binding potentials. Here we are interested in membrane driven interaction between adsorbing colloidal particles that are more than one order of magnitude larger than the membrane thickness. Despite their structural complexity, for sufficiently large scales the behavior of lipid membranes can be described by a small number of elastic parameters that capture their response to deformation; a bending rigidity κ_b of the order of $10k_{\rm B}T$, and a small surface tension $\gamma \approx 10^{-2} - 10^{-3} pN/nm$ are the most important ones. Both can be altered either by dispersing within the bilayer additional molecular components, or by changing the lateral forces/osmotic pressure applied on the membrane.

In this Chapter we show that spherical nanoparticles adhering to fluid membranes can self-assemble into a variety of two-dimensional aggregates. Significantly, for intermediate and biologically relevant values of the bending rigidity we find that particles preferentially arrange into linear/flexible aggregates. This result is in striking contrast with most of the theoretical studies on membrane inclusions that predict isotropic aggregation when the embedding object imposes an isotropic deformation on the surface. Linear aggregation is expected only for sufficiently anisotropic wedge-like local deformations [73], and this is clearly not the case for spherical nanoparticles. We find that the key to understand the stability of linear versus isotropic aggregates resides in the interplay between bending and binding energies of the nanoparticles. The latter term, usually and correctly neglected when dealing with embedded nano-components, does indeed play a major role in the structural morphology of the aggregates formed by non-embedded adhering components.

It should be stressed that string-like formations very similar to those we present here have been observed experimentally in several systems. To best of our knowledge, Safinya et al. have been the first to experimentally investigate membrane mediated attraction of colloidal particles bound to a lipid membrane [75]. They studied two systems: streptavidin-grafted latex beads (0.3 and 0.9 μm in diameter) attached to a biotinilated phospholipid giant unilamellar vesicles (GUV) and negatively charged colloidal DNA-lipid aggregates adsorbed on cationic GUVs. Their experiments revealed that in both cases particles caused deformations of flexible GUVs and experienced membrane mediated attraction. Vesicles with a single attached bead showed distorted contours with a pinched angle around the bead. If the vesicle was not spherical, but had a stomatocyte shape, the bead would preferentially bind to the concave region of the vesicle. This maximizes particle binding energy, with as little bending cost as possible. When a second bead was added to the system, the two beads approached each other over a period of time and eventually bound. The lipid mobility was a prerequisite for aggregation, and particles showed no tendency to aggregate in solution, excluding the possibility of particle attractions without the presence of the membrane. Interestingly, upon addition of the third particle a chain-like triplet was formed on a spherical vesicle, as opposed to a triangular formation which would be expected in isotropic aggregation. Remarkably, in a multi-particle system, a ring shaped string of beads aggregated around the waist of a multilamellar vesicle as shown in Fig. 3.1, clearly exhibiting a peculiar non-isotropic attraction. A close packed hexagonal cluster of colloids was observed only when the vesicle was not symmetric and had a concave region as a preferred binding site. Similarly, the cationic lipid-DNA complexes of low net charge assemble into linear colloidal aggregates when adsorbed to the cell membrane [128].

Concurrently with our work, Yue and Zhang have performed computer simulations of receptor-mediated endocytosis of multiple nanoparticles [129]. Uptake of nanoparticles in cells and GUVs is often preceded by nanoparticle clustering, as regularly

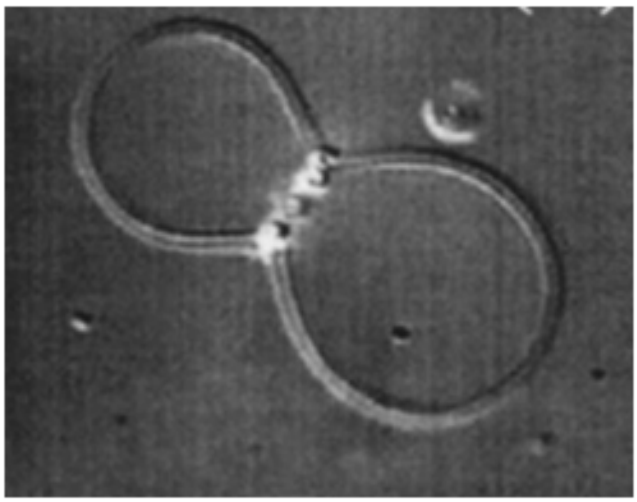

Figure 3.1: Latex beads bound to a multilamellar vesicle via biotin-streptavidin interactions forming linear string-like aggregates. Reprinted from Ref. [75].

observed in experiments [130]. The authors have shown that membrane-mediated interactions between adsorbed nanoparticles are strongly sensitive to their size. They have found small nanoparticles ($\sim 2.5nm$) to exhibit short-range attractions and to aggregate in hexagonal structures. Nanoparticles of intermediate size ($\sim 4.5nm$), once partially wrapped by the membrane, experience longer range interactions that connect them in a linear arrangement, very much like the pearl-like chains observed by Safinya et al [75, 128]. For larger nanoparticles ($\sim 6.5nm$) the membrane dynamics slows down significantly, as the number of receptors required to be recruited to deform the membrane becomes large. In that case individual-wrapping of each nanoparticle has been observed, except when the nanoparticles were initially next to each other, which leads to wrapping of the whole dimer. Zhang et. al attribute this aggregation patterns to membrane-mediated interactions, which are strongest for small, highly-curved particles, and decrease with the particle size. Furthermore, they argue that the interactions are attractive for the small sized particles and repulsive for the big ones. This however does not explain the switch form isotropic to anisotropic aggregation. Nanoparticles of size comparable to the membrane thickness

can considerably disturb the local lipid packing. The resulting deformations induced on the membrane are complicated, but the net effect seem to be analogous to that induced by hydrophobic mismatch leading to the familiar short-range isotropic attraction when like deformations of individual particles overlap. Less well understood is the scenario in the large particle limit. In this Chapter we use a combination of numerical simulations and scaling arguments to detail the physical origin behind it.

3.2 Simulation details

We performed Monte Carlo simulations of planar and spherical fluid membranes interacting with adsorbing nanoparticles. The membrane is modeled using a simple one particle-thick solvent-free model, and consists of N hard spherical beads, of diameter σ, connected by flexible links to form a triangulated network [101, 102, 104] whose connectivity is dynamically rearranged to simulate the fluidity of the membrane, as detailed in Chapter 2.3. The membrane bending energy acts on neighboring triangles, and has the form given by Eq. 2.6, with κ_B being its bending rigidity. γ is the tension of the surface and is included in the cost associated with area changes via Eq. 2.7.

A nanoparticle is modeled as a sphere of diameter $\sigma_{np} = Z\sigma$, with $Z = 3, 4$ or 6. Excluded volume between any two spheres in the system (nanoparticles and surface beads) is enforced with a hard-sphere potential. Finally, the nanoparticle-to-surface adhesion is modeled via a generic power-law potential between the nanoparticles and the surface beads defined as

$$V_{\text{att}}(r) = -D_0 \left(\frac{\sigma_M}{r}\right)^6 \tag{3.1}$$

with $\sigma_M = (\sigma + \sigma_{np})/2$, and cutoff at $r_{\text{cut}} = 1.5\sigma_M$. Following [131], simulations of the planar membrane were carried out in the $N\gamma T$ ensemble, while the NVT ensemble was used for the spherical membrane. Each simulation was run for a minimum of $5 \cdot 10^6$ steps. In each simulation the number of nanoparticles is held constant, and

the surface tension is set to $\gamma = 3k_{\mathrm{B}}T/\sigma^2$. For $\sigma \approx 30 - 50nm$ we have nanoparticles of diameter $\sigma_{np} = 100 - 200nm$ and surface tensions $\gamma \approx 10^{-2} - 10^{-3}pN/nm$.

3.3 Phase behavior

We begin by computing the phase behavior of the system for different values of the surface bending rigidity κ_b and nanoparticles' adhesive energy D_0. The results are summarized in the left panel of Fig. 3.2, and report the structure of the aggregates observed for each pair $[\kappa_b, D_0]$ in the case of the planar geometry.

A gas phase occurs when D_0 is too weak for the particles to deform the membrane. In this phase particles are just lightly bound to the surface, they are highly mobile, and have a certain probability of detaching from it. An arrested phase occurs for large values of D_0. In this case particles bind very strongly to the membrane resulting in large local deformations that heavily limit their mobility over the surface. This typically leads to configurations that are kinetically trapped or even to nanoparticle engulfment. Three ordered phases occur for moderate values of D_0. Each of the three phases spans a range of κ_b values. For small values of the bending rigidity, particles create well defined deep-spherical imprints in the membrane and organize into ordered hexagonal arrays (**H1**). Low cost in bending energy and high gain in surface binding allows for these deep deformations. In this phase the nanoparticles are not in direct contact with each other, but are separated by the pinched parts of the membrane. Close-packing maximizes sharing of the pinched regions between neighboring nanoparticles, thus maximizing the surface-to-nanoparticle contact area. An identical result is obtained when repeating the simulations on the spherical membrane, and is reminiscent of the experimentally observed two-dimensional hexagonal crystal formed by negatively charged particles on positively-charged surfactant vesicles reported in [132]. Even in this case the colloids are extensively wrapped by the membrane and are not in direct contact with each other.

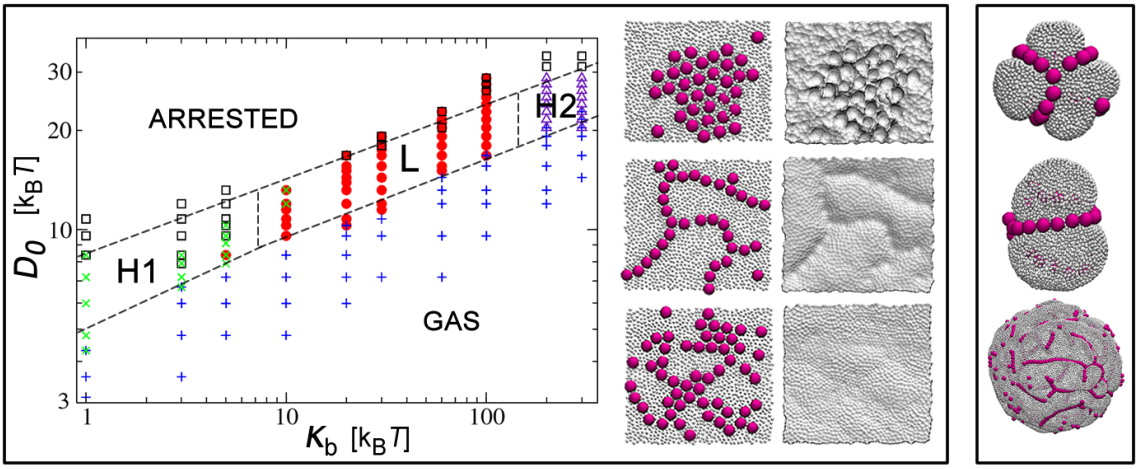

Figure 3.2: Left panel: Phase diagram of particle self-assembly on a fluid surface in terms of the surface bending rigidity κ_b and particle binding energy D_0. The snapshots show typical aggregates in the **H1**, **L** and **H2** phases in a top-to-bottom order, and the deformation pattern they leave on the membrane. The membrane-area is $A \simeq (40 \times 40)\sigma^2$, the nanoparticle-size $\sigma_{np} = 4\sigma$ and their surface fraction $\rho = 0.27$. Right panel: Snapshots of the linear aggregates on the spherical membrane. The upper two snapshots show the system of $R \simeq 15\sigma$, $\sigma_{np} = 4\sigma$ and $\rho = 0.11$ and the bottom snapshot depicts $R \simeq 45\sigma$, $\sigma_{np} = 3\sigma$ and $\rho = 0.16$.

For biologically relevant values of κ_b, our nanoparticles create smooth channel-like distortions on the membrane and self-assemble into linear aggregates (**L**) non unlike those predicted for anisotropic membrane inclusions [73]. Although we have not computed a structural phase diagram for our vesicle model, we find that the simulations on the vesicle performed at different nanoparticle concentrations and vesicle radii lead to analogous results. Here particles form sinuous linear patterns that tend to follow the equatorial lines of the vesicle. Snapshots from our simulations are shown in the right panel of Fig. 3.2. This phase strikingly resembles the linear aggregates of colloidal particles on Giant Phospholipid Vesicles obtained by Safinya et al. [75].

For very large values of κ_b the nanoparticles re-organize into the familiar hexagonal lattice, however, unlike what happens for the small κ_b aggregates, the membrane now remains almost completely flat and the nanoparticles are in contact with each other (**H2**). Because of its high stiffness, particles can only weekly deform the membrane to gain in binding energy, as a result the binding energy is minimized by recruiting the largest number of membrane beads in the vicinity of the nanoparticles. This effectively drives the crystallization of the region of the membrane that directly interacts with the nanoparticles, creating a line tension between crystalline and fluid membrane regions that is minimized when isotropic aggregation takes place [77, 81].

As mentioned before, the formation of linear aggregates is quite surprising. To ensure that our results are not affected by the triangulation underlying the definition of our membrane model, we repeated our simulations using the coarse-grained, but tether-free model proposed by Zhang et al. [107]. This model also accounts for possible topological changes in the surface, however the elastic properties of the membrane are not fed to the system in the form of parameters of an elastic energy, but are encoded into the molecular details of the anisotropic pair potentials between the effective building blocks of the membrane, and need to be extracted by analyzing the fluctuations spectrum of the surface [107], or by other means. It is comforting

to report that no qualitative difference was found on the overall phenomenology of the phase diagram: linear aggregates do indeed form and are not an artifact of our model. We also checked that linear aggregates do no form when limiting the area of the particles' binding region to enforce a finite (constant) contact angle between particles and membrane. This case is basically equivalent to enforcing isotropic regions with intrinsic curvature, mimicking for instance the local perturbation of a protein, in a lipid bilayer for which isotropic aggregation is expected [81].

3.4 Free energy studies of linear aggregation

To understand why linear aggregates become more favorable for moderate bending rigidities, we placed three nanoparticles, A, B and C in linear formation and at a kissing distance over a planar membrane, and calculated the free energy cost required to disrupt the linear arrangement. The idea is to keep in place particles A and B and force particle C to form an angle φ_0 between the vector connecting particles A and B and that connecting particles B and C while keeping the relative particle distance unaltered. Using the umbrella sampling method, we can reconstruct piece-wise the probability that the trimer arranges according to any of the explored angles, which in turns gives us access to the free energy difference $\Delta F = F(\varphi) - F(\pi)$. All simulations were repeated for different values of D_0 and two different ranges of the binding potential. The results are shown in Fig. 3.3a, and undoubtedly tells us that in this region of the phase diagram the linear configuration is the most stable one, with the close-packed compatible configuration ($\varphi_0 = \pi/3$) sitting in a metastable shallow minimum of the free-energy curve separated from the linear configuration ($\varphi_0 = \pi$) by a significant barrier. The height of the barrier depends on the exact parameters, but is typically larger than $4k_{\mathrm{B}}T$ inside the linear region of the phase diagram. Fig. 3.3b shows the free-energy as a function of particle separation when the third particle approaches the other two from infinity, either in the linear or perpendicular alignment,

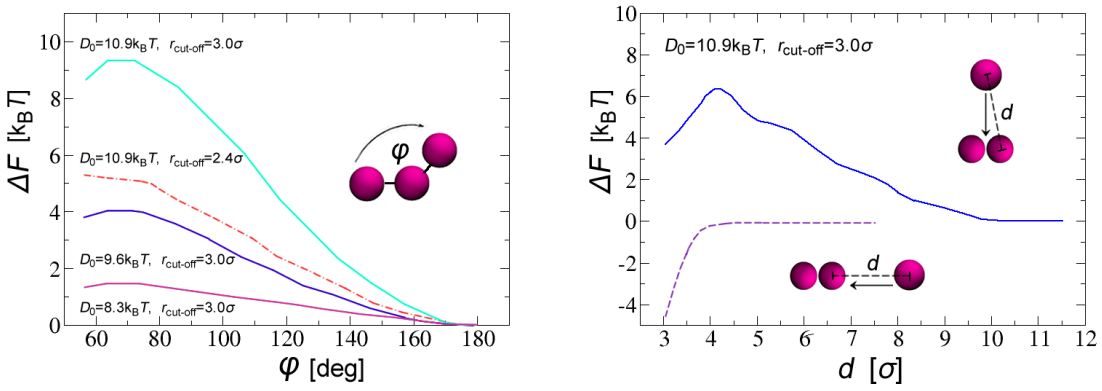

(a) (b)

Figure 3.3: (a) Angular free-energy profile for three nanoparticles bound to the membrane at different values of binding constant D_0 and interaction range $r_{\rm cut}$. (b) Free-energy as a function of the separation when a third particle approaches a fixed dimer along the direction of the dimer's axis (dashed line) and perpendicular to it (full line). In both cases we used $\kappa_b = 20 k_{\rm B}T$ and $\sigma_{np} = 3\sigma$.

as depicted in the insets in Fig. 3.3b. When the third particle approaches the dimer to form a linear aggregate, the free-energy (when particles are sufficiently close) decreases monotonically down to a minimum at contact. When the third particle approaches the dimer from a direction that is perpendicular to the dimer's axis, we observe a repulsive free energy barrier that precedes a shallow minimum at contact. Remarkably the range of the repulsion is felt as far as three nanoparticle diameters (up to 9 times the range of the attractive part), revealing correlations in the three body interactions that are significantly longer than the ones expect from a simple Casimir effect [73, 127].

To understand the unexpected stability of the linear aggregates over the close-packed structures in the regime where linear aggregation occurs, we measured the energy of the system associated with linear and hexagonal aggregates. The left panel of Fig. 3.4 shows explicitly how the total energy difference between linear and hexagonal aggregates, computed for the same values of γ, D_0 and k_b, as a function of

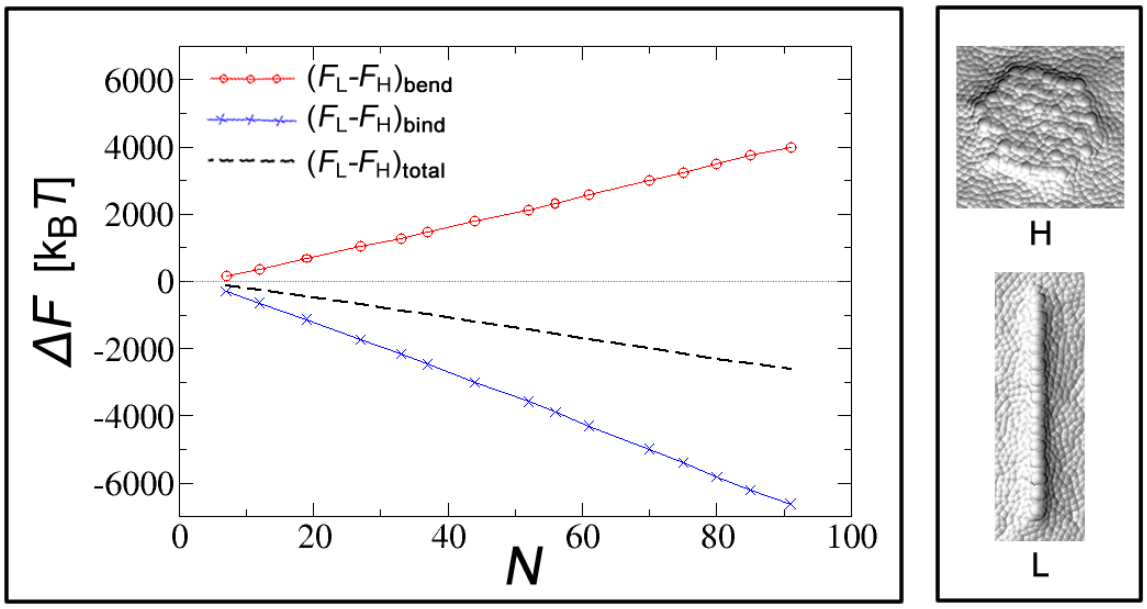

Figure 3.4: Left panel: Difference in bending, $(F_L - F_H)_{\rm bend}$, and binding, $(F_L - F_H)_{\rm bind}$, energies between linear and hexagonal aggregates as a function of particle number N at $\kappa_b = 20 k_{\rm B}T$, $D_0 = 10.9 k_{\rm B}T$ and $\sigma_{np} = 3\sigma$. The dashed line indicates the total energy difference between the two configurations. Right panel: typical membrane profiles underneath the aggregates in this regime.

particle number N, is partitioned between the bending $(F_L - F_H)_{\rm bend}$ and the binding $(F_L - F_H)_{\rm bind}$ contribution. This analysis reveals that despite the smaller bending cost, hexagonal aggregates provide a fairly small gain in binding energy when compared to linear aggregates, and this leads to a net energy balance that favors the latter. It is worth mentioning that we monitored the difference in free energy due to the surface tension between the two configurations, and found it to be indeed negligible. We also checked that linear aggregates form for our largest nanoparticles, $Z = 6$.

To rationalize these numerical data we offer the following scaling argument. A quick look at the typical surface deformations in this region of the phase diagram (see

snapshots in the right panel of Fig. 3.4) suggests that in either linear or hexagonal configuration the contribution to the system energy can be split in two parts. The first part comes from the overall deformation of the membrane due to the collective arrangement of the particles. The second part comes from the shallow surface indentations (corrugations) produced by each particle on top of the overall deformation. Let's assume that the energy due to the corrugation is fairly independent of the overall arrangement of the aggregates. We can think of it as a particle self energy e_0 that is constant for a given κ_B, γ and D_0. The total self-energy is than $E_0 = e_0 N$.

When particles arrange into linear structures (L), they generate a channel-like profile in the membrane with length proportional to the number of the nanoparticles N and width proportional to σ_{np}. The bending energy of the channel can be estimated using the standard elastic energy $\frac{\kappa_B}{2}(A/R^2)$ [36] with A being the area and $1/R$ being the constant curvature of the deformation. Ignoring the energy due to the contribution of the surface tension and subtracting the contribution of the particles' self energy, we can write the total free energy of the channel as $F_L - E_0 \approx 2\pi\alpha(\frac{\kappa_B}{2} - D_0\sigma_{np}^2)N$, where $0 < \alpha < 1$ is a parameter that accounts for the degree of surface wrapping per nanoparticle, and is related to the overall height of the channel. Close-packed hexagonal (H) arrangements form a flat, two-dimensional imprint of lateral size proportional to $\sqrt{N}$. In this case, apart from a geometrical prefactor, the free energy due to the rim of the imprint scales as $F_H - E_0 \approx \pi\alpha(\frac{\kappa_B}{2}(1+N^{-1}) - D_0\sigma_{np}^2)N^{\frac{1}{2}}$. In fact, here the area is proportional to the length of the rim and grows as $\sqrt{N}$, and the N^{-1} term accounts for the small bending cost associated with the in-plane curvature of the rim $k_B/2c^2A$ with $c \sim N^{-1/2}$. The key step is to notice that for any of these phases to be stable, the gain in binding needs to overcome the cost in bending, otherwise particles would not even bind to the membrane. Since the binding energy in the L phase grows much faster with N than that in the the H phase, the L phase becomes more stable as more and more particles are added to the surface. In other words, the gain in binding energy overwhelms the larger cost in bending.

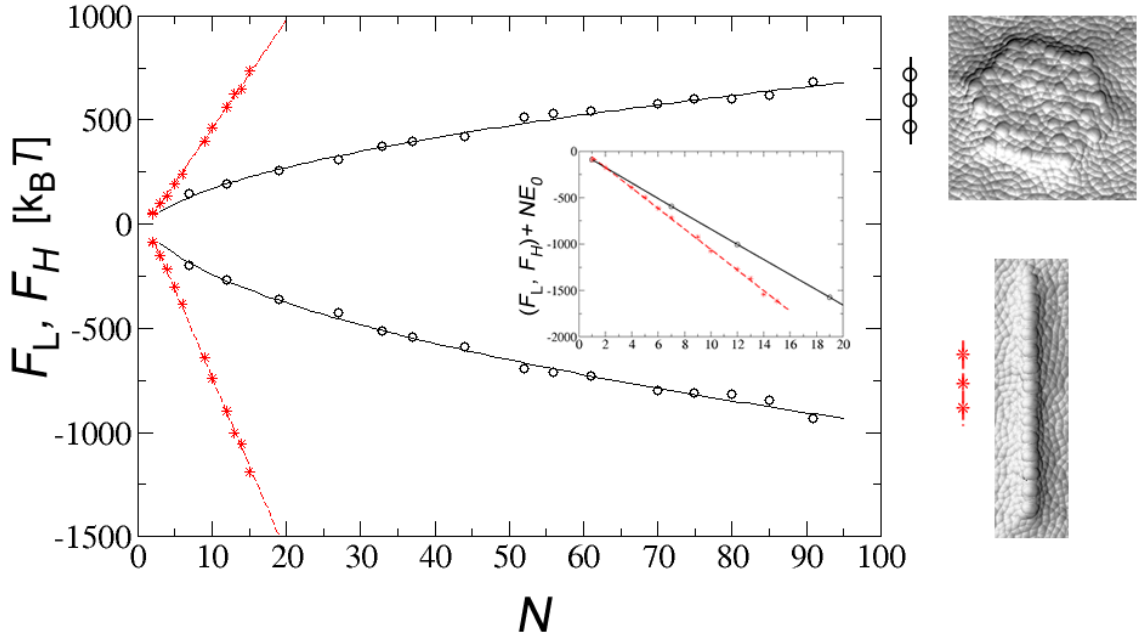

Figure 3.5: Bending (postive) and binding (negative) energy of linear (red stars and dashed lines) and hexagonal aggregates (black circles and solid lines) as a function of particle number N at $\kappa_b = 20k_{\mathrm{B}}T$, $D_0 = 10.9k_{\mathrm{B}}T$ and $\sigma_{np} = 3\sigma$. The self-energy E_0, estimated with a linear fit of bending and binding energies of the inner particles in hexagonal aggregates, has been subtracted from both curves. The inset shows the total energy of the two configurations, and the snapshots show the membrane profiles underneath the aggregates.

Fig. 3.5 shows separately the scaling of binding and bending energies once we subtract out the total particles' self-energy NE_0 and the average bending energy due to thermal fluctuations measured in particle-free simulations. This reveals that indeed our scaling hypothesis is correct, and for linear aggregates both bending and binding grow linearly with N, whereas isotropic structures result in a weaker $\sqrt{N}$ dependence on the number of particles. The inset in Fig. 3.5 shows the total energy (this time including NE_0) due to bending and binding for the two configurations as a function of the number of particles and shows that indeed the linear aggregates are more stable, and the difference between them increases with increasing N. The binding energy term, usually and correctly neglected for the case of membrane inclusions, is thus the essential ingredient for understanding the behavior of adsorbed particles.

3.5 Conclusion

In this Chapter we have computed a phase diagram showing the different aggregates formed by nanoparticles adsorbing onto a lipid bilayer as a function of the surface bending rigidity and nanoparticles adhesive energy. Our main result is that for a wide range of bending rigidities $\kappa_b \approx 10 - 100 k_{\mathrm{B}}T$, nanoparticles can organize into linear aggregates − provided the binding energy is sufficiently large.

Although linear aggregates can be expected to form on elastic (polymerized) surfaces due to the global constraints imposed on the surface deformations by the stretching rigidity K_s (at least in the large K_s limit) [123, 124], for fluid membranes $K_s = 0$. Our result is therefore quite different than the expected, and usually assumed, isotropic aggregation mediated by either local isotropic deformations of the surface or due to hydrophobic mismatch. The binding energy of the nanoparticles, the missing ingredient in studies of aggregation of membrane inclusions, is the key to rationalize this phenomenology.

Chapter 4

Membrane tubulation induced by adhesive nanoparticles

4.1 Introduction

The internalization of complex macromolecules is a key factor in cell trafficking and intercellular communication. As large and charged biological cargo cannot directly cross the lipid bilayer that envelops the different compartments within eukaryotic cells, this process is usually accompanied by the formation of vesicular- and tubular-shaped membrane protrusions. The mechanism by which they develop can be extremely diverse [80, 133–137]. It often involves active processes requiring accessory factors, such as clathrin or caveolin protein coats, or motor-proteins and external forces. It can also develop as a result of the self-assembly of anchoring proteins, such as BAR domain proteins [138, 139], that impose a local curvature on the lipid bilayer. The physical mechanism driving protein aggregation in this case is fairly well understood within the framework of effective bending mediated elastic forces[69]. The size and shape of the resulting deformation is determined by how the packing properties of the proteins couple to the elastic response of the membrane.

Several endocytic pathways, however, are found to be triggered by the cargo it-

self [133, 135, 140, 141]. In some cases, such as HIV-1 [142], the virus itself is formed on the membrane as its proteins self-assemble inducing their own vesicular bud. The internalization is thus a consequence of cooperativity of many protein molecules. In this Chapter we are interested in passive internalization of preassembled viruses, virus-like particles and other colloidal particles. The main difference from the cases discussed above is that the interaction of a single colloidal particle (typically one order of magnitude larger than a protein) with the lipid bilayer can induce its own invagination by wrapping its surface with the membrane. For instance, it has been shown that budding of preassembled alphaviruses and type-D retroviruses [135, 143], as well as charged colloids [144], can take place without the presence of external factors.

Although one might expect budding to be the main mechanism for internalization of large particles, long tubular protrusions typically of one-particle diameter are often observed in viral or nanoparticle internalization. Simian virus 40 (SV40), upon its binding to membrane receptors, is found to induce deep invagination and tubulation of both the plasma membrane and giant unilamellar vesicles (GUVs) [145]. Its entry occurs via small, tight-fitting indentations and the resulting invaginations have the same size as the virus-particle diameter. Positively charged nanoparticles were also shown to spontaneously induce tubulation in supported [146] and unsupported [144] giant unilamellar vesicles, suggesting the existence of a general physical mechanism of internalization, which is not exclusive for viruses and does not require assistance of membrane proteins.

Understanding this phenomenon is of great importance for developing anti-viral strategies, but also because viral and virus-like particles, as well as artificial nanoparticles, are promising tools in gene-therapy and molecular medicine, for which control over their cellular uptake is essential. Despite the large body of work [107, 147–153] on the particle budding problem, most studies have focused on the interaction of a single particle with the membrane, and have completely missed tube formation,

a crucial component of the phenomenological behavior associated to particle internalization, that can only arise as a result of nontrivial cooperative behavior among many particles. Here we use computer simulations to investigate the physical mechanisms behind the occurrence of this process, and show how it depends on particle size, concentration and binding strength. While the phenomenon has been observed in several experiments, to the best of our knowledge, this Chapter presents the first theoretical study that addresses nanoparticle-driven tubulation, and rationalizes its interplay with the particle budding process.

4.2 Literature review

In Chapter 3 we have considered only nanoparticles that impose relatively small deformations on the membrane surface. Significant local deformations can occur for sufficiently flexible membranes and large enough binding constants or nanoparticle diameters. Self-assembly in such conditions can lead to large global membrane deformations, and even to topological transitions. Now it is a good time to take a more detailed look at the binding of a single nanoparticle to the membrane. Let us consider a particle of radius $R_p \gg t$ adsorbed on a fluid membrane. The resulting membrane indentation can be approximated as a spherical cap of height h and area $S_{\rm cap} = 2\pi R_p h$, as illustrated in Fig. 4.1. According to Eq. 2.1, the cost in bending associated with this configuration is $\frac{2\kappa}{R_p^2} S_{\rm cap}$ and the cost due to surface tension is $\gamma\pi h^2$. In the latter expression πh^2 is the difference between the area of the spherical cap and its projected area, giving the increase in the membrane area due to particle binding. The free energy gain due to the adhesion energy between particle and membrane scales as $-D_0 S_{\rm cap}$, where D_0 is the binding constant per surface area. A balance of these terms leads to an equilibrium particle coverage $\chi \equiv S_{\rm cap}/(4\pi R_p^2) = \frac{D_0 - 2\kappa/R_p^2}{2\gamma}$. This suggests that, for small values of surface tension, a particle will become wrapped by the membrane as soon as $D_0 \gtrsim 2\kappa/R_p^2$. At that point the wrapped particle looses

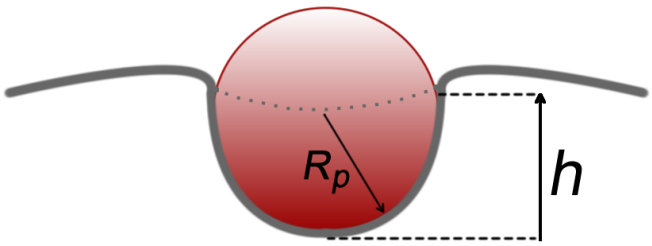

Figure 4.1: Nanoparticle of radius R_p wrapped by the membrane. h is the height of the corresponding spherical cap-like deformation induced on the membrane.

the contact with the membrane and buds off. The main point of this simple back-on-the envelope calculation is that for a given binding constant D_0, budding is easier for large particles.

A variety of more complicated calculations have been put forward to understand the nature of this transition [153–160]. In an early work on the subject [153], Döbereiner and Lipowsky have analyzed vesicles in contact with many colloids and they predicted individual budding of large particles. The authors completely neglected the contribution of the surface tension, in which case the simple analysis shows that the membrane coverage of a particle χ can be either 0 or 1, corresponding to unbound or fully wrapped particles, which clearly does not capture the complete picture since partial wrapping has been observed both in simulations and experiments. In a series of papers Deserno and co-workers have described the membrane profile underneath the bound nanoparticle and in its vicinity using full nonlinear shape equations [154, 155]. Their analysis reveals continuous nanoparticle binding with increase in D_0 followed by a discontinuous envelopment transition, pointing out to the presence of an energy barrier for the complete budding process. These results are in agreement with the particle-based simulations of the same process [150, 161–164], which in addition provide insight into molecular details of the transition and the different pathways it can take. Simulations have been extended to particles of different shapes [151, 152, 168, 169] and flexibility [170], and several statistical ther-

modynamic models have been developed [156–160] in search for optimal conditions for nanoparticle engulfment. Finally, a few experiments have been performed to understand the interaction of a single nanoparticle with a fluid membrane [165–167], with results in line with most of the theoretical findings. All these studies in the large deformation limit considered exclusively single-particle/membrane interactions. In what follows we review recent findings on binding of multiple particles showing that cooperative effects in such systems can lead to significantly different phenomena.

Reynwar et al. [140] have investigated aggregation of model virus caps and colloidal virus particles adsorbed on a coarse-grained membrane. They found that both the individual caps and the whole nanoparticles induce large, long range membrane deformations that span throughout the whole simulation box. Subsequently, the overlap of these large deformations drives nanoparticles together and induces membrane budding of several caps or particles without them being in direct contact. Although it is still unclear what is the origin of such large deformations, to the best of our knowledge this was the first explicit simulation study of the important process of collective endocytosis. Recently, the same authors have conducted continuum elasticity study of membrane-mediated interactions between circular particles in the strongly curved regime [72]. For large enough deformations they find a crossover from repulsive to attractive pair-interactions, in agreement with their particle-based simulations. Collective budding of many nanoparticles has also been discussed in simulations by Zhang et al. [129], in the small particle limit. In that case the budding is preceded by isotropic aggregation of nanoparticles into hexagonal structures and driven by increase in binding energy. Their snapshots show no large global deformations as the ones observed by Reynwar et al.

On the experimental side, Yu et al. have studied interaction of cationic nanoparticles enclosed inside spherical phospholipid GUVs [144]. In this experiments nanoparticles adsorbed onto the membrane surface and induced shape transformation in the form of tubular protrusions, that would break up into pearls over longer periods of

time. The tubules were almost uniform in size and approximately an order of magnitude larger than the size of a single nanoparticle. The nanoparticles did not appear to be embedded within lipid tails, but were mobile in the adsorbed state. The authors argue that the adsorption of a cationic nanoparticle increases the headgroup area of lipids causing a mismatch of surface area between the outer and inner leaflets. This would create a local curvature that could drive nanoparticle aggregation and shape change, but no qualitative explanation is available at this time. Similarly, Orwar et al. have investigated adsorption of $\sim 200nm$ CdSe/CdTe nanoparticles inside of surface-supported phospholipid vesicles connected to a multilamellar reservoir of lipids [146]. By tuning the concentration of salt they were able to control the spreading of the phospholipid on the supporting surface. When the vesicle did not preferentially adhere to the surface, they found that nanoparticles create tubular protrusions in the lipid bilayer which grow up to up to a length of several hundred microns and subsequently retract. They observe nanotubes of different fluorescent intensities, pointing out to a range of possible tube radii. In some occasions, tubes grew large in diameter and exhibited multicompartmentalization, which is beyond the scope of this discussion. Unlike Yu et al., this study did not report tubule pearling.

These results are quite exciting, since they point out to unexplored routes to nanoparticle internalization in biological and artificial membrane compartments [133]. To be able to use and control the process, a better understanding of the mechanism behind it is essential. It is well established that tubes can be generated out of lipid membranes by mechanical methods such as by action of motor proteins [171] or polymerization of cytoskeletal filaments [172] in cells, as well as by pulling by micropipette or optical tweezers in controlled experiments [173–176] and by exposure to hydrodynamic flows [177]. The size of the tubule in all of these cases is determined by the membrane's mechanical properties, and is given by $R_0 = \sqrt{\kappa/(2\gamma)}$ [178, 179]. Tubules can also be generated by curvature-inducing proteins [81, 133, 180–183], as well as by different chemical means such as by polymer or cholesterol insertion

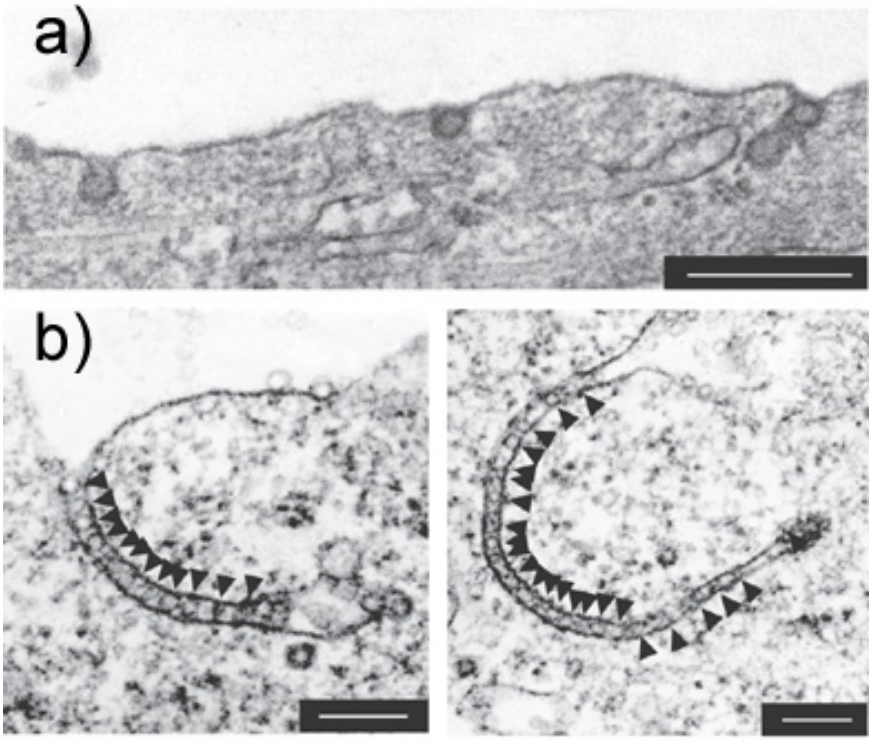

Figure 4.2: Tubular membrane invaginations induced by binding of SV40 virus particles. (a) Electron micrographs of cells that were incubated with SV40. Note the tight-fitting membrane under SV40 particles. (b) Electron micrographs of polyomavirus virus-like particle after incubation with cells. The virus-like particles line inside of tubular membrane invaginations like beads on a string (shown by arrowheads). Scale bars are 200 nm. Reprinted from Ref. [145].

[80, 181]. But until recently, tubulation induced by adhering nanoparticles has been missing from the large body of work published on nanoparticle-membrane interactions.

For large particles one usually expects budding to be the main mechanism of internalization by membranes. Nevertheless, long tubular protrusions have been observed in infectious pathways of preassembled virus particles. Ewers et al. have performed a thorough study of tubulation induced by simian virus 40 (SV40), both in plasma membranes and GUVs [145]. The authors conducted separate experi-

ments on tubulation driven by preassembled virus-like particles (VLP) of $45nm$ in diameter, as well as by individual $\sim 5nm$ capsomers. SV40 binds to the membrane via specific ligand-receptor interaction and the experiments show that association of both isolated capsomers and VLPs with membrane receptors was sufficient to induce formation of long tubular invaginations. However, the mechanism by which small membrane-curving capsomers induce tubulation is very different from that of pre-assembled particles. In both cases adhesion to the membrane creates local regions enriched in lipid receptors, causing line tension between receptor-enriched regions and the surrounding lipids. Decrease in line tension energy drives isotropic aggregation of capsomers enabling curvatures of individual proteins to build up cooperatively and deform the membrane, thus promoting tubulation via isotropic self-assembly. This picture is supported by the fact that tubulation in the case of capsomers is strongly tension-dependent and has a definite lag-time required for the aggregates to nucleate. On the other hand, binding of a single VLP causes sufficiently large local curvature by itself and tubulation happens almost instantaneously. Tubulation of VLPs shows no tension-dependence and fails to occur if not enough membrane receptors are engaged, pointing out to the dependence on binding. The VLPs aggregate into tight-fitting single-file nanotubes, where each VLP is in significant contact with the membrane (see Fig. 4.2). The authors suggest that VLP aggregation and membrane tubulation is driven by line tension or by means of curvature-mediated attractions, presumably similar to those proposed in simulations of Reynwar et al. However, these experiments suggest a scenario in which colloids are in direct contact with each other and well wrapped by the membrane, in contrast with the floppy invaginations in [140] which are low in nanoparticle density.

In this Chapter we discuss how this process can be explained by pure tendency of nanoparticles to increase their contact with the membrane, thus decreasing the binding energy and free energy of the whole system.

4.3 Simulation details

Our system setup consists of N_p particles, modeling colloidal viruses, virus-like particles or inorganic colloids, placed inside a vesicle of undeformed average radius R. Given the large size difference between the thickness of the vesicle and the nanoparticles considered in this study, we model the vesicle as an infinitely thin elastic surface consisting of N spherical beads of diameter σ connected by entropic flexible links of maximal extension $\sqrt{3}\sigma$ to form a triangulated network [101, 102, 104] whose connectivity is dynamically rearranged to simulate the fluidity of the membrane, as detailed in Chapter 2.3.

The membrane bending energy acts on neighboring triangles, and has the form given by Eq. 2.6, where κ_b is the bending rigidity. The cost associated with area changes is included via the energy term given by Eq. 2.7, where γ is the tension of the surface. The particles are represented as spheres of diameter $\sigma_p = Z\sigma$, where $Z > 1$ is a parameter used to control their size. Excluded volume between any two spheres in the system (particles and surface beads) is enforced with a hard-sphere potential. The colloid-to-membrane adhesion energy is modeled via an additional power-law interaction between the particles and the surface beads defined as in Eq. 3.1, with the cut-off set at $r_{\text{cut}} = 1.5\sigma_M$. D_0 is thus again the membrane-particle binding constant. This potential is quite generic and is typically employed to describe short-range attractions, such as ligand-receptor or van der Waals interactions. The system is equilibrated using the Monte Carlo simulations in the NVT ensemble where N is the total number of particles, V is the volume of the simulation box, and T is the temperature of the system. Most of our data are obtained at $\kappa_b = 5k_{\text{B}}T$, $\gamma = 1k_{\text{B}}T/\sigma^2$ (corresponding to surface tensions of the order of $10^{-2} - 10^{-3}$ pN/nm) and $Z = 2, 3, 4, 6$ or 8.

4.4 Tubulation *versus* budding

We begin our analysis by computing a diagram that indicates, for a given value of D_0 and R_p, the phenomenological behavior of the particle-membrane coupled system at a constant particle concentration. The results are shown in Fig. 4.3. For small values of D_0, the overall shape of the membrane is unchanged while the particles, barely adhering to it, freely diffuse over its surface as a low-density two-dimensional gas (**G**). Increasing D_0, we find that the nanoparticles organize into linear aggregates (**L**). This phase develops due to effective interactions between the particles driven by the membrane's need to minimize its elastic energy while maximizing its binding surface to the particles, as explained in Chapter 3. Upon further increase in D_0, spontaneous formation of tubular protrusions (**T**) takes place. This region of the diagram is characterized by nanoparticles tightly and linearly packed into tubular structures extruding out of the membrane core. The radius of the tubes equals the diameter of the particles. This behavior is in agreement with the SV40-induced membrane invaginations [145], where one-particle-wide tubes were also observed, but tubulation failed to occur if the adhering viruses were unable to form a sufficient number of interactions with the membrane binding sites. Further increase in D_0 causes nanoparticles to adhere to the membrane and become completely enveloped into a bud (**B**) before any significant particle diffusion can occur. The **T**-**B** transition is not abrupt, and a mixture of both "corrugated" tubes and single-particle buds is found in the borderline area between the two phases. Although in our model buds cannot physically detach from the membrane, they are easily identifiable by their complete surface-coverage and the characteristic sharp membrane neck shape. A single particle bud is shown in the inset of Fig. 4.3.

The most important message arising from our analysis is that tubulation develops as a result of the interaction of many particles and should be expected for intermediate binding constants. Such a behavior occurs for all particle sizes considered in this study and for all bending rigidities analyzed (up to $40k_{\mathrm{B}}T$), indicating that what sets

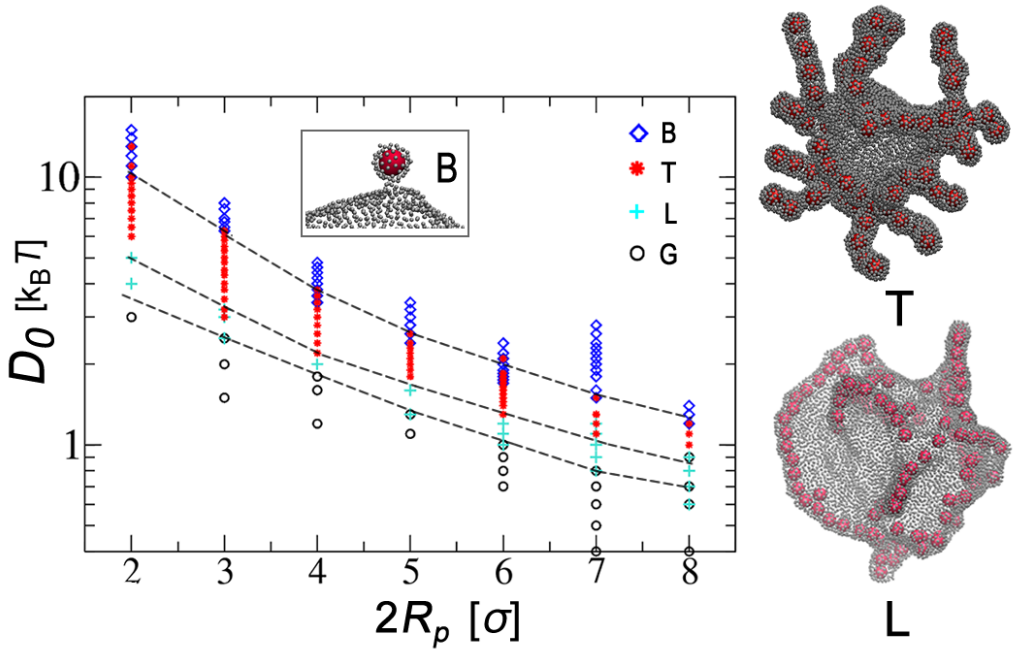

Figure 4.3: Left panel: D_0-R_p phase diagram of the membrane aggregates and protrusions induced by colloidal particles. Right panel: Snapshots of the linear (**L**) and tubular (**T**) phases. The inset shows a typical single-particle bud conformation (**B**) that occurs at large D_0. The bottom region of the phase diagram is the gaseous phase (**G**). The radius of the membrane is $R = 30\sigma$ and the particle surface fraction is kept constant at 0.15.

the tube size is the particle diameter and not the natural length-scale associated to membrane tube formation, $R_0 = \sqrt{\kappa_b/(2\gamma)}$, obtained by pulling experiments [179, 185]. Moreover, preassembly of nanoparticles into linear aggregates seems to greatly facilitate the formation of long tubes.

4.5 Free energy studies of tubulation

To obtain more physical insight into the mechanism by which tubular protrusions form, we considered a series of free energy calculations. First, we measure the effective interaction between two colloids adhering to the membrane in the **T**-region of the phase diagram. A standard implementation of the umbrella sampling method [119], using the distance d between the particles as an order parameter and a weak harmonic potential as a constraining bias, allows us to sample piecewise the probability that the two particles are at any given separation d from each other and estimate the free energy difference $\Delta F = F(d) - F(\infty)$. Fig. 4.4a shows ΔF as a function of d, while the inset monitors how the orientation of the dimer with respect to the membrane surface, φ, depends on the same variable. This result is quite revealing; the elastic cost required to bring together two large membrane deformations, responsible for the weak mid-range repulsion, is replaced by a large energy gain when the particles are in contact. The corresponding configuration is characterized by two particles contained within a membrane tube oriented perpendicularly to the membrane surface. As we have not imposed any constraint on the values of φ, this is clear evidence, at least at the two-particle level, that in this region of the phase diagram, tube formation is more favorable than budding.

Using the same procedure, we can also measure the free energy as a function of separation between a two-particle-tube and a third isolated particle. Our data, shown in Fig. 4.4b, tells us that the lowest free energy is again achieved when the three particles are in contact in a tubular formation. This very important result indicates

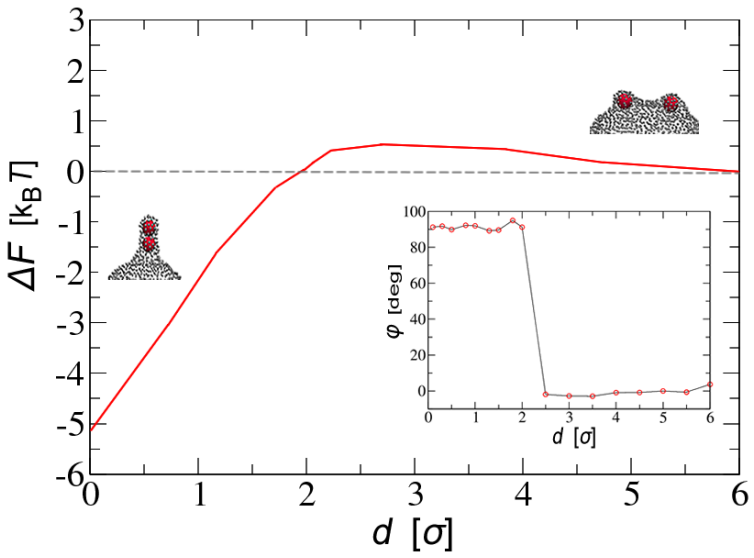

(a)

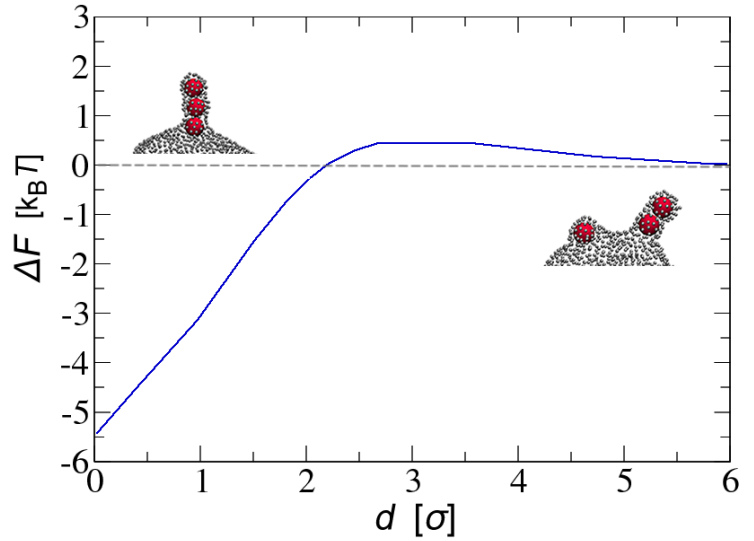

(b)

Figure 4.4: Tube formation and growth. **(a)** Free-energy as a function of separation of two membrane-bound particles. The inset shows the orientation of the dimer with respect to the membrane surface and indicates the distance at which the tubulation occurs. Here, φ is the angular excursion of the dimer's axis as it goes through the transition **(b)** Free-energy as a function of separation of a two-particle tube and a single membrane-bound particle. In both cases $Rp = 4$, $R = 15\sigma$ and $D_0 = 2.6k_{\mathrm{B}}T$.

that tubes and free particles bound to the membrane attract each other, and once a tube is formed, its growth by particle addition drives the system towards a lower free energy. In both cases, the extent of the repulsion and attraction is dependent on the specific region of the phase diagram they are computed at. The characteristic energy barrier at mid-range distance becomes more significant as D_0 increases and the system crosses over to the budding regime, implying that for large D_0 particle aggregation becomes rare, making budding the most likely barrier-crossing mechanism. This is a kinetically dominated regime: in fact, once the budding threshold has been overcome, particles would leave the membrane before having the time to aggregate.

4.6 Tubule nucleation

Interestingly, in most of our simulations in the **T** phase we observe that tube formation if often preceeded, in particular at higher particle densities, by the formation of long linear aggregates that eventually extrude from the membrane via a tilting mechanism illustrated in Fig. 4.5. This two-step process becomes more significant as we move closer to the **L-T** boundary, suggesting that these aggregates function as nucleation seeds promoting the transition. To support this idea we perform two sets of simulations: in the first set we start from a connected four-particle-long linear aggregate, and measure its surface coverage χ as a function of D_0 until a tube is formed, in the second set we start from an already tubulated structure and we decrease D_0 until the tubule retracts. As shown in Fig. 4.5, tubulation is accompanied by a sudden jump in the particle coverage χ (and consequentially in the binding energy), indicating the presence of a free energy barrier between the two states that needs to be crossed for the linear aggregates to protrude out of the membrane. This result is consistent with previous force-extension calculations and experiments on GUVs [179], that also indicated tube formation to be a first order transition.

Finally, we measured the onset value D_0^* at which a preformed linear aggregate

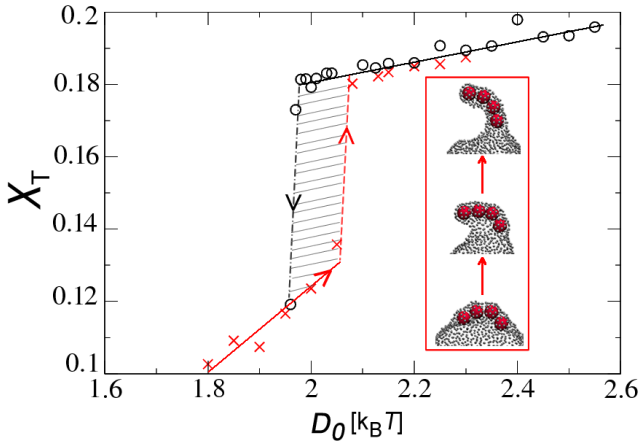

Figure 4.5: Hysteresis associated with the tubulation of a linear aggregate, in terms of the surface coverage χ and D_0, for the extrusion of a four-particle-long aggregate. χ is computed as the ratio between the number of membrane beads in contact with the particles and the same number when the surface completely envelops the particles. The red crosses show the results of simulations that start form a linear aggregate, while the black circles show simulations that start from a tube. Here $Rp = 4\sigma$ and $R = 15\sigma$.

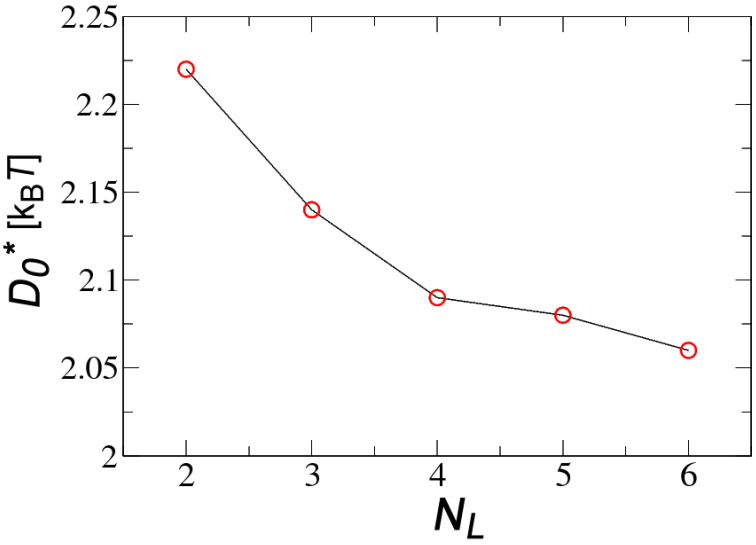

Figure 4.6: Onset binding constant for tubulation D_0^* as a function of the length of the preformed linear nucleation cluster; $Rp = 4\sigma$ and $R = 15\sigma$.

forms a tube as a function of its size, at a fixed particle radius. A weak but clearly inverse dependency is found, shown in Fig. 4.6, and supports the idea that the free energy cost for tubulation from the **L** phase does indeed decrease monotonically with the size of the aggregates which therefore act as nucleation seeds for the transition. It should be stressed that because the probability of forming linear aggregates increases with particle surface concentration, ρ, it is logical to expect tubulation to be more likely to occur in denser systems. This is indeed what we find in our study. We have not computed the phase diagram for different particle surface fractions, but we find that for $\sigma_p = 4$ the onset value of D_0 for tubulation decreases as the particle surface fraction is increased from 0.05 to 0.15 and 0.3. We expect tubulation to cease for sufficiently large nanoparticle-surface coverage as one approaches the colloidosome limit.

Working on almost identical system, Bahrami et al. [184] performed energy minimization of two and three particles adsorbed on the outer side of a vesicle. In

line with the results of our group, they found that the tubule which encapsulates colloids is indeed the energy minimum also in that case. The authors repeated two-particle simulations for several values of reduced volumes of the vesicle, mimicking conditions of different osmotic pressures obtainable in experiments. Based on the fact that stability of a two-particle tube varied with the reduced value of the vesicle, they suggest that changing osmotic pressure should be enough to reversibly control nanoparticle uptake.

4.7 Conclusion

We have shown that for a broad range of binding energies, tube formation and not membrane budding is the main mechanism leading to internalization of sufficiently large particles. Nowhere in our simulations have we observed formation of membrane tubes of radius larger than one particle diameter; however, these may develop as a result of direct particle-particle interactions or nontrivial long-range electrostatic effects [144] not included in our study. It should be emphasized that our results should hold as long as the particle size is sufficiently large so that the molecular details of the membrane can be ignored. Although the elastic constants of our model were selected in a range relevant to biological processes and we only considered two vesicle radii, we do not expect the process to be extremely sensitive to these parameters. Indeed, data with nanoparticle-membrane interaction range down to $0.1\sigma_M$, and surface tensions up to one order of magnitude larger show no qualitative difference in the tubulation process as long as membrane fluidity is preserved ($\gamma \lesssim 30 k_{\mathrm{B}}T/\sigma^2$ in our model when $\kappa_b = 5 k_{\mathrm{B}}T$).

Chapter 5

Self-assembly of nanoparticles on planar elastic surfaces

5.1 Introduction

Elastic surfaces are ubiquitous in nature and technology and appear across all length scales, from the cellular microenvironment to large-scale objects such as bridges and buildings. The mechanical properties of these surfaces play an important role both in their biological function, and in their wide usage in material engineering. For instance, it is known that the stiffness of an elastic substrate alters the morphology and dynamics of tissue cells adhering onto it [186]. Variable cytoskeleton assembly [187] and cell spreading [38] on substrates of different mechanical properties are two nice examples of this. Furthermore, their response to external stress have been exploited in metrology [46, 188] and in the production of micro- and nano-scale patterned surfaces that may serve as components with novel optical, electronic and magnetic properties [189].

In this Chapter we are interested in understanding how elastic surfaces could be used to template aggregation of nanocomponents. The idea to use elastic surfaces to design more complex nanoparticle patterns has come as a response to increasingly

large number of novel methods in producing elastic sheets and shells at the nano- and microscopic scale.

Elastic surfaces bend and stretch in response to deformations. The resulting macroscopic behavior is characterized by strong nonlinearities [36]. The mechanical properties of macroscopic elastic sheets have recently been the subject of intense investigation [46, 48, 59, 190–192]. Under an applied force an elastic surface deforms in a way that minimizes the energy associated with the deformation. As discussed in Chapter 2.1, it is easy to show [36, 59] that the ratio between stretching and bending energies for an arbitrary deformation of amplitude h on a flat elastic sheet of thickness t scales as $E_s/E_b \sim (h/t)^2$. Therefore, for sufficiently thin sheets, bending is the preferred mode of deformation and unstretchability can be thought of as an overall geometrical constraint to the deformations. The net result is that thin elastic surfaces respond to an external applied stress with stretch-free deformation involving (when possible) exclusively uniaxial bending. Such nontrivial phenomenology extends to the micro-scale. There are several artificial and naturally occurring examples of microscopic elastic surfaces, including graphite-oxide sheets [44, 45], graphene sheets [42, 43], cross polymerized biological membranes [37], cross polymerized hydrogels [38], buckypaper [193–195], the spectrin-actin network forming the cytoskeleton of Red Blood Cells [39, 40], and very recently they have been fabricated using close-packed nanoparticle arrays [41]. Our expectation is that diffusible particles adhering over an elastic surface should be driven to aggregate into configurations that reduce the mechanical cost of the overall surface deformation. These configurations will depend on the geometry of the surface, its elastic properties and the strength of the adhesion (the applied force).

In this Chapter we explore the phase behavior of nanoparticles adhering onto a planar (extended) elastic substrate as a function of the mechanical properties of the substrate, namely its stretching and bending rigidity, and the strength of the adhesion. We also analyze the role of the boundaries of the elastic sheet and their

influence on the aggregation patterns. Our findings suggest that the geometrical features of the anisotropic aggregation of the particles can be tuned in a variety of patterns by controlling the elastic parameters of the problem.

5.2 Simulation details

The elastic plane is modeled via a standard triangulated mesh with hexagonal symmetry [101]. To impose surface self-avoidance we place hard beads at each node of the mesh. Any two surface beads interact via a repulsive truncated-shifted Lennard-Jones potential:

$$U_{LJ} = \begin{cases} 4\epsilon \left[\left(\frac{\sigma}{r}\right)^{12} - \left(\frac{\sigma}{r}\right)^{6} + \frac{1}{4} \right] & , r \leq 2^{1/6}\sigma \\ 0 & , r > 2^{1/6}\sigma \end{cases} \tag{5.1}$$

where r is the distance between the centers of two beads, σ is their diameter, and $\epsilon = 100 k_{\mathrm{B}} T$.

We enforce the surface fixed connectivity by linking every bead on the surface to its first neighbors via a harmonic spring potential

$$U_{stretching} = K_s (r - r_B)^2. \tag{5.2}$$

Here K_s is the spring constant and it models the stretching rigidity of the surface. r is the distance between two neighboring beads, $r_B = 1.23\sigma$ is the equilibrium bond length, and it is sufficiently short to prevent overlap between any two triangles on the surface even for moderate values of K_s.

The bending rigidity of the elastic surface is modeled by a dihedral potential between adjacent triangles on the mesh:

$$U_{bending} = K_b (1 + \cos\phi) \tag{5.3}$$

where ϕ is the dihedral angle between opposite vertices of any two triangles sharing an edge and K_b is the bending constant.

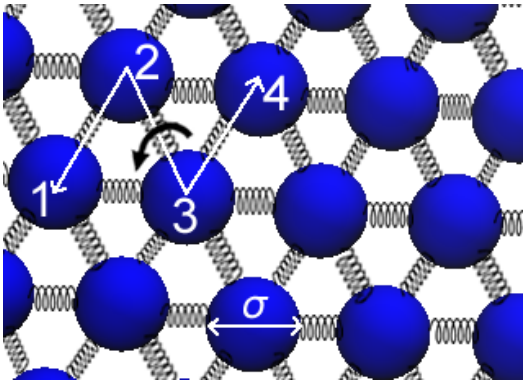

Figure 5.1: Illustration of the triangulated mesh model used in our simulations. The surface beads of diameter σ (blue spheres) are set at the nodes of each triangular element to enforce surface-self-avoidance and are linked to their first neighbors with springs of the constant K_s and the equilibrium length r_{NB} (measured form the beads centres). The surface connectivity is kept constant, and apart from boundary nodes each surface bead has six neighbors. The dihedral angle 1-2-3-4 from which bending energies are computed is also indicated. This energy is minimized when all angles between neighboring triangles are equal to ϕ.

Particles of diameter $\sigma_c = 10\sigma$ are described via the repulsive truncated-shifted Lennard-Jones potential introduced in Eq. 5.1 with $\sigma \to \sigma_c$. The generic binding between the nanoparticles and surface is described by a Morse potential:

$$U_{Morse} = \begin{cases} D_0 \left(e^{-2\alpha(r-r_{NB})} - 2e^{-\alpha(r-r_{NB})} \right) & , r \leq 10\sigma \\ 0 & , r > 10\sigma \end{cases} \tag{5.4}$$

where r is the center-to-center distance between a nanoparticle and a surface-bead, r_{NB} is bead-nanoparticle contact distance $r_{NB} = 5.5\sigma$ and D_0 is the binding energy. The interaction cutoff is set to 10σ and $\gamma = 1.25/\sigma$.

The simulations were carried out using the LAMMPS molecular dynamics package [196] with a Langevin dynamics in the NVT ensemble. Dimensionless MD units are used throughout this Chapter. The timestep size was set to $dt = 0.002\tau_0$ (τ_0 is

the dimensionless time) and each simulation was run for a minimum of $5 \cdot 10^6$ iterations. In this study we considered unconstrained and edge-constrained sheets. To minimize edge effects in unconstrained sheets we considered surfaces with an overall circular geometry. Two different equilibrium radii $R_{plane} \simeq 50\sigma$ and $R_{plane} \simeq 60.4\sigma$ were explored. To preserve the mechanical stability of the sheet the colloids were placed both on top and at bottom of the surface. When edge-constrained surfaces were considered, a rectangular shape was selected and the colloids were placed only on one side of the plane. For this specific case we considered two surface equilibrium areas, $A \simeq (176 \times 152)\sigma^2$ and $A \simeq (244 \times 212)\sigma^2$. In both cases a wide range of nanoparticle surface fractions between 10% and 60% was explored. Typical values of $\sigma \sim 10-20nm$ would imply colloidal particles of diameter $\sim$ 100-200 nm and surfaces of area $A \sim 200 - 1000\mu\text{m}^2$. Figure 5.1 illustrates the model used in our simulations.

5.3 Free-standing elastic sheet

We find that elastic surfaces can indeed drive nanoparticle aggregation. The geometry of the aggregates can be tuned into a variety of patterns controlled by the mechanical properties of the surface (K_s and K_b) and the strength of the particle's adhesion (D_0). Let us begin by looking at the role of the membrane's stretching rigidity. Fig. 5.1a) shows a diagram of the different aggregates obtained for different values of K_s as a function of the extent of the surface deformation (regulated by D_0) at fixed bending rigidity K_b. Fig. 5.1c) shows simulation snapshots of the corresponding patterns. As expected, when D_0 is small the surface is basically unaffected by the presence of the particles and the particles behave effectively as a low-density two-dimensional hard sphere fluid. In the opposite limit, when the particles bind very strongly, the membrane undergoes large local deformations limiting the diffusion of the particles and resulting in kinetically trapped configurations. Repeating the simulations under the same conditions leads to a different not well defined configuration. We call this

phase the arrested phase.

The intermediate regime is characterized by five distinct structured phases. For small values of K_s the aggregation is completely driven by the minimization of the bending energy. As a result particles aggregate into a two-dimensional hexagonal crystal. Upon a small increase in K_s the hexagonal crystal rearranges into a square lattice.

For even larger values of K_s the connected network is disrupted and particles arrange into straight parallel lines. Increasing K_s at this points only leads to to a larger stiffness of the linear aggregates. This transition is completely stretching-driven. The parallel lines start appearing when $K_s \gtrsim K_b$. This is clearly shown in Fig. 5.1b) where we show how the formation of straight and connected aggregates depend on both stretching and bending constants. For $K_s/K_b \gg 1$ one indeed recovers the thin and unstreachable sheet limit for which only stretch-free (uniaxial) deformations are possible. It is important to stress that the formation of parallel lines, that effectively creates a uniform undulating and one-particle-think corrugation on the surface, is driven by the binding energy. In fact, a stretch free deformation could also be obtained by forming several particles-thick linear aggregates, but these configurations would have a weaker binding to the surface. The most dramatic consequence of this property of elastic plates is the fifth, folded phase. This phase occurs for larger values of D_0, when particles tend to increase the contact area with the membrane as much as possible. In this region the surface immediately folds into a well organized higher three-dimensional hexagonal structure (Fig. 5.1c)).

To better characterize the dependence of the different phases on K_s - from the hexagonal to the square lattice, from the connected network to the linear one, we also measured the frequency of particle contacts as a function of K_s. Fig. 5.2 shows the probability distribution of the number of the nearest neighbors as a function of K_s in the different phases. The connectivity decreases when increasing K_s, going from the six neighbors of the hexagonal phase to the four neighbors in the square lattice,

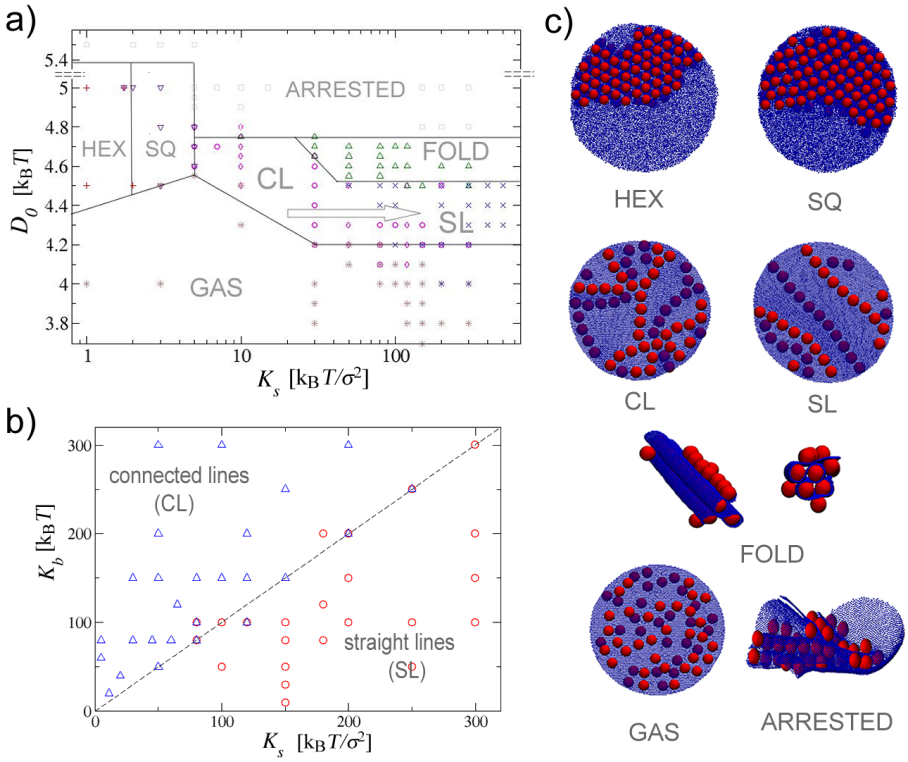

Figure 5.2: (a) Phase diagram of nanoparticles binding to an elastic planar surface. In this case the bending rigidity is $K_b = 150k_BT$; the equilibrium radius of the surface is $R \simeq 60.4\sigma$ and the number of nanoparticles is $N = 40$. The lines separating the different phases serve as a guide to the eye. The arrow points in the direction of lower line connectivity. (b) Boundary between connected to straight parallel lines as a function of K_s and K_b. The dashed $K_b = K_s$ line serves as a guide to the eye. (c) Simulation snapshots of the seven observed phases. For the sake of clarity the hexagonal and the square crystal phases are shown with the larger number of particles than the other phases.

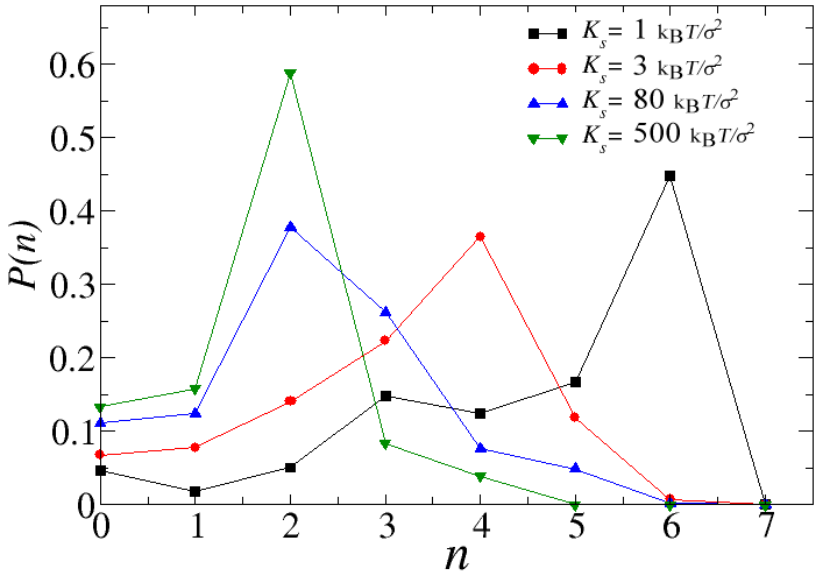

Figure 5.3: Probability distributions of particle contacts in self-assembled aggregates for different values of K_s, and constant $K_b = 150k_BT$. From right to left the distributions refer to the planar hexagonal crystal, the planar square crystal, the interconnected lines, and the straight parallel lines.

and finally two for the connected and the straight lines. For the linear aggregates the significant difference is not in the location of the peak of the distribution (indeed a large number of particles will have two neighbors even in the connected linear aggregates), but in the relative height of $P(3)$ which is the signature for branching.

It should be emphasized that the number of connections does decrease continuously with increasing K_s. It is tempting to interpret these data in terms of a single growing length scale that sets the size for the average distance between any two nodes in the linear network, and consider the straight-line phase as the limiting behavior in which this distance becomes larger than the surface. A simple mean field calculation balancing stretching and bending energies [59] points to the length scale

$l_p \propto h^{1/2}(K_s/K_b)^{1/4}R^{1/2}$ (discussed in details in Chapter 6), which qualitatively produces the correct phenomenological behavior, but unfortunately the small system sizes analyzed in this study prevent us from making such a link more concrete.

5.4 Clamped elastic sheet

It is important to stress that the free boundaries of the membrane play an important role. Indeed, it is not clear whether the linear phases indicated in Fig. 5.1 are stable with respect to folding. In fact, in a few cases our longest simulations of the linear phases resulted eventually in a folded phase. We expect this to be an effect of the free boundary of the surface that can be taken care of by applying a small external tension or by clamping the outer edge of the surface. To show that this is indeed the case, we considered a rectangular elastic sheet in which two opposite sides (edges) are kept fixed (clamped). In the absence of the adhering particles the sheet remains flat to its equilibrium size. Once the particles bind to it we observe only two phases for moderate values of K_s, the gas phase and the straight-linear phase. The former appears when D_0 is insufficient for the particles to deform the membrane, while the latter occurs when D_0 crosses a certain threshold value which depends mainly on the bending rigidity of the plane (Fig. 5.3a)).

The linear structures formed in this phase always appear to be perpendicular to the constrained sides of the membrane (Fig. 5.3b)). However we observe that the distance between them can be tuned by changing K_s and K_b. This kind of pattern is reminiscent of the wrinkle pattern that occurs when a thin elastic sheet is subjected to a longitudinal stretching strain[191, 192]. The sheet is then unable to contract laterally near the clamped boundaries, so it wrinkles to accommodate the in plane stress. Cerda and Mahadevan showed that, for a constant tension, the wavelength of the wrinkles scales as $\lambda \sim (L)^{1/2} \sim (K_b/K_s)^{1/4}$ [192].

Indeed, we find the same reasoning can be applied here. Instead of having an external

force stretching the plane, the particles binding to the surface act as the stress source causing the sheet to wrinkle. This stress is directed perpendicularly to the fixed sides of the plane. Since the wrinkles are the regions where the particles can gain the highest contact area with the surface, i.e the highest binding, the particles follow the wrinkle pattern resulting in the straight parallel aggregates. We believe that the destabilization of the linear-connected phase is due to the implicit symmetry breaking imposed by the way we clamp the membrane, in fact, when clamping is enforced on all four edges of the sheet, the phase reappears.

We also analyzed the dependence of the wavelength of the particles' lines with K_b and K_s and it appears to nicely follow the theoretical prediction of Cerda and Mahadevan (Fig. 5.3b)). Nevertheless, two extra parameters play a role in determining the separation between the lines in this case: the surface coverage and the particles's binding energy. Since particle binding to the surface is favorable, once the particle's density becomes larger than that required to completely fill the wrinkles with particles, new lines (wrinkles) form in between the preexisting ones, bringing the preexisting ones closer together. The inset in Fig. 5.3b) shows the decrease in λ with the increase in the particle density, for two different values of K_s. In addition to that, we find that the increase in D_0 (for constant K_s and K_b) also brings the lines closer together. Higher binding increases the amplitude of the wrinkles (analogous to increasing the strain tension in [191]), which decreases the surface area accessible to the particles, effectively increasing the density.

It should be stressed that the mechanism driving self-assembly of particles into linear aggregates that we described is significantly different from the controlled wrinkling methods recently developed for the fabrication of patterned surfaces[189]. There the wrinkles are preformed by compressing the substrate, and particles trivially arrange along the wrinkles' axis to maximize their binding energy, in our case the surface is not pre-wrinkled, and the linear aggregates develop (in a reversible manner) as a result of a more delicate balance between the energies of the system and the collective

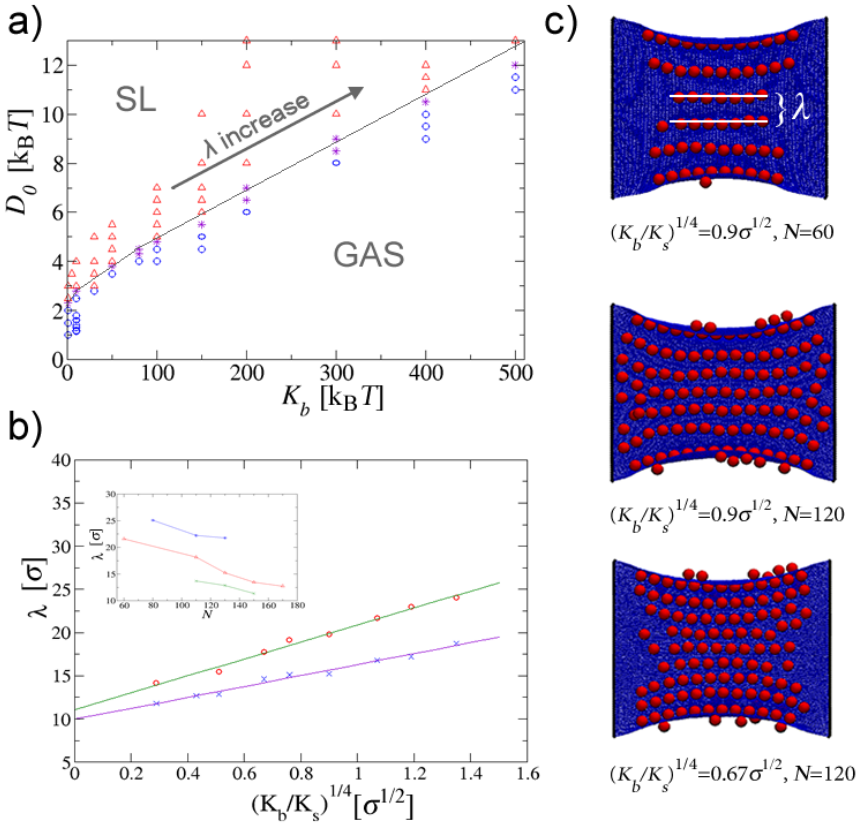

Figure 5.4: (a) Phase diagram of nanoparticles binding to a clamped rectangular elastic surface. Two phases are observed for different values of K_b and depend only on D_0: the gas phase and straight parallel lines phase (SL). These data refer to the case in which $K_s = 150 k_B T/\sigma^2$, $N = 60$, and the area of the the plane is $(176 \times 152)\sigma^2$. (b) Line separation λ as a function of the mechanical properties of the surface. We show data for two different surface coverages: $\phi = 38.7\%$ (cross symbols) and $\phi = 21.2\%$ (circle symbols). The straight lines represent the fit of the data to the scaling law $\lambda \sim (K_b/K_s)^{1/4}$. The inset shows the dependence of λ on the particle surface coverage, shown for three different values of the $(K_b/K_s)^{1/4}$ parameter: $1.35\sigma^{1/2}$(top), $0.9\sigma^{1/2}$ (middle), $0.51\sigma^{1/2}$ (bottom). (c) Simulation snapshots of linear aggregates for three different combinations of the elastic parameters and the surface coverage densities. The equilibrium surface area is $A = (176 \times 152)\sigma^2$.

behavior of the particles. Interestingly, once the wrinkled phase is formed it is possible to control the overall direction of the lines by simply applying a small external tension. For instance, the release of the surface clamping and simultaneous application of a small tension in the direction perpendicular to the direction of the wrinkles, results in a reorientation of the lines along the direction of the tension. This supports our assumption of the reversibility of the line-forming process and could suggests even richer potential application of this approach for periodical patterning.

5.5 Conclusion

In this Chapter we shown how elastic surfaces can template self-assembly of nanoparticles, similarly to the way fluid interfaces do. We show how by tuning the relative cost of bending and stretching energies (i.e. the thickness of the sheet) it is possible to control the geometry of the aggregates. The formation of the different linear aggregates, for thin sheets, is an explicit manifestation of the anisotropic interaction between the nanoparticles. When the surfaces become effectively unstreachable particles arrange into macroscopic ordered parallel lines whose separation can be controlled by the elastic parameters of the surface. Clamping of the edges across the membrane substantially improves the periodic ordering in the system.

The physical properties of our model can be mapped onto a model of a thin sheet supported on an elastic foundation if the stretching rigidity of the plane is substituted by the stiffness of the elastic foundation. Therefore, the results of our theoretical study are quite general and may suggest novel use of the elastic interfaces in nano/micromechanics and material engineering. Possible experimental systems where our predictions could be tested include cross-polymerized or crystalline lipid bilayers, thin polymeric sheets, ultrathin cross-linked nanoparticle-membranes or possibly free standing liquid crystalline films in the presence of colloidal particles. More in general,

any elastic substrate that can be locally deformed by the interaction with a diffusable binding component.

Chapter 6

Effective elasticity of a flexible filament bound to a deformable elastic tube

6.1 Introduction

A ubiquitous geometrical state filaments arrange into is the helix. Apart from some synthetic polymers [197] and biological filaments such as ds-DNA and actin filaments which spontaneously develop a helical conformation due to their inherent chemical structure [2], helicity can also appear when a filament is bound to a cylindrical surface. This phenomenon can be observed across all length scales: from vine wrapped around trees, to DNA on carbon nanotubes [198].

Although in several instances it is believed that what leads to the helicity of a filament is either a specific property of the filament or the specific interactions between the filament and the underlying surface [199–201], there is evidence that semiflexible polymers binding non-specifically to cylindrical surfaces can spontaneously develop helical conformations. The arrangement of cellulose microfibrils in the plant cell wall [202] is a nice example of it. Recently it has been suggested that the helix is the

preferred conformation of semiflexible polymers when generically bound to the surface of an infinitely long cylinder, provided the cylinder's radius is sufficiently large [203].

One particular aspect of the problem that has not been studied and could be of great relevance, concerns the role of the deformability of the underlying cylindrical surface. This property is inherent to biological materials, and the dynamical interplay between protein filaments and the soft cell membrane has been shown to be crucial in several biological processes [2]. In fact, semiflexible biopolymers such as microtubules and actin filaments not only provide the cell with a highly dynamical scaffolding that regulates its shape, but they also mediate important extracellular interactions. Cell division [204] and cell crawling [205] are two dramatic examples of it.

In this Chapter, we explicitly consider the role of the surface deformability and geometry, and predict that new phenomelogical behavior arises when a filament is bound to it. Because of the surface's curvature, the situation is a bit more complex than in the case of the elastic plane discussed in Chapter 5 [124, 209]. As long as the surface-rigidity allows the particles to indent the membrane, they will arrange in linear aggregates that optimize the binding energy, analogous to the cases of a fluid membrane and elastic plane. However, the spatial orientation of the lines will change depending on the ratio of the bending to the stretching rigidity. Unlike flat sheets, elastic nanotubes have a unique and very well defined way of deforming at zero stretching cost: the deformation must be parallel to its axis and must persevere uniformly along the whole cylinder.

Using simple scaling arguments it is possible to estimate the extent of the deformation, l_p, that arises when an indentation of amplitude h is imposed on a narrow elastic sheet of width D, as shown in Fig. 6.1a). Following Ref. [59], the bending and stretching energies associated with this deformation scale as $E_b \sim K_b \left(h/D^2\right)^2 D l_p$ and $E_s \sim K_s \left(h^2/l_p^2\right)^2 D l_p$, where K_b and K_s are the bending and stretching constants respectively. The balance between the two terms gives $l_p \sim D h^{\frac{1}{2}} \left(K_s/K_b\right)^{\frac{1}{4}}$. A more familiar form of this expression is obtained by plugging $K_s \sim \mathrm{Y}t$ and $K_b \sim \mathrm{Y}t^3$ [36]

(Y is the Young modulus of the surface) to give $l_p \sim D(h/t)^{\frac{1}{2}}$.

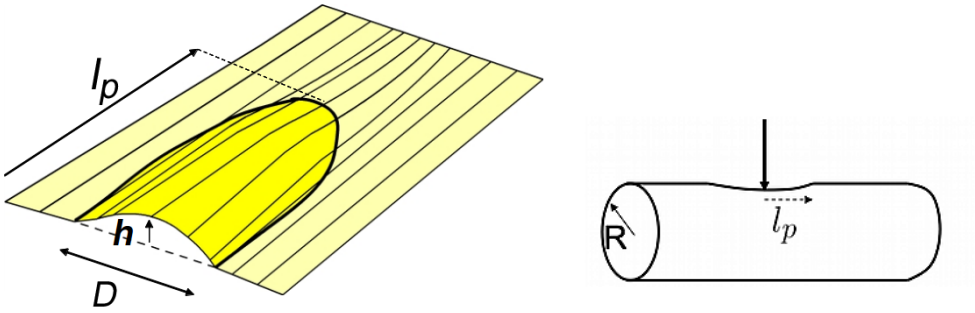

(a) (b)

Figure 6.1: (a) Sketch of the extent of the deformation, l_p, after an indentation of height h is imposed on a planar elastic sheet of a width D. (b) Analogous extent of the deformation along the axis of a cylinder.

This result can be generalized to a cylindrical surface of radius R (with $D \sim R$) as long as $h \ll R$ (see Fig. 6.1b)), and saturates to $l_p \sim R(R/t)^{\frac{1}{2}}$ for thin cylinders and/or large deformations [206, 207]. Either way, for a fixed cylindrical radius R and indentation h, the extent of the deformation along the axis of the cylinder is set by the ratio between bending and stretching constants.

In this Chapter we show how a fully flexible filament that generically binds to a deformable cylindrical surface can acquire a macroscopic bending rigidity and a specific intrinsic curvature set by the mechanical properties of the surface and the extent of the deformation. The net result is an effective semi-flexible chain that wraps around the cylinder with a tunable pitch. Using a combination of scaling arguments and numerical simulations we show how the characteristic length scale l_p is directly related to the pitch of the helix, and we present a phase diagram showing the transition from a disordered (random walk) to the helical conformation of the filament as a function of its binding affinity to the surface. The physical reasons behind it are quite general, are applicable to arbitrary geometries, and can be understood by analyzing the nontrivial mechanical response of elastic sheets to local deformations.

6.2 Simulation details

We model the elastic surface via a standard triangulated mesh [101]. The mesh is composed of $N = 14960$ nodes arranged to produce an initial configuration with perfect hexagonal tessellation. To impose surface self-avoidance we place hard beads of diameter σ in each node of the mesh. Any two surface beads interact via a purely repulsive truncated and shifted Lennard-Jones potential given in Eq. 5.1.

We enforce the surface's fixed connectivity by linking every bead on the surface to its first neighbors via a harmonic spring whose constant is K_s (Eq. 5.2). The bending rigidity of the elastic surface is modeled by a dihedral potential between adjacent triangles on the mesh (Eq. 5.3), with the bending constant K_b.

The polymer is constructed as a "pearl necklace" with $N_m = 20$ monomers of diameter of $\sigma_m = 10\sigma$. Neighboring monomers are connected by harmonic springs as in Eq. 5.2 with an equilibrium bond length $r_M = 1.18\sigma_m$ and spring constant of $120k_{\mathrm{B}}T/\sigma^2$. Polymer self-avoidance is again enforced via the repulsive truncated-shifted Lennard-jones potential introduced in Eq. 5.1 with $\sigma \to \sigma_m$. Note that we do not associate an explicit bending rigidity to the polymer which behaves as a simple self-avoiding random walk when bound to an infinitely rigid cylinder.

The generic binding between polymer and surface is described by a Morse potential with its associated binding constant D_0, as in Eq. 5.4.

We used the LAMMPS molecular dynamics package [196] with a Nosé/Hoover thermostat in the NVT ensemble to study the statistical behavior of the system. Periodic boundary conditions are imposed to make the cylinder effectively infinite. No difference was found when using the NP_zT ensemble, with $P_z = 0$ (z is aligned along the cylinder's axis). The timestep size was set to $dt = 0.002\tau_0$ (τ_0 is the dimensionless time) and each simulation was run for a minimum of $5 \cdot 10^6$ steps. The radius of the undeformed cylinder was set to $R = 14\sigma$ in all our simulations.

6.3 Polymer phases

The overall strategy of our numerical work is to perform a statistical analysis of the system for different values of K_s and D_0, and to understand how the configurational properties of the binding polymer are related to the elastic properties of the templating surface.

Fig. 6.2 shows for a particular value of the membrane bending rigidity the different phases of the polymer in terms of the binding constant D_0, which regulates the extent of the surface indentation h, and the stretching constant K_s. We find a gas phase, an arrested phase and a helical phase.

The behavior of the system in the limit of very large and very small indentations is clear. In the first case, the cylinder is effectively rigid and does not alter the behavior of the polymer which performs a self-avoiding random walk over its surface. We indicate this phases as the gas phase. In the second case, the polymer acquires non-helical conformations that differ from each other once simulations are repeated (under the same conditions) using a different initial configuration. This is indicative that the polymer becomes kinetically trapped and we take this as a signature that the system dynamics is becoming glassy. We call this phase the arrested phase. The most interesting behavior arises for moderate indentations, where the interplay between bending and stretching energies of the surface strongly affects the configurations of the polymer, and results in an interesting helical phase with pitch increasing monotonically with the membrane stretching cost.

6.4 Analysis of the polymer helicity

Local deformations caused by each monomer in the helical phase pair-up coherently to generate a smooth surface channel following the chain profile. Scaling arguments can be used to estimate the energy cost required to form a channel along the cylinder axis and one around it. The total bending energy associate with the axial configuration

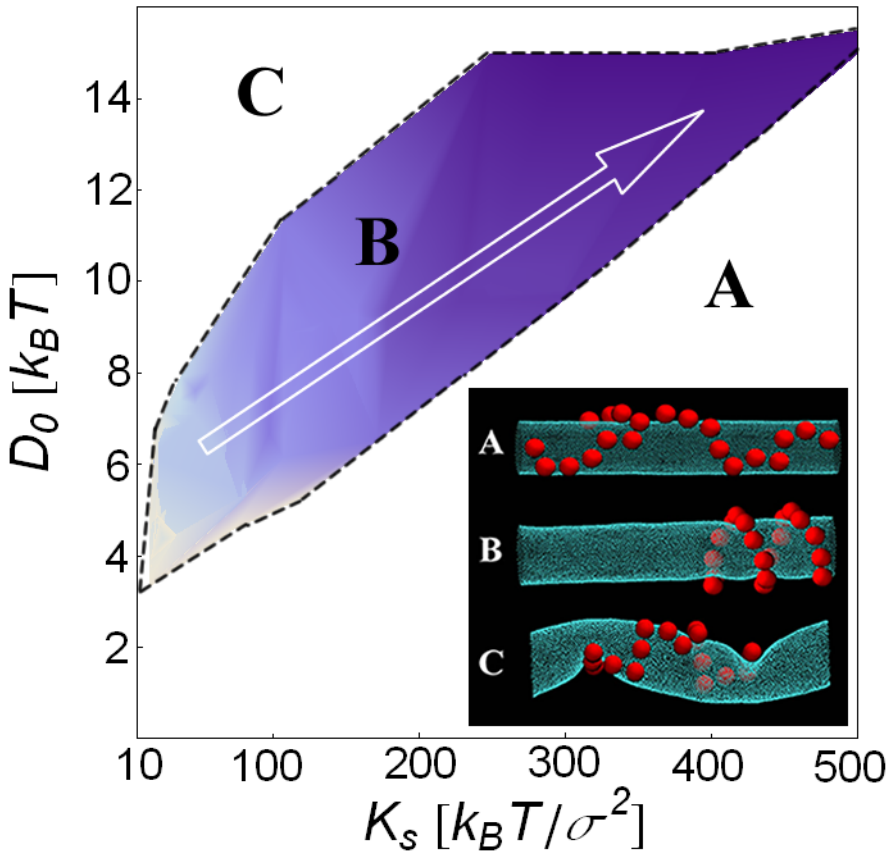

Figure 6.2: Phase diagram of a fully flexible polymer binding to an elastic tubular surface for fixed $K_b = 150k_BT$. Three phases are shown as a function of D_0 and K_s - A: gas, B: helix, C: arrested phase. The direction of the white arrow and the shading in the B phase show the helical pitch increase with K_s. Dark regions indicate large pitch, whereas light regions represent low pitch. The inset shows three snapshots of the chain configurations in the three phases.

scales as $E_b^{\parallel} \sim K_b \left(h/R^2\right)^2 lR$, while that for the transversal configuration has a bending cost $E_b^{\perp} \sim K_b \left(h/l_p^2\right)^2 ll_p$, where $l \sim \sigma_m N_m$ is the contour length of the polymer.

As l_p is typically larger than R, $l_p \sim R\sqrt{h/t}$, the bending energy balance favors configurations in which the polymer wraps around the cylinder to produce ring-like configurations. However, the stretching energy becomes negligible when the polymer

is placed along the cylinder's axis, and grows as $E_s^{\perp} \sim K_s \left(h/l_p\right)^4 l l_p$ when it is placed across the axis. The net result is that when the polymer is bound to a surface that is easily stretchable, i.e. sufficiently thick, it will spontaneously wrap around its axis. In the limit of an unstretchable, i.e. very thin surface, the polymer will align with the cylinder axis. The intermediate regime is dominated by helical configurations which represent a balance between the two tendencies. By holding h constant and altering the relative weight of bending and stretching energies we can modulate the pitch of the helix and establish its dependence on the mechanical properties of the membrane.

The angle θ formed between the axis of the cylinder and the direction of the polymer can be dimensionally related to the two natural length scales of the problem: the axial, l_p, and the transversal, R

$$\tan(\theta) \sim \left(\frac{R}{l_p}\right) \sim \left(\frac{1}{h^{\frac{1}{2}} \left(K_s/K_b\right)^{\frac{1}{4}}}\right). \tag{6.1}$$

This functional form has the correct limiting behavior. In the stretching dominated regime $\theta \to 0$, and in the bending dominated regime $\theta \to \pi/2$. It is important to notice that one should be able to modulate the helicity of the polymer by increasing its binding energy to the surface (i.e. h). However, for sufficiently large values of h the system can become kinetically trapped, or crosses over to the scaling behavior $l_p \sim R^{3/2}/t^{1/2}$ [207], which is independent of h. It is therefore clear how variations of h have a weak effect on the pitch of the polymer.

To test our theoretical predictions, we performed a series of numerical simulations in which we carefully investigated the dependence of θ on the membrane stretching rigidity, and on the indentation h. The amplitude of the indentation, h, is tuned by changing the strength of the monomer-bead attraction (binding energy) D_0, and can be estimated by computing the largest vertical distance among the surface beads underneath a given monomer. Fig. 6.3a) shows how θ depends on K_s for fixed bending rigidity, K_b, and indentation, h. The line is a fit to the data obtained by using the inverse of the functional form in Eq. 6.1.

Fig. 6.3b) shows how θ depends on the binding energy D_0 which, for fixed K_s and K_b, and within the narrow range of values of D_0 we explored, grows linearly with h. We repeated the calculation for two different values of K_s and fit the data with the inverse of Eq. 6.1. In both cases Eq. 6.1 appropriately describes the helicity of the polymer in terms of the elastic properties of the membrane. The inset of Fig. 6.3a) shows the representative snapshots of the polymer conformations for different values of K_s at constant h and K_b.

6.5 Polymer persistence length

Two important points need to be emphasized. (1) The physical origin of the disordered-to-helix transition of the chain can be understood in terms of the usual balance between the entropy of the filament and the energy penalty associated with a random, non-optimal distribution of indentations on the surface. (2) By going through the transition the filament acquires a large effective bending rigidity which results in a persistence length several times larger than the chain length.

The jump in persistence length of the polymer can be best observed by measuring a function that accounts for the periodic correlation between the monomers, as described in [208]:

$$G(m) = \frac{1}{N_m - 3} \sum_{i=1}^{N_m - 2} g(m, i). \tag{6.2}$$

Here m is the number of monomers between particle i and j along the chain, and $g(m, i)$ is given by

$$g(m, i) = \frac{(N_m - 1) \sum_{j=1}^{N_m - m - 1} (s_{i,j} - \overline{s_{i,j}})(s_{i,j+m} - \overline{s_{i,j}})}{(N_m - m - 1) \sum_{j=1}^{N_m - 1} (s_{i,j} - \overline{s_{i,j}})^2} \tag{6.3}$$

where $s_{i,j} = \cos\theta_{i,j}$ is the cosine of the angle between bond vectors i and j, and $\overline{s_{i,j}}$ is the average over all such angles in the chain.

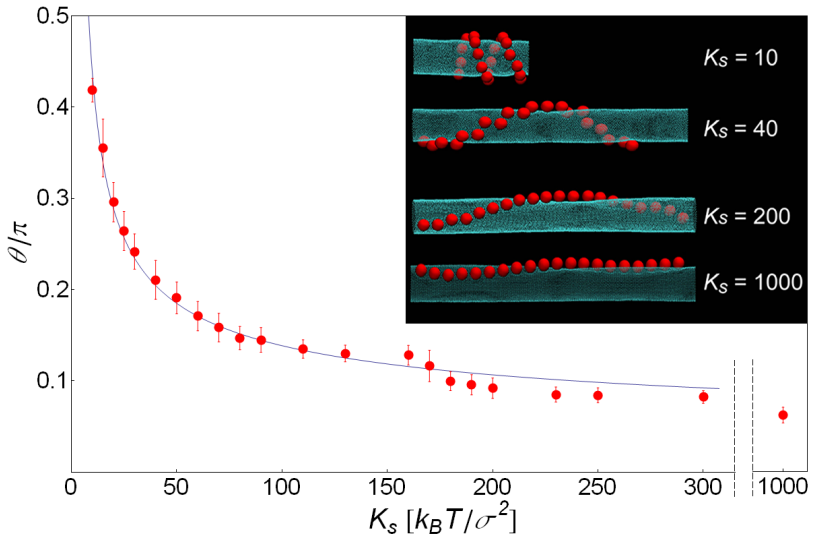

(a)

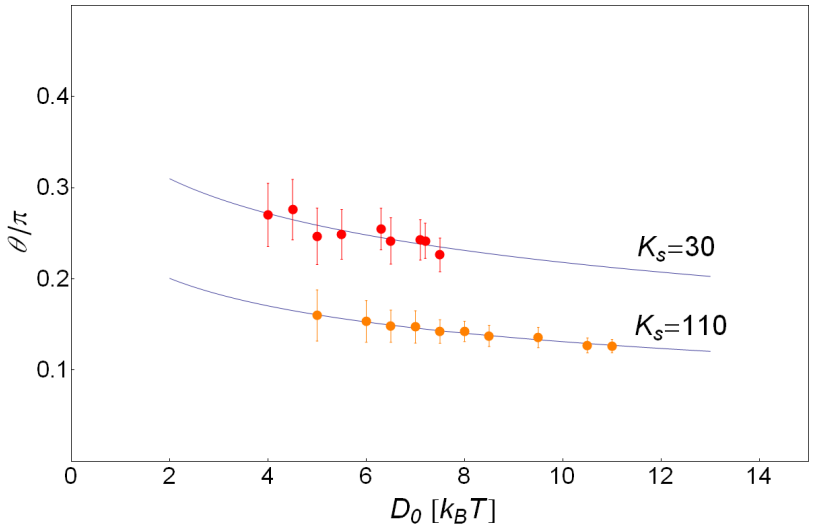

(b)

Figure 6.3: (a) Variation of θ as a function of K_s at fixed $h \approx 1.17\sigma$ and $K_b = 150k_BT$. The solid line indicates the fit to the data using the inverse of Eq. 6.1. The inset shows the representative helices form increasing values of K_s. (b) Variation of θ as a function of the binding energy D_0, at $K_b = 150k_BT$, for two different values of the stretching constant: $K_s = 30k_BT/\sigma^2$ and $K_s = 110k_BT/\sigma^2$. The solid line indicates the fit to the data using the inverse of Eq. 6.1.

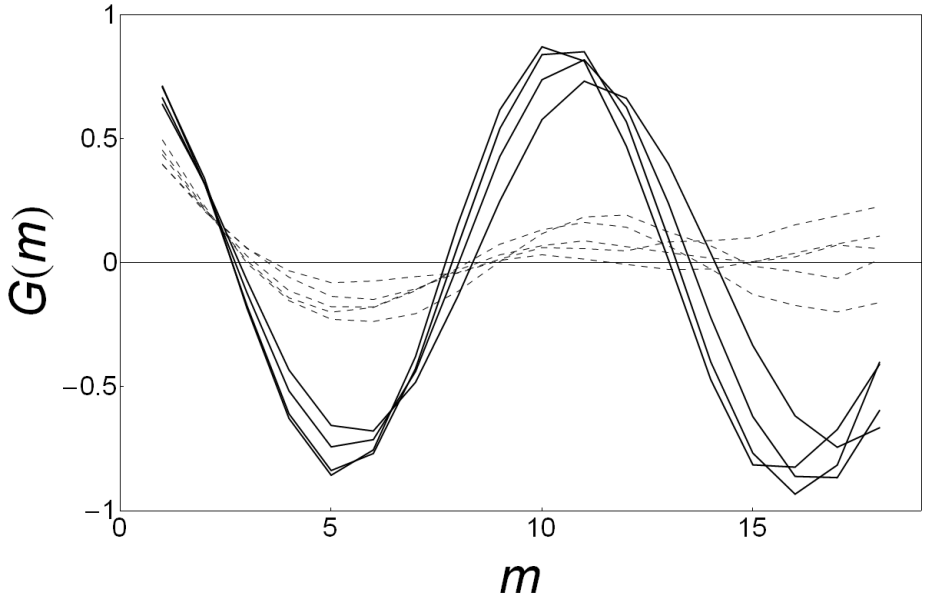

Figure 6.4: $G(m)$ as calculated from Eq. 6.2 at $K_s = 10k_BT/\sigma^2$, $K_b = 150k_BT$, for different values of D_0. The jump in persistance length is observed around $h \simeq 0.5\sigma$. We indicate $G(m)$ with dashed lines for $h < 0.5\sigma$ and we use solid lines for $h > 0.5\sigma$.

Fig. 6.4 shows $G(m)$ for different values of h at $K_s = 10k_BT/\sigma^2$ and $K_b = 150k_BT/\sigma^2$, and clearly indicates two distinct cases. For $h < 0.5\sigma$ the correlation between the relative location of the monomers on the surface is negligable, while for $h > 0.5\sigma$, $G(m)$ shows perfect helical correlation of monomers over a distance that is larger than l. Since $G(m)$ does not decay, it is obvious that our polymer is too short for a reliable estimate of the persistance length in the helical phase. However, the persistence length clearly exceeds the chain length over several times.

What limits the length of the polymer in our simulations is the large number of triangles required to describe the cylindrical surface. In fact, to avoid the artifacts due to the specific tesselation of the surface, monomers need to be significantly larger than the surface beads. We find that the $\sigma_m = 10\sigma$ is enough for the monomers not to feel the underlying structure of the membrane. Interestingly, when the monomer size becomes comparable to the size of the surface beads, we find that the direction

of the chain is biased along the main axes of the mesh. This is a reminder that below a certain length scale, the structural details of the underlying surface cannot be neglected.

6.6 Conclusion

In conclusion, it is important to emphasize two things. The first is that the onset indentation amplitude h for helical conformation is typically just a small fraction of the monomer size (barely 5% in the case described above) which is not an unreasonable perturbation even for simple membrane-bound proteins. The second is that although in this Chapter we have focused specifically on the problem of flexible chains on cylindrical surfaces, the nature of this phenomenon is quite general and is intrinsically connected to the nonlinear response to deformations of elastic sheets. This behavior can be generalized to arbitrary geometries − we find that filaments also acquire very peculiar conformations when placed on spherical or toroidal deformable shells [126] − and more importantly can be extended to any component adhering to the surface. We can anticipate [209] that elastic surfaces can be used to drive self-assembly of hard colloidal particles resulting in a variety of geometric patterns not unlike the ones observed with the filaments. Clearly the specific details of the long-range correlations induced by the surface will depend on the surface topology, and on the physical constraints of the macromolecules adhering to it. Nevertheless, it is the interplay between the stretching and bending modes of the surface that will determine the effective interactions between the components bound to it and the overall geometry of the aggregates.

Our hope is that the results presented in this Chapter will stimulate experimentalists to further study the elastic and mechanical properties of elastic sheets and, in particular the long range correlations arising when particles bind to it.

Chapter 7

Collapse transition of nanoparticle-laden nanotubes

7.1 Introduction

Nanotube-nanoparticle composites are currently one of the most promising hybrid materials. Combining the unique properties of these two components can result in exceptional mechanical, electronic and optical properties [210]. Efficient protocols for decorating carbon, silica or polymeric nanotubes with a variety of inorganic nanoparticles have opened novel avenues for their application in nanotechnology [211–216]. Up-to-date nanoparticle-nanotube composites have successfully been used as chemical- and biosensors [217–219], catalysts and catalyst supports in fuel cells [220–222], high-strength engineering fibers [223, 224], as well as components in nanoelectronics [225], photovoltaics [226] and neural nets [227]. Understanding the interactions between nanoparticles and nanotubes, as well as the structural properties of their assemblies, is essential for the successful design and manipulation of these materials. Here, we consider how the self-assembly of adhering nanoparticles drives a peculiar collapse transition of nanotubes that has the potential to broaden the application of this class of hybrid materials.

The thin walls of hollow nanotubes render them quite flexible when subjected to radial deformation, even when their stiffness in the axial direction is extremely high. Consequently, nanotubes are prone to radial buckling. Due to the importance of this transition, a significant body of work has been dedicated to understanding the radial buckling and collapse of nanotubes under point-like mechanical loading or isotropic compressive stresses [228–231]. Radial buckling of carbon nanotubes within a carbon nanotube fiber has been shown to improve the mechanical strength of the fiber [223, 224]. Such a collapse also strongly affects the nanotube's electrical properties, inducing for example their semiconductor-metal transition in single and double walled carbon nanotubes [232–234]. Furthermore, the catastrophic collapse of cytoskeletal microtubules under large radial loads has been reported [207], though its biological significance is still unclear. In all cases, the process is characterized as a discontinuous transition that depends only on the nanotube radius and that is often directed by attractions between the opposite walls of the nanotube.

In this Chapter we show how the collective behavior of nanoparticles assembling on a deformable nanotube can promote this transition, even when the walls of the nanotube are fully noninteracting, and can result in an ordered nanoparticle engulfment inside the collapsed structure. In our simulations the nanotube is modeled in a coarse-grained fashion as a generic elastic tubular surface which, depending on the specific choice of mechanical parameters, can represent a hollow nanotube of a broad range of materials. We study the process for different values of bending stiffness (Young moduli) of the nanotube and characterize the dependence of the transition on the ratio of nanotube/nanoparticle radii, the concentration of the nanoparticles, and the strength of the nanoparticle adhesion to the nanotube walls. We demonstrate how the collapse and nanoparticle engulfment can be controlled and reversed by tuning the strength of nanoparticle adhesion, which can be achieved for instance by changing the properties of the medium, suggesting a new class of environment-responsive nanocomposites.

7.2 Simulation details

We model the nanotube as an elastic membrane of cylindrical shape, using a standard triangulated mesh of hexagonal symmetry [101]. Hard spherical beads of diameter σ are placed at each node of the membrane in order to impose surface self-avoidance, and any two surface beads interact via a repulsive truncated-shifted Lennard-Jones potential, as in Eq. 5.1.

Each bead of the surface is linked to its immediate neighbors *via* the harmonic spring potential of a constant K_s (Eq. 5.2).

Keeping K_s constant, we modulate the bending rigidity of the surface according to a dihedral potential between adjacent triangles of the mesh, as given in Eq. 5.3. K_b is the bending constant that sets the bending rigidity of the surface.

The ratio between stretching and bending constants is simply related to the thickness of the material t, $K_s/K_b \simeq (1/t)^2$ [36], and in this work we focus on the limiting behavior of nearly unstretchable tubes ($\sigma^2 K_s/K_b \geq 10^2$), corresponding to nanotubes with very thin walls. An analogous continuous mechanics descriptions of nanotubes has been shown to be applicable even to study the mechanical properties of carbon nanotubes containing as little as about 10 atoms on the perimeter [228].

Nanoparticles of diameter $\sigma_c = 10\sigma$ are described *via* the repulsive truncated-shifted Lennard-Jones potential above. Generic nanoparticle adhesion to the membrane is described by the Morse potential of a depth D_0, as given by Eq. 5.4. The interaction cutoff is set to 7σ (i.e. 70% of the nanoparticle diameter) and the decay factor to $\alpha = 1.25/\sigma$. Nanoparticles appear to each other as hard spheres, interacting via Eq.(5.1) with $\sigma \to \sigma_c$. Simulations were carried out using the LAMMPS molecular dynamics package [196]. To allow for stretch-free configurations, changes in the length of the box parallel to the nanotube axis (the x-axis in our case) are included by employing an NP_xT ensemble with $P_x = 0$. The timestep was set to $dt = 0.002\tau_0$ (τ_0 is the dimensionless unit of time). We varied the bending rigidity, K_b, the radius of the tube, R, as well as the number of nanoparticles, N, and their adhesion to the

nanotube, D_0, to characterize how the binding of the particles drives the collapse of the nanotube.

7.3 Collapse of the nanotube

Nanoparticles exhibit three distinct phases upon adhesion to the surface, as depicted in Fig. 7.1, depending on the binding constant D_0. The first is a gas phase that arises when D_0 is insufficient to overcome the resistance to deformation imposed by the bending rigidity and the particles randomly diffuse over the surface (Fig. 7.1(a)). As D_0 is increased, the nanoparticles slightly deform the tube and self-assemble into linear string-like aggregates which are aligned with the cylinder's axis and partially wrapped by the surface, albeit never fully (Fig. 7.1(b)). This phase is a consequence of the inherent tendency of thin sheets to respond to a deformation by bending uniaxially, the only stretch-free way. Since the stretching rigidity of the surface is much higher than its bending rigidity (the nanotube's walls are very thin), the axial direction is the preferred direction of the deformation and promotes nanoparticle self-assembly into long lines [123, 124, 209]. However, the range of D_0 for which this occurs is relatively narrow, and the phase invariably appears in coexistence with the first gaseous phase, with the majority of the nanoparticles arranging in linear formation and a few diffusing to either side of it.

As soon as the nanoparticle adhesion or concentration is slightly increased, the linear phase becomes unstable and the third phase (hereafter *collapsed*) occurs, as shown in Fig.7.1(c). This illustrates that in the high-stretching and binding limits, incompletely wrapped axial lines are unstable and as the particles become entirely wrapped by the surface in order to maximize the energy gained by nanoparticle-nanotube binding interactions, the surface collapses to generate a uniform buckle along the axis of the tube. In this configuration, nanoparticles are arranged into strings and are firmly contained within the tubular inner fold. By reversing the tran-

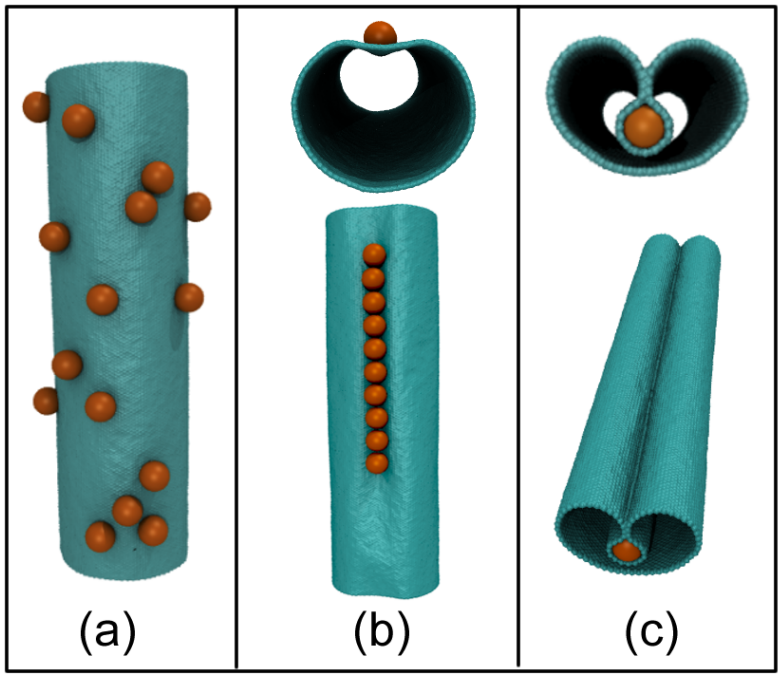

Figure 7.1: Snapshots of three possible phases upon nanoparticle (orange) adsorption on the nanotube (blue). (a) The random gas state. (b) The axial linear aggregate of nanoparticles. Top panel shows the cross-section when looking down the cylinder axis, the bottom panel shows the view from above. (c) The collapsed state in which a self-assembled linear aggregate of nanoparticles is completely wrapped by the surface of the nanotube. The panels are analogous to those in (b).

sition, for instance by decreasing the nanoparticle binding with changing experimental conditions, a mechanism similar to responsive nanocaging could be achieved.

7.4 Onset binding energy for the collapse

To characterize the transition from the axial structures to the stable collapsed state, it is insightful to relate the *onset value* of binding $D_0{}^*$ (i.e. the first value of D_0 that is sufficiently large to induce collapse) to the mechanical properties of the surface and the number of nanoparticles in the system. To obtain cleaner results, we initially

prepare the nanoparticles in linear formation just above the surface of the tube and oriented parallel to the axis of the cylinder. However, it should be emphasized that the linear configuration is also the lowest-energy configuration, as explained above, and reported in [124]. We let the simulation equilibrate and measured the average extent of particle wrapping by the surface, ϕ, as a function of increasingly larger values of D_0. Particle wrapping is defined as the total surface area of the nanotube in contact with a nanoparticle, S_0, divided by the surface area of a nanoparticle, $\phi = S_0/(4\pi\sigma_c^2)$. We consider a bead of the nanotube to be in contact with a nanoparticle when their center-to-center distance is within the cut-off of the Morse potential. Clearly, $\phi = 1$ would imply complete wrapping of the nanoparticles. However, because of the large energy costs associated with the stretching energy, this scenario never occurs in our system and the maximum particle wrapping is achieved when a linear aggregate is completely enveloped by the nanotube (as depicted in Fig.7.1(c)). This configuration yields typical wrapping values per particle of $\phi \simeq 0.4$. To understand the nature of the transition, we also examine the reverse process, i.e. we repeated the simulations for the same set of parameters, but choosing a fully wrapped linear aggregate as an initial configuration and by decreasing D_0 until the buckle is released and the cylindrical geometry is restored. This analysis has been repeated for different values of K_b, R, and number of particles, N.

The collapse transition for three bending rigidities is illustrated in Fig. 7.2, and shows that there is a clear discontinuity in nanoparticle wrapping parameter above an onset value ${D_0}^*$, corresponding to a first-order transition. Not surprisingly, as K_b increases, ${D_0}^*$ shifts to higher values due to larger energy needed to deform the surface. Simulations for the reversed process, which started from a wrapped state, show that nanoparticle engulfment can indeed be reversed, with D_0 for the nanoparticle release being lower than the onset ${D_0}^*$ needed to promote the collapse. We observe hysteresis broadening for higher values of K_b, indicating a higher energy barrier for the collapse of stiffer nanotubes, but also for the reverse process. This result is important because

it suggests a simple way to control the stability of the collapsed state, against restoring forces.

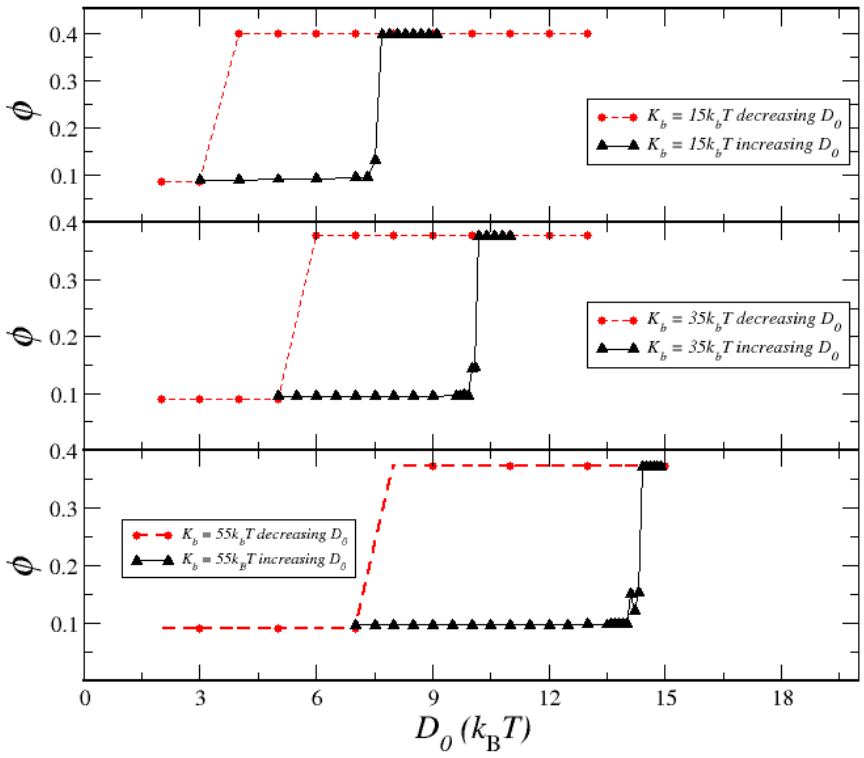

Figure 7.2: From top to bottom, hysteresis plots for $K_b = 15k_BT$, $K_b = 35k_BT$, and $K_b = 55k_BT$, respectively. For each plot, triangles (black) represent the forward direction, whose initial configuration is a line of nanoparticles just above surface of the cylinder and parallel to its axis, and circles (red) represent simulations whose initial configuration is the fully wrapped linear aggregate (see Fig.7.1c). The onset value of collapse, $D_0{}^*$, increases with increasing K_b, accompanied by the hysteresis broadening. Here, $R = 25.4\sigma$ and $N = 15$

Our data also reveal that $D_0{}^*$ increases when decreasing the radius of the cylinder or the number of nanoparticles (Fig. 7.3). In the first case, the nanoparticles need to deform against a larger curvature in order to adhere, resulting in higher values of $D_0{}^*$. This is analogous to the well-known fact that carbon nanotubes of smaller radii

are more stable against buckling [229], and it is due to the smaller cost associated to bending deformations of wider tubes. Additionally, since the collapse transition is a consequence of a collective behavior of nanoparticles, at lower nanoparticle densities the surface is deformed to a lesser extent resulting in greater $D_0{}^*$.

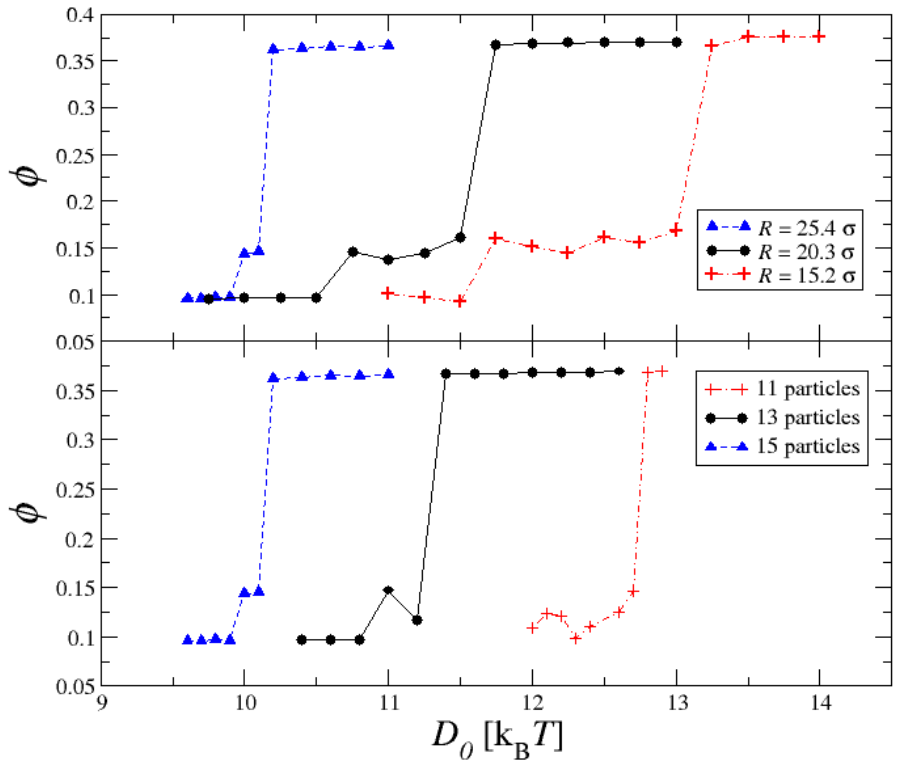

Figure 7.3: Top panel: The onset value of collapse, $D_0{}^*$, increases as the nanotube radius R decreases because the nanoparticles need to deform against the larger curvature. $K_b = 35k_BT$ and $N = 15$ are kept constant. Bottom panel: $D_0{}^*$ increases as the number of nanoparticles N decreases due to lesser collective deformation by the particles. $K_b = 35k_BT$ and $R = 25.4\sigma$ are kept constant.

7.5 Scalling analysis for the onset binding energy

Our findings suggest a general scaling law relating ${D_0}^*$ to the mechanical and geometric properties of the surface, and the number of adhering nanoparticles. A good place to start are the scaling laws for the deformation of thin elastic sheets. As explained in Chapter 6, when a thin sheet of a thickness t, width w, and mechanical parameters K_b and K_s, is subject to a deformation of amplitude h, the associated bending and stretching energies scale as $E_b \simeq K_b \left(h/w^2\right)^2 w l_p$ and $E_s \simeq K_s \left(h^2/l_p^2\right)^2 w l_p$, where l_p is the extent of the axial deformation. Minimizing the sum of the bending and stretching energies contributions with respect to l_p gives $l_p \simeq w h^{\frac{1}{2}} \left(K_s/K_b\right)^{\frac{1}{4}} = w(h/t)^{1/2}$, a well known expression for the persistence length of a point-like deformation. This result can be generalized to a cylindrical surface of radius R when $h \ll R$ −which is the relevant case to study the onset of the collapsing transition − and one recovers the large deformation limit $l_p \simeq R(R/t)^{\frac{1}{2}}$ by setting w and h equal to R [207].

A single particle adhering to an elastic surface imprints a deformation whose shape can be approximated by that of a spherical cap of a height h and radius σ_c. Binding energy is then $E_{\text{bind}} \simeq -\pi D_0 h \sigma_c/\sigma^2$, where $\pi h \sigma_c/\sigma^2$ accounts for the degree of wrapping of the nanoparticle, i.e. the number of membrane beads it is in contact with. As the depth of the deformation, h, is now controlled by the binding constant D_0, we can perform the same minimization described above with the additional energy contribution due to the biding energy, and obtain an expression for the equilibrium value of h, namely

$$h^{\frac{1}{2}} \sim \frac{\left(D_0 \sigma_c R^2\right)^{\frac{1}{3}}}{\left(\sigma^8 K_s K_b^3\right)^{\frac{1}{12}}}. \tag{7.1}$$

The expression for the extent of the deformation along the axis of the cylinder, l_p, upon binding of one nanoparticle, can then be re-written as

$$l_p \sim \left(\frac{K_s{}^{\frac{1}{3}}}{K_b}\right)^{\frac{1}{2}} \left(\frac{R^5 D_0 \sigma_c}{\sigma^2}\right)^{1/3}. \tag{7.2}$$

In the case of a single indentation, a necessary condition for the buckling transition to span the entire axis of the cylinder thus leading to the collapse is that $l_p > L$, where L is the length of the cylinder. Whenever $l_p < L$ uniform axial buckling does not occur and a local transversal deformation involving the formation of two stress points does instead take place as shown in Fig. 7.4(a).

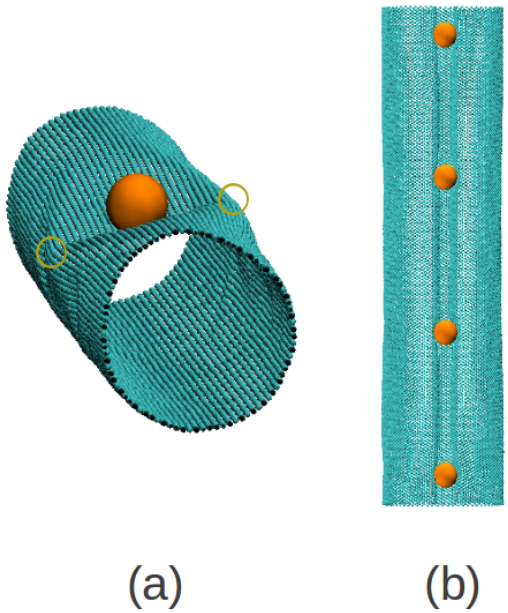

Figure 7.4: (a) Transversal bucking caused by a large single point deformation. In this case $l_p < L$, and the side rings indicate the location of the transversal stress focus points. (b) Uniform axial buckling and nanotube radial collapse induced by four equidistant localized deformations such that $4l_p > L$.

These arguments suggest that the collapse of an elastic tube indented by N equidistant and well spaced binding particles can occur whenever $L^* \equiv Nl_p \geq L$, i.e. when the persistence lengths from each independent deformation couple and

span the length of the cylinder (see Fig. 7.4(b) for an illustration). Our system is a bit different from the case discussed above, in fact, in the linear aggregates self-assembled in our study − precursors configuration for tube collapse − particles are in contact with each other, and typically $l_p \gg \sigma_c$, suggesting that a more appropriate measure for the extent of the total longitudinal deformation is $L^* = N\sigma_c + l_p$. Imposing that the correlation of the axial deformations between the particles extends beyond the length of the tube, $L^* \geq L$, leads to a scaling law for D_0^*

$$D_0^* \geq \frac{(L - N\sigma_c)^3 \sigma^2}{\sigma_c R^5} \left(\frac{K_b^3}{K_s}\right)^{\frac{1}{2}}. \tag{7.3}$$

It should be stressed that in this formula, N is not the total number of particles in the system, but the length of the aggregate driving the collapse transition. To test this scaling ideas, we inserted data from all our simulations for various values of D_0, K_b, R and N into a single scatter plot, which has the right-hand side expression of Eq. (7.3) on the y-axis, and the binding constantD_0 on the x-axis, as shown in Fig. 7.5. The points are marked as "collapsed" and "not collapsed", according to the final state of the simulation. There appears a distinct division between data corresponding to the collapsed state and those that do not, verifying the validity of the scaling law given in Eq. (7.3). We expect deviations to this scaling law when the diameter of the tube becomes comparable to that of the particles, as in this case a more accurate estimate of the elastic energies of the nanotube would be required to better take into account its global deformation.

7.6 Conclusion

In conclusion, in this Chapter we have studied a system of nanoparticles adhering to an elastic unstretchable nanotube. We have shown how the nanoparticles self-assemble into a linear aggregate which promotes the collapse transition of the nanotube, resulting in nanopaticle entrapment. The collapse is easier if the nanotube

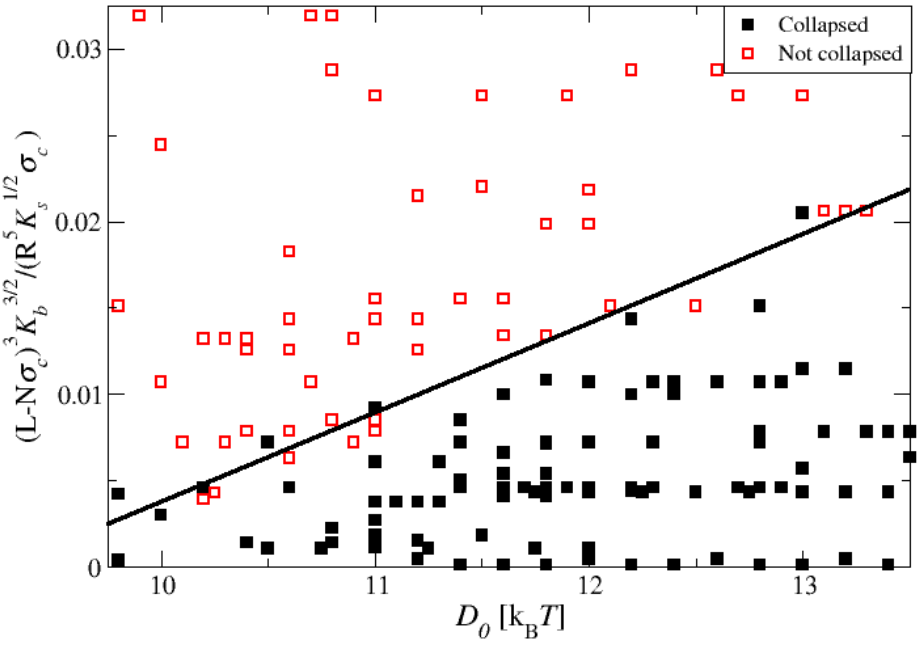

Figure 7.5: Testing the scaling law presented by Eq. (7.3): scatter plot of all simulation data. The right-hand side of Eq. (7.3) is plotted on the y-axis versus D_0 from the simulation. Open squares represent simulations which did not induce a collapsed state, while filled squares represent simulations which have ended in a collapsed state. In both cases the initial state was a non-collapsed linear aggregate prepared above the surface of the nanotube containing N particles. The straight line is provided as a guide to the eye to emphasize the clear division between the data.

radius or the nanoparticle concentration are increased, and the bending rigidity (the material thickness) is decreased. Using the elasticity theory for thin sheets we establish a scaling law linking the onset of binding energy to the collapsing transition in terms of the elastic and geometric properties of the tube. Finally we show how the process can be reversed and we how its hysterectic cycle widens with the bending rigidity of the tube. We suggest that this feature can be exploited to design particle

nanotraps, but also as a way to enhance the mechanical strength of nanoparticle-nanotube composites, in addition to altering their electric and optical properties. Clearly the release (un-buckling) transition can be further stabilized by adding a weak attraction between the layers of the nanotube. Although our work focused primarily on the low particle density limit, it would nevertheless, be interesting to generalize our scaling laws for buckling in the presence of multiple linear aggregates (in the large particle coverage limit) and to understand how the presence of one axial collapse may influence the occurrence of further collapse of the nanotube. We expect this effect to be important when $\sigma_c \sim 2R$. We hope that our research will stimulate experimental investigations of the nanoparticle-induced collapse of nanotubes as well as its application in nanotechnology.

Chapter 8

Nanoparticle self-assembly on elastic shells

8.1 Introduction

In this Chapter we try to understand how closed elastic surfaces, such as spherical shells, can be used to drive self-assembly of nanoparticles. What makes this problem very interesting is that unlike planar or cylindrical geometries, for which there is a clear solution to the stretch-free deformation problem, any deformation of a spherical shell will necessarily involve stretching of the surface. The shape of the deformation minimizing the stretching energy in this case is therefore far from obvious. Furthermore, a buckling transition from the spherical to a faceted icosahedral shape is known to take place at large stretching energies [235]. In addition to that, for sufficiently small shells (or large deformations) the ratio between bending and stretching energy becomes independent of h, and only depends on the radius of the sphere R and its thickness t, $E_s/E_b \sim (R/t)^2$ [36]. Such complexity of elastic shells can give rise to very peciliar and beautiful aggregation patterns.

In Chapters 5 and 6 we have shown how the response to deformations of elastic sheets and nanotubes can drive self assembly of colloidal particles into straight and

curved lines [123, 209] and can alter the elastic properties of a flexible filament binding to it [124]. Here we will show how the elastic response to deformations of a spherical shell can be used to self-assemble colloidal particles in a variety of patterns that only depend on the mechanical properties of the system and the amount of deformation of the surface. We will also show how a fully flexible polymer bound to the shell will spontaneously arrange to conform to similar patterns observed for the nanoparticles.

8.2 Simulation details

We model the elastic surface via a standard fishnet network representation[101]. Each node of the network is placed to conform to the symmetry of an icosadeltahedron. In such surfaces, like viral shells, all but 12 nodes have a regular triangulation with six neighbors; 12 five-fold disclinations are also present as required by Euler's theorem relating number of faces, edges and faces on a spherical triangulation. The number of nodes N_k describing the surface is then related to the location of the five disclinations, and satisfies the constraint $N_k = 10(n^2 + nm + m^2) + 2$. Here n and m indicate that one must move n nodes along the row of neighboring bonds on the sphere, and then after a turn of 120°, move for m extra steps [236].

We studied two different sphere sizes; the smaller one has $N_k = 6752$ nodes and symmetry described by $n = 15$ and $m = 15$, the larger one contains $N_k = 10832$ nodes with $n = 19$ and $m = 19$.

To impose surface self-avoidance we place hard beads at each node of the mesh. Any two surface beads interact via a purely repulsive truncated and shifted Lennard-Jones potential, according to Eq. 5.1.

We enforce the surface fixed connectivity by linking every bead on the surface to its first neighbors via a harmonic spring potential with the associated spring constant K_s, as in Eq. 5.2.

The bending rigidity of the elastic surface is modeled by a dihedral potential

between adjacent triangles on the mesh, as in Eq. 5.3, with K_b being the bending rigidity.

Colloidal particles of diameter $\sigma_c = 10\sigma$ are described via the repulsive truncated-shifted Lennard-Jones potential introduced in Eq. 5.1 with $\sigma \rightarrow \sigma_c$. Finally the polymer is constructed as a "pearl necklace" with $N \in [20, 45]$ monomers of diameter also $\sigma_m = 10\sigma$. Neighboring monomers are connected by harmonic springs as in Eq. 5.2, with an equilibrium bond length $r_M = 1.18\sigma_m$ and spring constant of $120k_{\mathrm{B}}T/\sigma^2$. Polymer self-avoidance is again enforced via the repulsive truncated-shifted Lennard-Jones potential introduced in Eq. 5.1, with $\sigma = \sigma_m$.

The generic binding of the polymer monomers (and the colloids) to the surface is described by a Morse potential, given by Eq. 5.4, with D_0 being the depth of the well, i.e. the surface-colloid binding constant. The interaction cutoff is set at 10σ and $\alpha = 1.25/\sigma$.

We used the LAMMPS molecular dynamics package [196] with a Nosé-Hoover thermostat [237, 238], in the NVT ensemble to study the statistical behavior of the system at room temperature. The timestep size is set to $dt = 0.002\tau_0$ (τ_0 is the unit time expressed in standard MD units) and each simulation was run for a minimum of $5 \cdot 10^6$ steps. The radii of the undeformed spherical shells are $R = 29.05\sigma$ for $N_k = 6752$, and $R = 34.16\sigma$ for $N_k = 10832$.

8.3 Shell buckling and the phase behavior

To understand how the configurational properties of the binding polymer and colloids are related to the elastic properties of the templating surface, we performed a series of simulations for many values of K_s, K_b, D_0 which controls the extent of the surface indentation) and for different polymer lengths and number of colloidal particles. We find that a convenient way of representing our data is via the dimensionless parameter known as the Foppl-Von Kàrmàn number, defined as $\gamma = YR^2/\kappa_B$, where Y is the

Young modulus of the shell and κ_B is the bending rigidity as defined in the continuum theory of elasticity [36, 239]. We begin our analysis by studying the buckling transition of the shell as a function of γ in the absence of binding agents. This will give us critical information about how to relate the shape of the templating surface (the elastic shell) and its elastic properties. To identify the buckling transition and match the numerical parameters of our model with γ we follow the analysis carried out in [101]. Fig. 8.1A shows the results of our simulations. The surface asphericity A, defined as

$$A = \frac{\langle \Delta R^2 \rangle}{\langle R \rangle^2} = \sum_{i=1}^{N} \frac{(R_i - \langle R \rangle)^2}{\langle R \rangle^2} \ , \tag{8.1}$$

R_i being the radial distance of the surface bead i and $\langle R \rangle$ being the mean radius of the shell, is plotted againts $\gamma = (4/3)K_s R^2/K_b$. The buckling transition, for which the spherical shape begins to facet, begins for values of $\gamma \gtrsim 10^2$. This result is in good agreement with that computed in [235], and represents a good test of our numerical model. We next add colloidal particles to the system and observe their self-assembly on the surface of the spherical shell. Depending on the value of γ, particles arrange in patterns that minimize the elastic energy of the shell. Figure 8.1B shows the resulting patterns as a function of γ for different values of indentation, and a constant number of colloidal particles $N = 35$. A convenient way of extracting the indentation is obtained by computing $(A_p - A)^{1/2}$, where A_p is the asphericity of the shell in the presence of the particles and A is the asphericity without them.

The general feature of the diagram is that self-assembly occurs for only a relatively narrow range of particle deformations. When $(A_p - A)^{1/2}$ is too small, i.e. the surface is basically unaffected by the presence of the particles, we find no aggregation; this is the result one should indeed expect when placing N noninteracting hard particles on the surface of a rigid sphere (al low densities). We indicate this phase as the *gas phase*. When $(A_p - A)^{1/2}$ is too large and significant deformations are induced by the binding particles, we find that the system becomes kinetically trapped (at least within the timescales considered in this study) into metastable states. In fact,

repeating the simulations under the same conditions leads consistently to different and not well defined aggregation patterns. We indicate this phase as the *arrested phase*. For intermediate deformations, particles consistently self-assemble in a variety of patterns whose features are clearly related to the mechanical properties of the shell via γ.

For small values of γ we find that particles aggregate isotropically to form a two dimensional crystal on top of the sphere. The presence of these 2d crystals tends to flatten the surface underneath it. As a consequence, if a sufficiently large number of particles is added to the system we find that the side length of the crystal is limited by the shell diameter, and extra particles begin to aggregate on its opposite side (Fig. 8.1B-I). As γ becomes larger, at low surface coverage, particles become localized over the twelve disclinations, and as N increases linear aggregates initially grow by linking the five fold disclinations on the sphere and finally form a linear network with 3-line joints winding around the disclinations in the shell (Fig. 8.1B-II). As the templating surface begins to facet, each segment of the network straightens revealing a clear patterns following the seams that a pentagonal tiling of the sphere would generate (a dodecahedron, Fig. 8.1B-III). It should be noticed that the previous two phases are topologically equivalent. The only difference is the presence of extra particles sitting on the twelve disclinations in region II of the diagram. Increasing the surface coverage in region III results in thickening of the width of the dodecahedral pattern by formation of parallel and adjacent secondary lines of particles.

At even larger values of γ, once the shell is well faceted, particles arrange into a linear and non-connected aggregate that smoothly winds around and away from the twelve disclinations (Fig. 8.1B-IV). This pattern is reminiscent of that of the baseball or tennis ball seam, the difference being that in our case the geometry of the aggregate is dictated by the presence of 12 topological defects, while in the baseball the seam winds around the location of the four $s = 1/2$ disclinations that a thin nematic liquid crystal texture would generate on a sphere [240, 241].

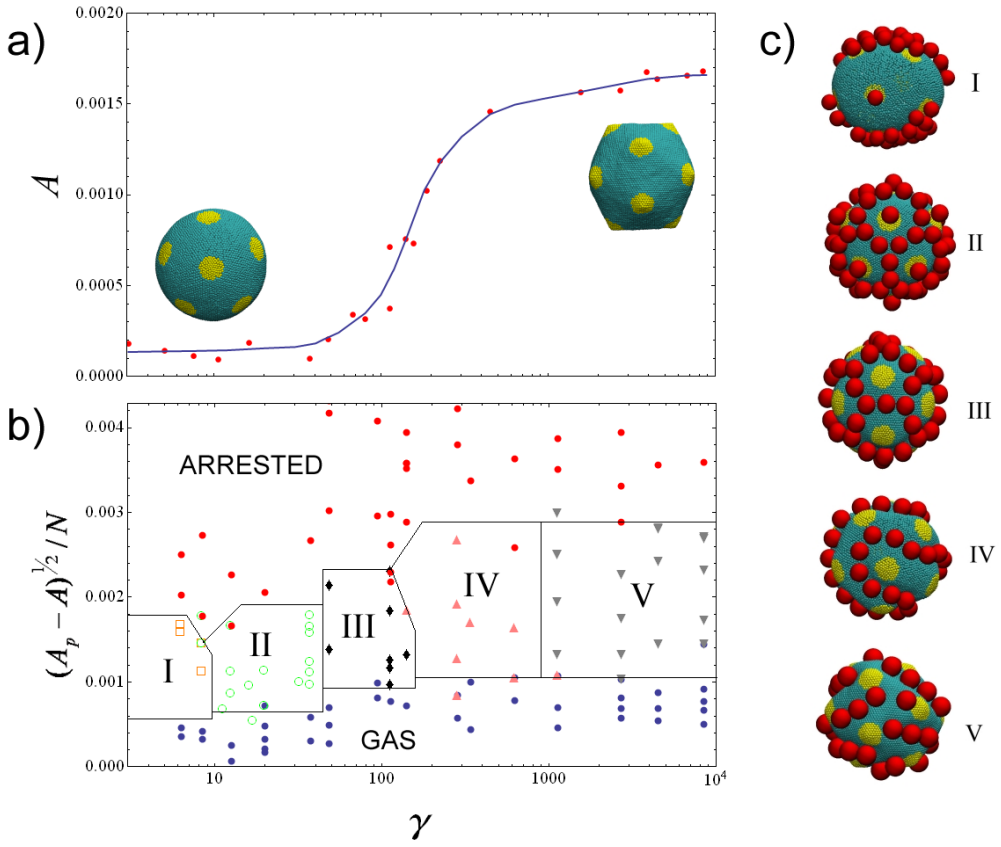

Figure 8.1: (a) Plot of the asphericity A versus Foppl-Von Kàrmàn number γ indicating the buckling transition in our model of a spherical elastic shell in the absence of colloidal particles. (b) Phase diagram indicating how the different aggregates formed by the colloidal particles depend on the mechanical properties of the shell (γ) and the degree of indentation measured in terms of the particle-induced asphericity $(A_p - A)^{1/2}/N$ computed using $N = 35$ particles. The five different phases are indicated with Roman numerals and include data for spherical shells of radius $R = 29.05\sigma$ and $R = 34.16\sigma$. Different symbols are used to emphasize simulation points that give rise to the different phases. (c) Snapshots from our simulations of the phases indicated in the phase diagram. From top to bottom $\gamma = 5.6$, $\gamma = 37.5$, $\gamma = 75$, $\gamma = 225$ and $\gamma = 4500$. For the sake of clarity, the particles defining the shell are depicted with a larger volume and the regions around the disclinations are depicted with a lighter color.

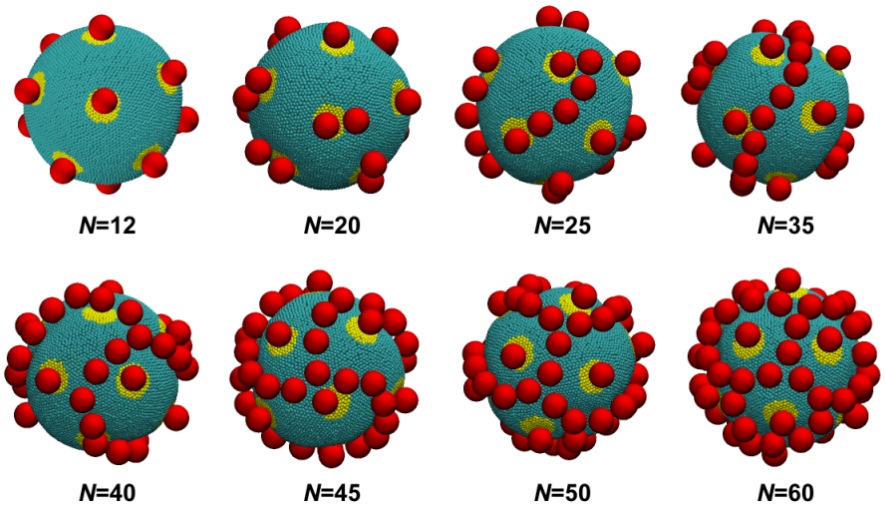

Figure 8.2: Snapshots showing the particle aggregates as a function of surface coverage for the phase II (see Fig. 8.1B). These snapshots are taken for a spherical shell with $\gamma = 37.5$ and $R = 29.05\sigma$.

Finally, for the largest values of γ we find that particles arrange into straighter but shorter aggregates (rods) that localize into ten distinct regions of the shell. The length of the rods grows with the surface coverage until a critical size which depends on the size of the sphere and equals roughly the distance between two disclinations located at the opposite vertices of two of the icosahedral triangles that share one edge (Fig. 8.1B-V). Further increase of N results in the formation of multiple rods per region which align parallel to each other. Figure 8.2 shows the explicit dependence of the pattern as a function of surface coverage in region II of the phase diagram.

8.4 Energy analysis of the shell

To gain insight into the physical origin of the different patterns formed by the particles, we measured the strain and bending energy at each node of the shell for different values of γ in the absence of the particles. Figure 8.3 shows the energy map of the

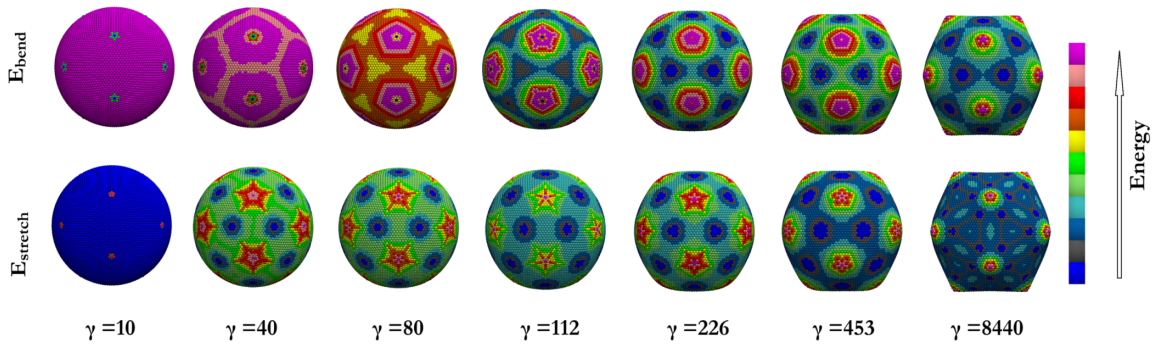

Figure 8.3: Bending energy map (top) and stretching energy map (bottom) of a spherical shell as a function of γ. Different shades indicate the relative strengths as indicated in the color map on the side.

two contributions for small, intermediate and large values of γ. The results are quite revealing and provide a simple framework from which the patterns can be understood. Particles aggregates align to follow the low bending and stretching energy regions on the shell. The formation of isotropic aggregates and the presence of the particles on top of the disclinations for small values of γ suggests that bending energy plays an important role in determining the pattern in region 1 and 2 of the diagram. Regions III, IV and V are instead completely dominated by the stretching energy which is driving the shape transition of the shell.

Of particular interest are the two phases that occur for very large values of γ (region IV and V). This condition that can be obtained either by increasing the radius of the sphere R or by significantly altering the relative weight of stretching and bending energies in favor of the former. In this regime particles can easily bend the surface in regions that are far away from the icosahedral vertices, yet the only bending deformations that will not induce stretching energy are those that involve bending around a single radius of curvature. We believe that the transition from the dodecahedral arrangement to the smooth closed loops in Fig. 8.1B region IV is due

to the large stretching energy cost that would be associated with the formation of either sharp corners or three-lines joints. This constraint become so severe in region V of the same figure, that the linear aggregates break into shorter pieces of roughly equal length that straighten by flattening the edges shared by any two triangles of the underlying icosahedral geometry.

8.5 Phases of an adsorbing polymer

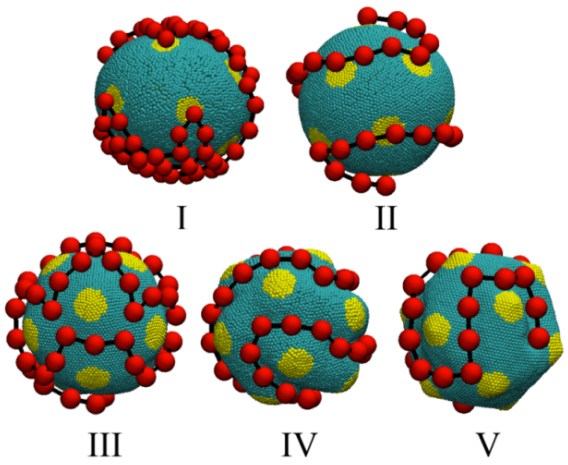

Figure 8.4: Snapshots showing the different conformations adopted by a fully flexible chain when binding to a deformable elastic shell. From left to right $\gamma = 5.6$, $\gamma = 37.5$, $\gamma = 112.5$, $\gamma = 140$ and $\gamma = 2700$.

Interestingly, we find that almost all phases depicted in Fig. 8.1 can also be acquired by a fully flexible chain binding to the shell for analogous degrees of deformations and comparable number of monomers. The only differences are due to the connectivity constraints on the chain. Region II and region V are obviously impossible to achieve with a chain; nevertheless, the difference in region V is minimal as short rods are in this case replaced by a poly-line with segments having the same length of the rods formed by the colloids.

In region II the polymer traces a simple path connecting the disclinations. Figure 8.4 shows snapshots of the different phases for the fully flexible chain. Given these similarities between the behavior of the polymer and that of the colloidal particles, it is clear that the mechanism regulating the conformational changes of the chain on a flexible shell is identical to that driving the self-assembly of the colloidal particles on the same surface.

8.6 Conclusion

In this Chapter we detailed how deformable elastic surfaces can be used to mediate self-assembly of otherwise noninteracting colloidal particles, and/or alter the conformational properties of a fully flexible chain bound to it. We find that the structure of the aggregates (the conformation of the polymer) can be understood in terms of the mechanical properties of the templating shell via the Foppl-Von Kàrmàn number γ. Specifically, we have shown how there are two distinct regimes: one dominated by the shell bending energy, and the other by its stretching energy. In the former case the shell acquires an overall spherical shape and particles localize on top of the disclinations and organize to link small bending energy regions. In the latter case the shell facets into an icosahedron with vertices located where the twelve five-fold disclinations reside; here particles follow low stretching pathways across the shell.

Crucially, the underlying shell's shape transition determines the role of the disclinations in the self-assembly process. The twelve five folded points attract the binding colloidal particles for small values of γ and repel them in the other regime. This result can be of great importance for controlling the functionalization of mesoparticles such as for instance colloidosomes [242]. In fact, we have shown how a small number of particles can be localized around the twelve disclinations in the bending dominated regime, and around the vertices of a dodecahedron (dual to the icosahedron) in the stretching dominated regime.

Our results can be considered as another example or an extension of the ideas discussed by Nelson [101, 240] regarding the functionalizability of the four $s = 1/2$ disclinations in a nematic liquid crystal texture covering a colloidal particle. One of the main differences, apart from the overall symmetry of the problem, is that in our case the shape of the template is allowed to change in response to the elastic strains induced by the presence of the defects, and that self-assembly (or conformational changes in a flexible chain) is driven by the elastic response to deformation of the shell. It would be interesting to study how particles self-assemble over a deformable shell under the overall tetrahedral symmetry provided by a nematic liquid crystal texture.

Chapter 9

Final remarks and future directions

In this Dissertation we have discussed the self-assembly of nanoparticles adsorbed on fluid and elastic membranes. We have found a plethora of aggregation patterns, whose stability can be explained by the interplay between mechanical properties of the surface and cooperative binding of many nanoparticles. Specifically, we have shown how fluid membranes can mediate linear aggregation of spherical particles for a wide range of biologically relevant bending rigidities. In the case of a very deformable membrane, this can be followed by an additional morphological transition - membrane tubulation. We have presented a detailed study of the tubulation mechanism, and have discussed how it compares to the competing process of membrane budding. When the membrane is cross-polimerized (elastic), the linear aggregates are again favorable, but they appear straighter. If a persistence length is associated to these aggregates, it can be tuned by changing the stretching rigidity of the surface, while their spatial orientation is controlled by the surface's geometry. Various organizational patterns of linear aggregates have been found on cylindrical and spherical shells, including helices and self-avoiding loops. We have demonstrated that nanoparticle aggregation can also lead to a reversible collapse of the underlying shell, a property which could be exploited in nanoparticle caging.

Although we have not covered the topic of multi-components systems, it is im-

portant to mention here the recent work by Olvera de la Cruz and collaborators [243, 244], as it bears important implications for the systems described so far. They studied phase separation of two or more component elastic shells using an effective elastic description of their local properties. Unlike most of the previous work on the subject, they also included explicitly the gaussian rigidity term in their energy balance. As explained in Chapter 2.1, κ_G is expected to be negative, it is proportional to the bending rigidity, and accounts for the topological changes of the membrane. Because a two component membrane can be described as a system of two surfaces, each constituted by its own component, mixed together and coupled via a line tension between them, arising for instance from different bending rigidities or chemical immiscibility, the energy coming from the Gaussian curvature cannot be considered constant and depends on the specific arrangements of the two components. A positive κ_G would occur with the line tension to form large domains with minimal mixing of the components, but $\kappa_G < 0$ leads to the destabilization of such phases promoting demixing. Using these arguments, Olvera de la Cruz and collaborators have studied phase separation and buckling of two component elastic shells as a function of composition and relative bending rigidities, and have reported patterns that are strikingly similar to those found in our study of particle self-assembly on elastic surfaces. These results suggest that the latter system can be described as an effective two-component system where the first component represents the fluctuating surface and the second component, having a larger bending rigidity and an intrinsic curvature, represents the particles. Although such an effective representation would probably be appropriate mostly for intermediate binding strengths (deformations), it is not obvious how to associate a Gaussian rigidity to these systems. Nevertheless, it provides an elegant and more general framework of the problem that can be easily generalized to particles interacting on fluid membranes as well as on interfaces.

Furthermore, there is typically a certain degree of attraction between nanoparticles, which introduces an extra degree of complexity in the nanoparticle-membrane

systems. In which case the nanoparticle-surface binding competes with the binding of nanoparticles between themselves. Our preliminary results indicate a rich variety of new phases which arise due to the interplay between the linear and isotropic aggregation. Moreover, different mechanisms of nanoparticle invagination by fluid membranes can be obtained, with multiple-file nanotubes, as well as budding of two- and three-dimensional nanoparticle crystals.

It would also be interesting to study the effect of electrostatic interactions in these systems. It has been shown that binding of charged nanoparticles can lead to membrane tubulation and subsequential membrane pearling [144], a process which is not yet understood. Moreover, charged nanoparticles, in the limit of large nanoparticle concentrations, have been found to induce membrane shrinkage and formation of homogeneously distributed tubes extruding perpendicularly from the membrane surface [245]. For this purpose, the role of the volume and surface-area constraints on the membrane, both highly dependent on the experimental conditions, should be explored.

Finally, we plan to study how the presence of surface defects, that are known to create long-range elastic perturbations in elastic membranes, may alter the nanoparticles aggregation patterns. We expect this study to suggest additional mechanisms for controlling functionalization of elastic surfaces.

References

[1] G. M. Whitesides and M. Boncheva, *Proc. Natl. Acad. Sci. U. S. A.*, 2002, **16**, 4769.

[2] B. Alberts, A. Johnson, J. Lewis, M. Raff, K. Roberts and P. Walter, *Molecular biology of the cell.*, 5th ed. (Garland Science, New York, 2008).

[3] F. H. C. Crick and J.D. Watson, *Nature*, 1956, **177**, 473.

[4] A. Klug and D. L. D. Caspar, *Advances in Virus Res.*, 1960, **7**, 225.

[5] E. Sackmann, *Can. J. Phys.*, 1990, **68** , 999.

[6] G. Subramanian, V. N. Manoharan, J. D. Thorne and D. J. Pine, *Advanced Materials*, 1999, **11**, 1261.

[7] G. A. DeVries, et al., *Science*, 2007, **315**, 358.

[8] M. Li, H. Schnablegger and S. Mann, *Nature*, 1999, **402**, 393.

[9] L. Hong, S. Jiang and S. Granick, *Langmuir*, 2006, **22**, 9495.

[10] H. Weller, *Phil. Trans. R. Soc. A*, 2003, **361**, 229.

[11] E. K. Hobbie et al., *Langmuir*, 2005, **21**, 10284.

[12] J. N. Israelachvili, D. J. Mitchell and B. W. Ninham, *J. Chem. Soc., Faraday Trans. 2*, 1976, **72**, 1525.

[13] S. U. Pickering, *J. Chem. Soc.*, 1907, **91**, 2001.

[14] C. Zeng, H. Bissig and A.D. Dinsmore, *Solid State Commun.*, 2006, **139**, 547 and references therein.

[15] A. Böker, J. Heb, T. Emrick and T. P. Russell, *Soft Matter*, 2007, **3**, 1231.

[16] Z. W. Niu, J. B. He, T. P. Russell and Q. A. Wang, *Angew. Chem.*, 2010, **49**, 10052.

[17] N. Bowden, A. Terfort, J. Carbeck and G. M. Whitesides, *Science*, 1997, **276**, 233.

[18] N. Bowden, I. S. Choi, B. A. Grzybowski and G. M. Whitesides, *J. Am. Chem. Soc.*, 1999, **121**, 5373.

[19] P. G. de Gennes, *Rev. Mod. Phys.*, 1985, **57**, 827.

[20] J. N. Israelachvili, *Intermolecular And Surface Forces*, (Academic Press, San Diego, 1992).

[21] D. H. Gracias, J. Tien, T. L. Breen, C. Hsu and G. M. Whitesides, *Science*, 2000, **289**, 1170.

[22] G. M. Whitesides, B. Grzybowski, *Science*, 2002, **295**, 2418.

[23] L. Botto , E. P. Lewandowski, M. Cavallaro and K. J. Stebe, *Soft Matter*, 2012, **8**, 9957.

[24] D. Boal, *Mechanics of the Cell*, (Cambridge University Press, 2001).

[25] S. Safran, *Statistical Thermodynamics Of Surfaces, Interfaces, And Membranes*, (Westview Press, 2003).

[26] A. Nel et al. *Nature Mater.*, 2009, **8**, 543.

[27] H. F. Krug and P. Wick, *Angew. Chem.*, 2011, **50**, 1260.

[28] S. Hiltl, M.-P. Schürings, A. Balaceanu, V. Mayorga, C. Liedel, A. Pich and A. Böker, *Soft Matter*, 2011, **7** 8231.

[29] T. A.-J. Wafa and K. Kostarelos, *Nanomedicine*, 2007, **2**, 85.

[30] P. J. Costanzo, E. Liang, T. E. Patten, S. D. Collins and R. L. Smith, *Lab Chip*, 2006, **5**, 606.

[31] R. J. Mart, K. P. Liem and S. J. Webb, *Pharm. Res.*, 2009, **26**, 1701.

[32] J. H. Fendler, *Acc. Chem. Res.*, 1980, **13**, 7.

[33] J. Oberdisse et al., *Langmuir*, 1996, **12**, 1212.

[34] D. E. Discher and A. Eisenberg, *Science*, 2002, **297**, 967.

[35] E. Barry and Z. Dogic, *Proc. Natl. Acad. Sci. U. S. A.*, 2010, **107**, 10348.

[36] L. D. Landau and E. M. Lifshitz, *Theory of Elasticity*, (Pergamon, New York, 1970).

[37] J. H. Fendler and P. Tundo, *Acc. Chem. Res.*, 1984, **17**, 3.

[38] P. C. Georges, P. A. Janmey, *J. Appl. Physiol.*, 2005, **98**, 1547.

[39] A. Elgsaeter, B. T. Stokke, A. Mikkelsen and D. Branton, *Science*, 1986, **234**, 1217.

[40] C. F. Schmidt et al., *Science*, 1993, **259**, 952.

[41] K. E. Mueggenburg, X. M. Lin, R. H. Goldsmith and H. M. Jaeger, *Nature Mater.*, 2007, **6**, 656.

[42] S. Stankovich et al., *Nature*, 2006, **442**, 282.

[43] J. C. Meyer et al., *Nature*, 2007, **446**, 60.

[44] M. S. Spector, E. Naranjo, S. Chiruvolu, J. A. Zasadzinski, *Phys. Rev. Lett.*, 1994, **73**, 2867.

[45] X. Wen et al., *Nature*, 1992, **355**, 426.

[46] J. Huang et al. *Science*, 2007, **317**, 650.

[47] R. J. Hamers, *Nature*, 2001, **412**, 489.

[48] K. Efimenko et al., *Nature Mater*, 2005, **4**, 293.

[49] N. Doshi, A. Zahr, S. Bhaskar, J. Lahann and S. Mitragotri, *Proc. Natl. Acad. Sci. U. S. A.*, 2009, **106**, 21495.

[50] J. H. Lim, K. S. Lee, J. C. Kim and B. H. Lee, *Opt. Lett.*, 2004, **29**, 331.

[51] F. Ilievski, A. D. Mazzeo, R. F. Shepherd, X. Chen and G. M. Whitesides, *Angew. Chem. Int. Ed.*, 2011, **50**, 1890.

[52] W. Helfrich, *Z. Naturforsch. C*, 1973, **28**, 693.

[53] F. L. H. Brown, *Annu. Rev. Phys. Chem.*, 2008,**59**, 685.

[54] M. Hu, J. J. Briguglio and M. Deserno, *Biophys. J.*, 2012, **102**, 1403.

[55] E. Kurtisovski, N. Taulier, R. Ober, M. Waks and W. Urbach, *Phys. Rev. Lett.*, 2007, **98**, 258103.

[56] H. Bermúdez, A. K. Brannan, D. A. Hammer, F. S. Bates and D. E. Discher, *Macromolecules*, 2002, **35**, 8203.

[57] H. Bermúdez , D. A. Hammer and D. E. Discher, *Langmuir*, 2004, **20**, 540.

[58] F. Jähnig, *Biophys. J.*, 1996 , **71**, 1348.

[59] T. A. Witten, *Rev. Mod. Phys.*, 2007, **79**, 643.

[60] K. Efimenko, M. Rackaitis, E. Manias, A. Vaziri, L. Mahadevan and J. Genzer, *Nature Mater.*, 2005, **4**, 293.

[61] M. Goulian, *Curr. Opin. Colloid Interface Sci.*, 1996, **3**, 358361.

[62] R. Phillips, T. Ursell, P. Wiggins and P. Sens, *Nature*, 2009, **459**, 379-85.

[63] T. Gil et al., *Biochim. Biophys. Acta.*, 1998, **1376**, 245.

[64] M. Goulian, R. Bruisma and P. Pincus, *Europhys. Lett.*, 1993, **22**, 145.

[65] M Goulian, R Bruinsma and P Pincus, Erratum, *Europhys. Lett.*, 1993, **23**, 155.

[66] P.G. Dommersnes and J.-B. Fournier, *Europhys. Lett.*, 1997, **39**, 681.

[67] D. R. Fattal and A. Ben-Shaul, *Biophys. J.*, 1993, **65**, 17951809.

[68] H. W. Huang, *Biophys. J.*, 1986, **50**, 1061.

[69] H. Aranda-Espinoza, A. Berman, N. Dan, P. Pincus and S. Safran, *Biophys J.*, 1996, **71**, 648.

[70] J. A. Killian, *Biochim. Biophys. Acta Rev. Biomembr.*, 1998, **1376**, 401.

[71] M. S. Turner and P. Sens, *Phys. Rev. Lett.*, 2004, **93** 118103.

[72] B. J. Reynwar and M. Deserno, *Soft Matter*, 2011, **7**, 8567.

[73] P. G. Dommersnes and J.-B. Fournier, *Eur. Phys. J. B*, 1999, **12**, 9.

[74] A. D. Dinsmore, D. T. Wong, P. Nelson and A. G. Yodh, *Phys. Rev. Lett.*, 1998, **80**, 409.

[75] I. Koltover, J. O. Rädler and C. R. Safinya, *Phys. Rev. Lett.*, 1999, **82**, 1991.

[76] T. Baumgart, S. T. Hess and W. W. Webb, *Nature*, 2003, **425**, 821.

[77] F. Jülicher and R. Lipowsky, *Phys. Rev. Lett.*, 1992, **70**, 2964.

[78] T. S. Ursell, W. S. Klug and R. Phillips, *Proc. Natl. Acad. Sci. U. S. A.*, 2009, **106**, 13301.

[79] J. E. Rothman, *Nature*, 1994, **372**, 55.

[80] K. Farsad and P. De Camilli, *Curr. Opin. Cell Biol.*, 2003, **15**, 372.

[81] R. N. Frese et al., *Biophys. J.*, 2008, **94**, 640.

[82] J. T. Groves, *Annu. Rev. Phys. Chem.*, 2007, **58**, 697.

[83] R. Parthasarathy and J. T. Groves, *Soft Matter*, 2007, **3**, 24.

[84] D. R. Nelson, *Nano Lett.*, 2002, **2**, 1125.

[85] G. Srinivas, D. E. Discher and M. L. Klein, *Nature Mater.*, 2004, **3**, 638.

[86] G. Srinivas, J. C. Shelley, S. O. Nielsen, D. E. Discher and M. L. Klein, *J. Phys. Chem. B*, 2004, **108**, 8153.

[87] S. M. Loverde, D. A. Pantano, D. A. Christian, A. Mahmud, M. L. Klein and D. E. Discher, *Curr. Opin. Solid State Mater. Sci.*, 2011, **15**, 277.

[88] L. Rekvig, B. Hafskjold and B. Smit, *Phys. Rev. Lett.*, 2004, **92**, 116101.

[89] F. L. Brown, *Q. Rev. Biophys.*, 2011, **44**, 391.

[90] M. Deserno, *Macromol. Rapid Commun.*, 2009, **30**, 752.

[91] M. Venturoli, M. M. Sperotto, M. Kranenburg and B. Smit, *Phys. Rep.*, 2006, **437**, 1.

[92] H. Noguchi, *J. Phys. Soc. Jpn.*, 2009, **78**, 041007.

[93] A. P. Lyubartsev and A. L. Rabinovich, *Soft Matter*, 2011, **7**, 25.

[94] O. Farago, *J. Chem. Phys.*, 2003, **119**, 596.

[95] Z.-J. Wang and D. Frenkel, *J. Chem. Phys.*, 2005, **122**, 234711.

[96] I. R. Cooke, K. Kremer and M. Deserno, *Phys. Rev. E*, 2005, **72**, 011506.

[97] G. Brannigan and F. L. H. Brown, *J. Chem. Phys.*, 2004, **120**, 1059.

[98] S. Izvekov and G. A. Voth, *J. Phys. Chem. B*, 2005, **109**, 2469.

[99] G. Brannigan, L. C.-L. Lin and F. L. H. Brown, *Eur. Biophys. J.*, 2006, **35**, 104.

[100] M. Müller, K. Katsov and M. Schick, *Phys. Rep.*, 2006, **434**, 113.

[101] Y. Kantor, M. Kardar and D.R. Nelson, *Phys. Rev. Lett.*, 1986, **57**, 791.

[102] J.-S. Ho and A. Baumgärtner, *Europhys. Lett.*, 1990, **12**, 295.

[103] A. Baumgärtner and J.-S. Ho, *Phys. Rev. A*, 1990, **41**, 5747.

[104] G. Gompper and D. M. Kroll, *J. Phys.: Condens. Matter*, 1997, **9**, 8795.

[105] J. M. Drouffe, A. C. Maggs, and S. Leibler, *Science*, 1991, **254**, 1353.

[106] M. G. Del Pópolo and P. Ballone, *J. Chem. Phys.*, 2008, **128**, 024705.

[107] H. Yuan, C. Huang, J. Li, G. Lykotrafitis and S. Zhang, *Phys. Rev. E*, 2010, **82**, 011905.

[108] T. Kohyama, *Physica A*, 2009, **388**, 3334.

[109] H. Noguchi and G. Gompper, *Phys. Rev. E*, 2006, **73**, 021903.

[110] G. A. Vliegenthart and G. Gompper, *Nat Mater.*, 2006, **5**, 216-221.

[111] D.E. Discher, D.H. Boal and S.K. Boey, *Biophys. J.*, 1998, **75**, 1584.

[112] J. Li, M. Dao, C.T. Lim and S. Suresh, *Biophys. J.*, 2005, **88**, 3707.

[113] H. Noguchi and G. Gompper, *Proc. Natl. Acad. Sci. U. S. A.*, 2005, **102**, 14159.

[114] J. Li, G. Lykotrafitis, M. Dao and S. Suresh, *Proc. Natl. Acad. Sci. U. S. A.*, 2007, **104**, 4937.

[115] H. Li and G. Lykotrafitis, *Biophys J.*, 2012, **102**, 75.

[116] H. Noguchi and G. Gompper, *Phys. Rev. Lett*, 2004, **93**, 258102.

[117] D. Frenkel and B. Smit, *Understanding Molecular Simulation: From Algorithms to Applications*, 2nd ed. (Academic Press, San Diego, 2002).

[118] M. E. Tuckerman, *Statistical Mechanics: Theory and Molecular Simulation*, 1st ed. (Oxford University Press, USA, 2010).

[119] G. M. Torrie, J. P. Valleau, *J. Comp. Phys.*, 1997, **23**,187.

[120] J. Kästner, *WIREs Comput Mol Sci*, 2011, **1**, 932.

[121] A. Šarić and A. Cacciuto, *Phys. Rev. Lett.*, 2012, **108**, 118101.

[122] A. Šarić and A. Cacciuto, *Phys. Rev. Lett.*, 2012, **109**, 188101.

[123] A. Šarić and A. Cacciuto, *Soft Matter*, 2011, **7**, 8324.

[124] A. Šarić, J. C. Pàmies and A. Cacciuto, *Phys. Rev. Lett.*, 2010, **104**, 226101.

[125] J. A. Napoli, A. Šarić and A. Cacciuto, in preparation.

[126] A. Šarić and A. Cacciuto, *Soft Matter*, 2011, **7**, 1784.

[127] R.R. Netz, *J. Phys. I France*, 1997, **7**, 833.

[128] I. Koltover, T. Salditt and C. R. Safinya, *Biophys J.*, 1999, **77**, 915.

[129] T. Yue and X. Zhang, *ACS Nano*, 2012, **6**, 3196.

[130] C. Wilhelma et al., *Biomaterials*, 2003, **24**, 1001.

[131] M. Kranenburg, M. Venturoli and B. Smit, *Phys. Rev. E*, 2003, **67**, 060901.

[132] L. Ramos, T. C. Lubensky, N. Dan, P. Nelson and D. A. Weitz, *Science*, 1999, **286**, 2325.

[133] P. Sens, L. Johannes and P. Bassereau, *Curr. Opin. Cell. Biol.*, 2008, **4**, 476.

[134] J. Mercer, M. Schelhaas and A. Helenius, *Annu. Rev. Biochem.*, 2010, **79**, 803.

[135] B. J. Chen and R. A. Lamb, *Virology*, 2008, **372**, 221.

[136] S. D. Conner and S. L. Schmid, *Nature*, 2003, **422**, 37.

[137] S. Mayor and R. Pagano, *Nat. Rev. Mol. Cell Biol.*, 2007, **8**, 603.

[138] J. Zimmerberg and M. M. Kozlov, *Nature Rev. Mol. Cell Biol.*, 2006, **7**, 9.

[139] W. A. Prinz and J. E. Hinshaw, *Crit. Rev. Biochem. Mol. Biol.*, 2009, **44**, 278.

[140] B. J. Reynwar, G. Illya, V. A. Harmandaris, M. M. Müller, K. Kremer and M. Deserno, *Nature*, 2007, **447**, 461.

[141] W. Römer et al., *Nature*, 2007, **450**,670.

[142] J. H. Hurley, E. Boura, L.-A. Carlson and B. Różycki, *Cell*, 2010, **143**, 875.

[143] H. Garoff, R. Hewson, D.-J. E. Opstelten, *Microbiol. Mol. Biol. Rev.*, 1998, bf 62, 1171.

[144] Y. Yu and S. Granick, *J. Am. Chem. Soc.*, 2009, **131**, 14158.

[145] H. Ewers et al., *Nat. Cell Biol.*, 2010, **12**, 11.

[146] I. Gözen, C. Billerit, P. Dommersnes, A. Jesorka and Owe Orwar, *Soft Matter*, 2011, **7**, 9706.

[147] M. Deserno, *Phys. Rev. E*, 2004, **69**, 031903.

[148] M. Deserno, *J. Phys.: Condens. Matter*, 2004, **16**, S2061.

[149] K. A. Smith, D. Jasnow and A. C. Balazs, *J. Chem. Phys.*, 2007, **127**, 084703.

[150] M. Fošnarič, A. Iglič, D. M. Kroll and S. May, *J. Chem. Phys.*, 2009, **131**, 105103.

[151] S. Mkrtchyan, C. Ing, and J. Z. Y. Chen, *Phys. Rev. E*, 2010, **81**, 011904 .

[152] R. Vácha, F. J. Martinez-Veracoechea and D. Frenkel, *Nano Lett.*, 2011, **11**, 5391.

[153] R. Lipowsky and H.G. Döbereiner, *Europhys. Lett.*, 1998, **43**, 219.

[154] M. Deserno and T. Bickel, *Europhys. Lett.*, 2003, **62**, 767.

[155] M. Deserno, *Phys. Rev. E*, 2004, **69**, 031903.

[156] S. Tzlil, M. Deserno, W. M. Gelbart and A. Ben-Shaul, *Biophys J.*, 2004, **86**, 2037.

[157] H. Gao, W. Shi and L. B. Freund, *Proc. Natl. Acad. Sci. U. S. A.*, 2005, **102**, 9469.

[158] S. Zhang, J. Li, G. Lykotrafitis, G. Bao and S. Suresh, *Adv. Mater.*, 2009, **21**, 419.

[159] H. Yuan, J. Li, G. Bao and S. Zhang, *Phys. Rev. Lett.*, 2010, **105**, 138101.

[160] A. Chaudhuri, G. Battaglia and R. Golestanian, *Phys. Biol.*, 2011, **8** 046002.

[161] K. A. Smith, D. Jasnow and A. C. Balazs, *J. Chem. Phys.*, 2007, **127**, 084703.

[162] Y. Li and N. Gu, *J. Phys. Chem. B*, 2010, **114**, 27492754.

[163] T. Yue and X. Zhang, *Soft Matter*, 2011, **7**, 9104.

[164] T. Ruiz-Herrero, E. Velasco and M. F. Hagan, *J. Phys. Chem. B*, 2012, **116**, 9595.

[165] W. Jiang, B. Y. Kim, J. T. Rutka, W. C. Chan, *Nat. Nanotechnol*, 2008, **3**, 145.

[166] Y. Roiter, M. Ornatska, A. R. Rammohan, J. Balakrishnan, D. R. Heine, S. Minko, *Nano Lett.*, 2008, **8**, 941.

[167] S. Zhang, A. Nelson, P. A. Beales, *Langmuir*, 2012, **28**, 12831.

[168] K. Yang and Y. Ma, *Aust. J. Chem.*, 2011, **64**, 894.

[169] D. S. Dean, T. C. Hammant, R. R. Horgan, A. Naji and R. Podgornik *J. Chem. Phys.*, 2012, **137**, 144904.

[170] X. Yi, X. Shi and H. Gao, *Phys. Rev. Lett.*, 2011, **107**, 098101.

[171] R.D. Vale and H. Hotani, *J. Cell Biol.*, 1988, **107**, 2233.

[172] M. Waterman-Storer and E.D. Salmon, *Curr. Biol.*, 1998, **8**, 798.

[173] E. Evans et al., *Science*, 1996, **273**, 933.

[174] T. Roopa and G.V. Shivashankar, *Appl. Phys. Lett.*, 2003, **82**, 1631.

[175] D. Raucher and M.P. Sheetz, *Biophys. J.*, 1999, **77**, 1992.

[176] D. Cuvelier, N. Chiaruttini, P. Bassereau and P. Nassoy, *Europhys. Lett.*, 2005, **71**, 1015.

[177] R.E. Waugh, *Biophys. J.*, 1982, **38**, 29.

[178] I. Derenyi, F. Jülicher and J. Prost, *Phys. Rev. Lett.*, 2002, **88**, 238101.

[179] G. Koster, A. Cacciuto, I. Derényi, D. Frenkel and M. Dogterom, *Phys. Rev. Lett.*, 2005, **94**, 068101.

[180] W. Römer et al., *Nature*, 2007, **450**, 670.

[181] J. Zimmerberg and M.M. Kozlov, *Nat. Rev. Mol. Cell Biol.*, 2006, **7**, 9.

[182] W.A. Prinz and J.E. Hinshaw, *Crit. Rev. Biochem. Mol. Biol.*, 2009, **44**, 278.

[183] R. Matthews and C. N. Likos, *Phys. Rev. Lett.*, 2012, **109**, 178302.

[184] A. H. Bahrami, R. Lipowsky and T. R. Weikl, *Phys. Rev. Lett.*, 2012, **109**, 188102.

[185] I. Derenyi, F. Jülicher and J. Prost, *Phys. Rev. Lett.*, 2002, **88**, 238101.

[186] D. E. Discher, P. Janmey and Y. Wang, *Science*, 2005, **310**, 1139.

[187] A. Engler at al., *Biophys. J.*, 2004, **86**, 617.

[188] C. M. Stafford, E. E. Simony et al., *Nature Mater.*, 2004, **3**, 545.

[189] A. Schweikart, A. Fortini, A. Wittemann, M. Schmidt and A. Fery, *Soft Matter*, 2010, **6**, 5860, and references therein.

[190] E. Cerda, S. Chaieb, F. Melo and L. Mahadevan, *Nature*, 1999, **401**,46.

[191] E. Cerda, K. Ravi-Chandar and L. Mahadevan, *Nature*, 2002, **419**, 579.

[192] E. Cerda and L. Mahadevan, *Phys. Rev. Lett.*, 2003, **90**, 074302.

[193] M. Endo, H. Muramatsu, T. Hayashi, Y. A. Kim, M. Terrones and N. S. Dresselhaus, *Nature*, 2005, bft 433, 476.

[194] L. A. Girifalco, M. Hodak and R. S. Lee, *Phys. Rev. B*, 2000, **62**, 13104.

[195] L. J. Hall, V. R. Coluci, D. S. Galvao, M. E. Kozlov, M. Zhang, S. O. Dantas and Baughman, *Science*, 2008, **320**, 504.

[196] S. J. Plimpton, *J. Comp. Phys.*, 1995, **117**, 1.

[197] T. Nakano and Y. Okamoto, *Chem. Rev.*, 2001, **101**, 4013.

[198] M. Zheng et al., *Nature Mater.*, 2003, **2**, 338.

[199] D. W. Ehrhardt and S. L. Shaw, *Annu. Rev. Plant Biol.*, 2006, **57** 859.

[200] E. M. Wilson-Kubalek et. al., *Proc. Natl. Acad. Sci. U. S. A.*, 1998, **95** 8040.

[201] F. Balavoine et. al. *Angew. Chem. Int. Ed.*, 1999, **38**, 1912.

[202] A. C. Neville, *Biology of Fibrous Composites*, (Cambridge University Press, New York, 1993).

[203] I. Kusner and S. Srebnik, *Chem. Phys. Lett.*, 2006, **430**, 84.

[204] D. W. Adams and J. Errington, *Nature Rev. Microbiol.*. 2009, **7**, 642.

[205] D. Bray, *Cell movements: from molecules to motility*, 2nd ed., (Garland, New York, 2001).

[206] L. Mahadevan, A. Vaziri and M. Das, *EuroPhys. Lett.*, 2007, **77**, 40003.

[207] P. J. de Pablo et. al., *Phys. Rev. Lett.*, 2003, **91**, 098101.

[208] I. Gurevitch and S. Srebnik, *Chem. Phys. Lett.*, 2007, **444**, 96.

[209] J. C. Pàmies and A. Cacciuto, *Phys. Rev. Lett.*, 2011, **106**, 226101.

[210] X. Peng, J. Chen, J. A. Misewich and S. S. Wong, *Chem. Soc. Rev.*, 2009, **38**, 1076.

[211] M. Ding, D. C. Sorescu, G. P. Kotchey and A. Star, *J. Am. Chem. Soc.*, 2012, **134**, 3472.

[212] R.Y. Zhang, M. Hummelgård and H. Olin, *Mater. Sci. Eng. B*, 2009, **158**, 48.

[213] G. A. Rance , D. H. Marsh , S. J. Bourne , T. J. Reade and A. N. Khlobystov, *ACS Nano*, 2010, **4**, 4920.

[214] H. Yang, M. Li, L. Fu, A. Tang and S. Mann, *Sci. Rep.*, 2013, **3**, 1336.

[215] X. Li, Y. Qin, S. T. Picraux and Z.-X. Guo, *J. Mater. Chem.*, 2011, **21**, 7527.

[216] A. La Torre et al., *Nanoscale*, 2010, **2**, 1006.

[217] Q. Zhao, Z. H. Gan and Q. K. Zhuang, *Electroanalysis*, 2002, **14**, 1609.

[218] L.C. Jiang and W.D. Zhang, *Biosens. Bioelectron.*, 2010, **25**, 1402.

[219] Y. Yu et al., *Micro Nano Lett.*, 2009, **4**, 27.

[220] V. Lordi, N. Yao and J. Wei, *Chem. Mater.*, 2001, **13**, 733.

[221] X. Peng, S. Wong, *Chem. Mater.*, 2009, **21**, 682.

[222] C. Wang et al., *Nano Lett.*, 2004, **4**, 345.

[223] K. Koziol et al., *Science*, 2007, **318**, 1892.

[224] J. N. Zhao et al., *Small*, 2010, **6**, 2612.

[225] Z. Shi et al., *Nanoscale*, 2012, **4**, 4515.

[226] P. R. Somani, S. P. Somani and M. Umeno, *Appl. Phys. Lett.*, 2008, **93**, 033315.

[227] D. H. Marsh, G. A. Rance, R. J. Whitby, F. Guistiniano and A. N. Khlobystov, *J. Mater. Chem.*, 2008, **18**, 2249.

[228] J. Zang, A. Treibergs, Y. Han, and F. Liu, *Phys. Rev. Lett.*, 2004, **92**, 105501.

[229] J. A. Elliott, J. K. W. Sandler, A. H. Windle, R. J. Young and M. S. P. Shaffer, *Phys. Rev. Lett.*, 2004, **92**, 095501.

[230] T. Tang, A. Jagota, C.-Y. Hui and N. J. Glassmaker, *J. Appl. Phys.*, 2005, **97**, 074310.

[231] W. Lu and T.-W. Chou, *Phys. Rev. B*, 2011, **83**, 134113.

[232] C. J. Park, Y. H. Kim and K. J. Chang, *Phys. Rev. B*, 1999, **60**, 10656.

[233] A. P. M. Barboza et al., *Phys. Rev. Lett.*, 2008, 100, 256804.

[234] C. E. Giusse, Y. Tison, and S. R. Silva, *Nano Lett.*, 2008, **8**, 3350.

[235] J. Lidmar, L. Mirny and D. R. Nelson, *Phys. Rev. E*, 2003, **68**, 051910.

[236] H. M. S. Coxeter, *Introduction to Geometry* , (Wiley, New York, 1969).

[237] S. Nose, *J. Chem. Phys.*, 1984, **81**, 511.

[238] W. G. Hoover, *Phys. Rev. A*, 1985, **31**, 1695.

[239] J. Lidmar, L. Mirny and D. R. Nelson, *Phys. Rev. E*, 2003, **68**, 051910.

[240] V. Vitelli and D. R. Nelson, *Phys. Rev E*, 2006, **74**, 021711.

[241] A. M. Turner, V. Vitelli and D. R. Nelson, *Rev. Mod. Phys.*, 2010, **82**, 1301.

[242] A. D. Dinsmore et al., *Science*, 2002, **298**, 1006.

[243] G. Vernizzi, R. Sknepnek and M. Olvera de la Cruz, *Proc. Natl. Acad. Sci. U. S. A.*, 2011, **108**, 4292.

[244] R. Sknepnek, G. Vernizzi and M. Olvera de la Cruz, *Soft Matter*, 2012, **8**, 636-644.

[245] M. Šimunović, S. Aimon and P. Bassereau, unpublished results.